Plasma physical and material physical aspects of the application of atmospheric gases as a propellant for Ion-Thruster of the RIT-Type

Inaugural dissertation to graduate to
the doctor's degree in natural sciences
at the Justus-Liebig-University of Giessen
(FB-07 Physics)

Handed in by

Benjamin Lotz

from Giessen

May 2013

Dekan: Prof. Dr. P. Klar
1. Commentator: Prof. Dr. B.K. Meyer
2. Commentator: Prof. Dr. M. Thoma
Date of the defense of the thesis: 26.06.2013

Contents

List of figures

List of tables

Abbreviations

A	Wall surface
AC	Alternating Current
Accel	Acceleration
A_{ex}	Extraction area
A_I	Ionizer wall area
AUX	Auxiliary
BCC	Beam-Current-Controller
CAD	Computer-Assisted-Design
CC	Compression Correction factor
CEX	Charge Exchange
DC	Direct Current
Decel	Deceleration
DSMC	Direct Simulation Monte Carlo
EBB	Elegant Bread Board
E_{ind}	Induced electrical field
EP	Electric Propulsion
F	Thrust
FCU	Flow-Control-Unit
f_i	Ionization integral factor
g	Earth gravity acceleration
g_0	Gas flow of extracted ions
h	Planck's constant
Hg	Mercury
HPT	High-Performance-Test
I	Total current
I_{acc}	Drain Current on the Accel Grid
I_b	Beam Current ($I_i - I_{acc}$)
I_{Beam}	Beam Current ($I_i - I_{acc}$)
IC	Ionization-Chamber
I_{co}	Amplitude of the coil current

I_i	Extracted Ion current
I_{sp}, ISP	Specific impulse
j_A	Ambipolar current density
j_i	Ion beamt density
k	Boltzmann-constant
L	Inductance
l_c	Coil length
L_G	Grid conductance for gases
l_{opt}	Optimal length
$\dot{m}$	Mass-flow
m_{ion} , m_i	Mass (Ion)
m_e	Mass (electron)
ME	Mass efficency
MFC	Mass-Flow-Controller
MFM	Mass-Flow-Meter
n_0	Neutral particle density
N_c	Number of coil windings
n_e	Electron density
NHV	Negative-High-Voltage
N_i	Number of Ions
n_i	Ion density
n_{tot}	Total particle density
NTR	Neutralizer
P	Power
P_A	Ambipolar power losses
PHV	Postive-High-Voltage
P_I	Ionization power losses
p_I	Discharge pressure
P_{rf}	RF-Power provided by the RFG
P_{rfg}	RF-Power provided by the RFG
P-RFG	RF-Power provided by the RFG
PSCU	Power-Supply-Control-Unit

P-Total	Total power (RF-Power + RFG-Aux-Power + Beam-Power)
Q	Quality factor of coils
$q(CEX)$	Charge exchange cross section
q_i	Ionization cross section
q_{ion}	Ion charge
r	Grid hole radius
R	Radius
r_1	Screen-grid diameter
RAM-EP	The use of gathered atmospheric gases as a propellant for EP
rf	Radio Frequency
RFG	Radio Frequency Generator
RFG-Aux	Auxiliary power supply of the RFG
RIT	Radio-Frequency-Ion-Thruster
RITA	Radio Frequency Ion Thruster Assembly
S/C	Spacecraft
SC	Spacecraft
$SCCM$	Standard cubic centimeter
T	Temperature
T_0	Gas temperature in the ionizer
T_e	Electron temperature
THR	Thruster
TPS	Test-Power-Supply
TRB	Test-Review-Board
TRR	Test-Readiness-Review
U_-	Negative high voltage
U_+	Positive high voltage
U_a	Negative high voltage (accel grid)
U_{ex}	Extraction voltage
U_s	Positive high voltage (screen grid)
$\dot{V}$	Gas flow rate
$\dot{V}_0$	Neutral gas losses
V_I	Dicharge vessel volume

v_i	Ion velocity
$\dot{V}_i$	Gas consumption of the ions
V_P	Plasma-potential
w_0	Asymptotic fit parameter (eV/ion)
W_{diss}	Dissoziation-energy
W_e	Electron energy
w_i	Ion production costs
β	Percentage of the drain current (I_{acc}/I_i)
γ_c	Correction factor for short coils
ε_0	Electric field constant
μ_0	Magnetic susceptibility
η_{div}	Divergence efficiency factor
η_e	Electrical efficiency
η_{hom}	Homogeniety efficiency factor of the ion charge distribution
η_m	Mass efficency
ν	Frequency
ω	Circular frequency

1. Motivation

The low earth orbit (LEO) is a very interesting orbit for a huge amount of earth observation missions and also for the commercial sector. The low orbit altitude enables high precision measurements of the earth, even if the sensors are not very complex and their resolution is comparably low, also the launcher costs are quite cheap for this orbit. The major disadvantage of these orbits is the atmospheric drag, because the density of the surrounding atmosphere is still relatively high ($n_{tot}\ [m^{-3}] = 5.120 \cdot 10^{15}$, $\rho\ [kg/m^3] = 1.802 \cdot 10^{-10}$ and $T\ [K] = 742{,}4$ even for low sun activities, calculated with NRLMSISE-00 atmospheric model (1)). The resulting drag decelerates the spacecraft. The cross-section of the spacecraft has to be optimized to minimize this effect. In addition it is necessary to compensate this drag effect to maintain the mission altitude. This drag compensation can be realized whether with chemical and electrical propulsion. Both propulsion technologies need a big amount of propellant which has to be stored in the spacecraft to achieve an acceptable lifetime. In contrast the available spaces and also the maximum satellite masses are limited. To improve this situation the surrounding residual gas could be used to save propellant mass and increase mission lifetime. The atmospheric gases could be collected, compressed and used as propellant for the thruster. Apart from the gas gathering and the compression problem the usability of these unconventional propellants has to be demonstrated and verified for Electric-Propulsion-Systems. Though different EP-concepts are available on the market, the RIT-type is one of the most promising candidates for this kind of missions. The electrode-less discharge is nearly immune to chemically reactive gases like Oxygen, also the achievable thrust velocities and the throttling capabilities are very high. The feasibility of the thruster operation with atmospheric propellants, the measurement of the correlated thruster performance, a lifetime prediction and the development of a numerical thruster model are part of this dissertation.

This thesis starts with a theoretical chapter which introduces the fundamental equations and processes which are necessary to describe and to understand an rf-ion-thruster. The theoretical basis of the numerical model is also explained.

The following chapter 3 describes the performed experiments, consisting of two parts. The first part explains the used test setup, test hardware and the configurations. The second part describes the workflow and test sequences performed for this thesis.

The measured results are summarized and listed in chapter 4. At the beginning there are the flow calibration and the cold-flow tests. Afterwards the performance mappings, performance checks, endurance tests and grid measurements of Xenon, Nitrogen, Oxygen and their mixtures N_2+O_2 and N_2+O_2+Xe are described and their results are presented sequentially. The high performance test with N_2+O_2 finishes this chapter.

The results are post-processed, interpolated and discussed in the following chapter 5 to generate the required model parameters and to verify and explain the results.

The conclusion in chapter 6 summarizes the gathered details of the thruster lifetime, the demonstrated parameter fields and the dissociation problem.

The outlook proposes the future investigations which should be done to clarify the amount and impact of the dissociation and to improve the lifetime model of the grid-system with further lifetime tests.

2. Theory

This chapter summarizes the fundamental processes of a radio frequency ion thruster and the required diagnostics. The RIT-technology is based on an electrode-less discharge. An alternating electromagnetic field accelerates electrons inside the discharge chamber on circular paths. Once they have gathered enough energy the electrons can react in different ways with their environment. Table 8-1 provides the most important constants which are used in the equations of the following chapters.

2.1. Modeling inputs

To establish a mathematical model of RIT-engines running with atmospheric gases, four fields of former and recent investigations might be used (see Figure 2-1).

1st **Discharge theory:** The extractable ion beam current I_i depends on the gas pressure p_l or the neutral gas density n_0 in the ionizer, on the electron temperature T_e and the electron or plasma density n_e, as well as on the propellant species, e.g. on the ionization cross section q_i (see Figure 2-2). It will be discussed in detail as follows.

2nd **Discharge performance:** The dependency of the extracted ion current I_i on the rf-power P_{rf} and the gas flow rate $\dot{V}$ is to be measured in the frames of this thesis directly with a 10 cm rf-ion thruster for Xenon and atmospheric gasses O_2 and N_2.

Figure 2-4 shows the curves I_i (P_{rf},$\dot{V}$) for O_2 and N_2 (2) which could be regarded as a first approximation of the mathematical model.

3rd: **Extraction performance and theory:** Whether the beam current I_i offered by the plasma could really be extracted by the grid system, depends not only on the plasma data, but also on the extraction voltage U_{ex}, the grid geometry, and the propellant species.

4th **Discharge diagnostics:** By means of movable triple Langmuir probes, the plasma data T_e and n_e are to be measured as functions of the incoupled rf-power P_{rf} and the discharge pressure p_l. The ion beam yield I_i of the plasma was calculated by $n_e\sqrt{T_e}$ (see 2.2.2). Figure 2-3 shows the RIT-10 Mercury data (3). The shapes of the diagnostic curves for N_2 and O_2 are qualitatively the same. This activity is beyond the schedule of this thesis.

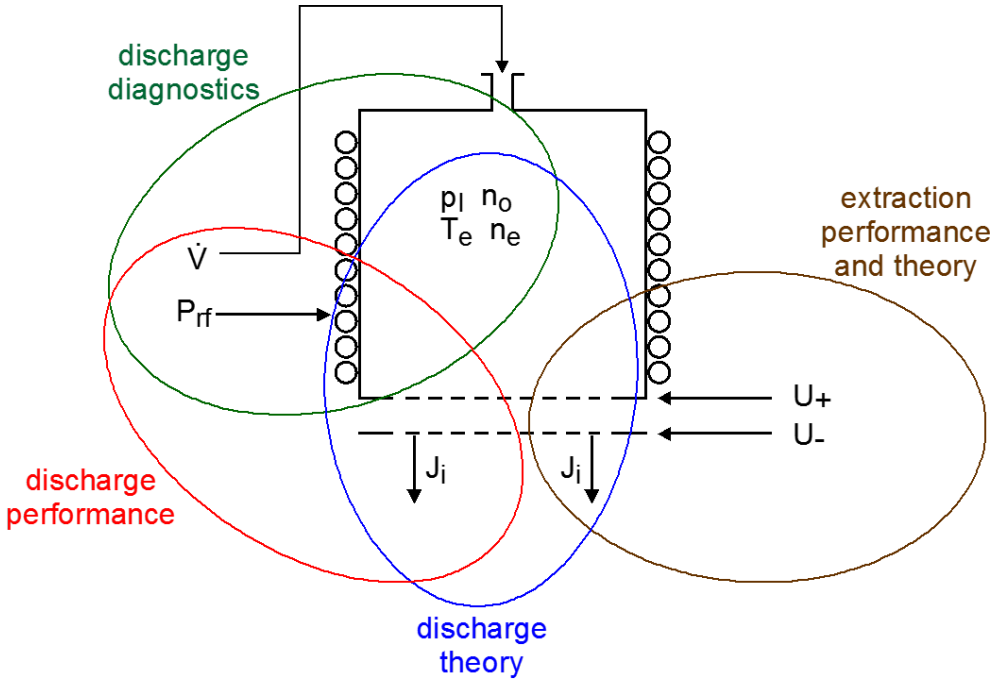

Figure 2-1: Four theoretical or experimental fields of investigation applied to establish a RIT-10 thruster performance model for operation with atmospheric gases (4)

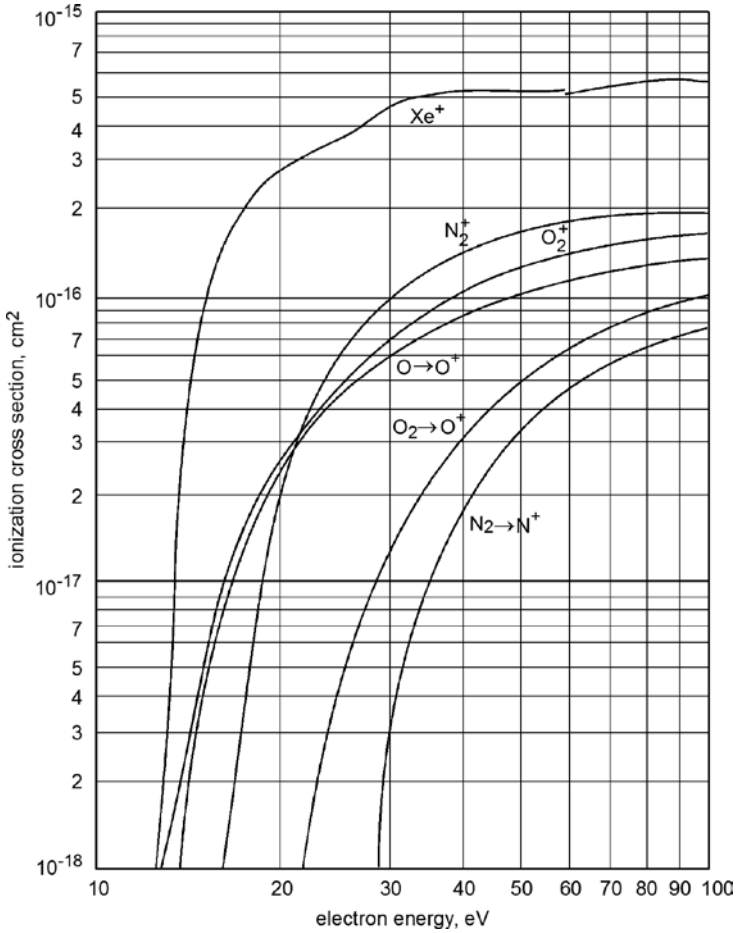

Figure 2-2: Ionization cross sections for Nitrogen and Oxygen as function of the electron energy (Xe-curve for comparison, presented data is based on NIST data) (5).

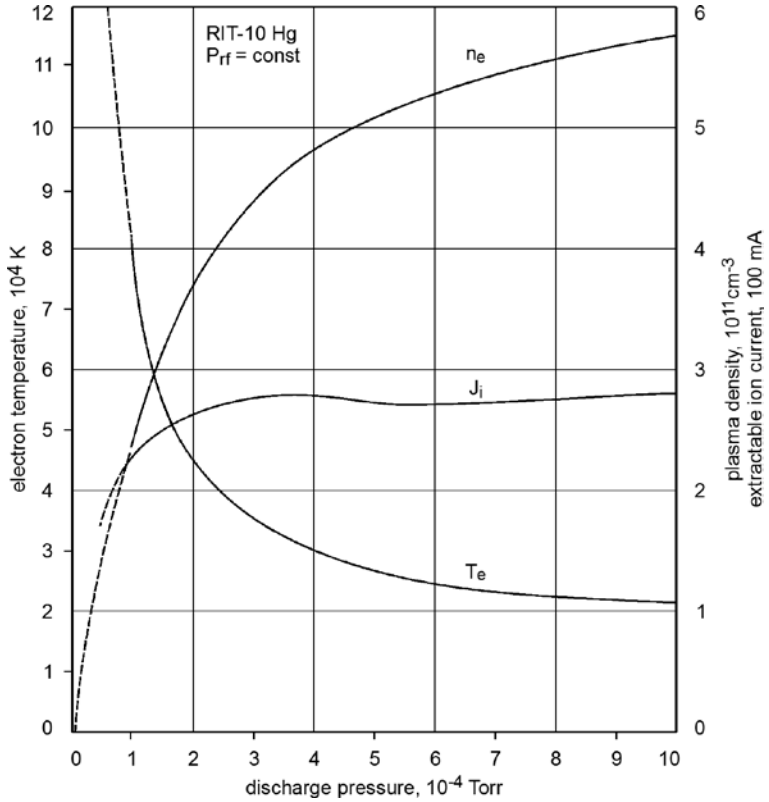

Figure 2-3: Plasma data as function of the discharge pressure for RIT-10 operated with Mercury at constant rf-power. Note that, although not shown in this curve, the plasma density n_e increases linearly with P_{rf} whereas the electron temperature T_e keeps nearly unchanged (3).

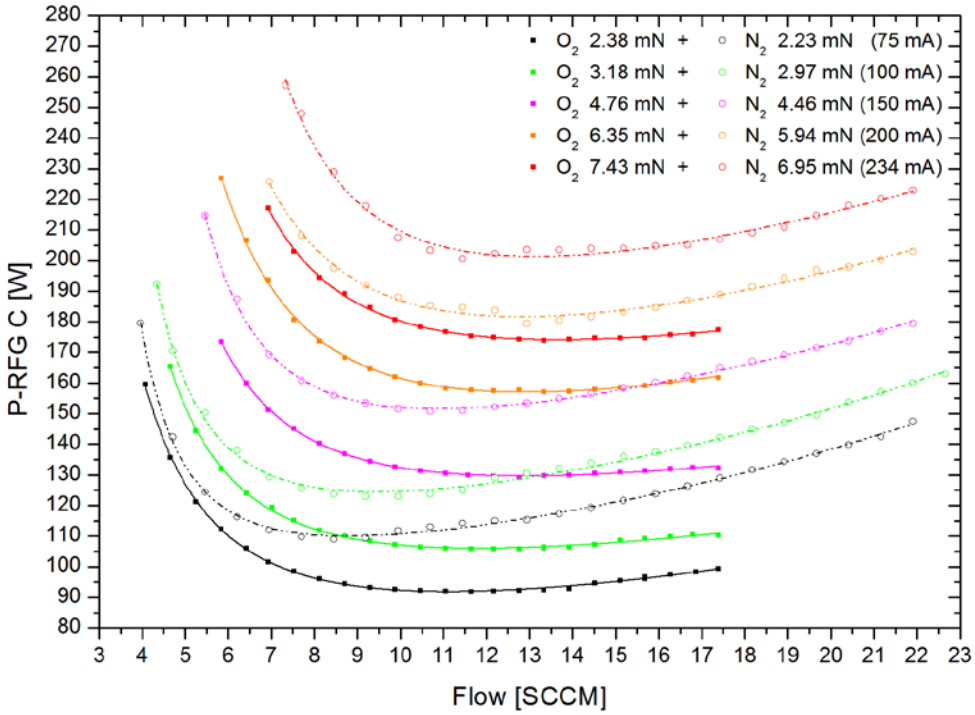

Figure 2-4: N_2 and O_2 comparison overview for P_{rfg} to mass flow

2.2. Basic mode of working

This chapter describes the major topics of the working principle of an rf-ion thruster. The chapter is grouped in four subchapters, the RF-ionization, the plasma balance and yield, the discharge characteristics and finally the ion extraction. The plasma generation and the ion extraction are compared to some other thruster principles like Hall Effect thrusters not directly coupled. That means that the plasma density can be separately varied while the extraction voltage stays constant and vice versa. However there would be voltage limitations for different plasma yields, given by the perveance limits. The first three chapters mostly take care about the plasma generation, whereas the last chapter concentrates on the extraction process.

2.2.1. RF-Ionization

The propellant (Xe, N_2, O_2, etc.) of an rf-ion thruster of the RIT-type is ionized by an electrode-less radio-frequency gas discharge. For this purpose, the induction coil of an rf-generator (RFG) surrounds the ionizer vessel made of a dielectric material. The coil generates an approximately axial rf-magnetic field which induces an electrical eddy field E_{ind} of the same RFG-frequency. Discharge electrons, have been generated in previous ionization collisions, are accelerated in this field. They gather energy until they are able to perform ionizing processes themselves.

Besides the ignition case, the self-sustaining discharge does not need a discharge cathode for a permanent electron supply. The induced annular electric field strength (6) (7) (8)is given by

$$E_{ind} = \frac{\mu_0 N_c}{2 l_c} \gamma_c r \omega \cdot I_{co} \cos \omega t \qquad 2\text{-}1$$

Herewith μ_o means the magnetic field constant, N_c the number of coil windings, l_c the coil length, γ_c a correction factor for short coils, r the distance from the axis, ω the angular frequency and I_{co} the amplitude of the coil current.
As E_{ind} is normally not high enough that an electron at rest can gather the necessary ionization energy during half of an rf-period (after which the direction of E_{ind} turns), an energy accumulation process must take place. Acceleration phases and elastic collisions with neutral gas particles take place alternatively resulting in a back and forth movement of the electrons. As this process follows the statistics, the electrons in an rf-discharge assume a Maxwell-Boltzmann distribution characterized by an electron temperature T_e. To enhance this energy accumulation process, the discharge pressure p_I should be adapted to the rf angular frequency ω. Both depend not only on the propellant species (mean free path) but also on the ionizer radius R (scaling laws see (9)):

$$p_I \sim \omega \sim \frac{1}{R} \qquad 2\text{-}2$$

The collision statistics with a Maxwellian distribution dn/n of the ionizing electrons, integrated over all electron energies W_e, yields the number of ionization collisions N_I per volume V and time t (10):

$$\frac{\partial^2 N_I}{\partial V \partial t} = \sqrt{\frac{8}{2\pi m_e}} \cdot n_0 n_e \cdot (kT_e)^{-3/2} \cdot \int_0^\infty q_i(W_e)\, W_e \cdot e^{-W_e/kT_e} dW_e \qquad 2\text{-}3$$

Figure 2-5 shows (for Xenon) the ionization integral factor $f_I = \frac{dn}{n} \cdot q_i \cdot W_e$ together with the Maxwellian-distribution dn/n of the electrons and the ionization cross section q_i. This integral $\int f_I dW_e$ (together with the densities of the neutrals n_o and electrons n_e) is proportional to the ionization rate $\partial^2 N_I / \partial V \partial t$.

Figure 2-6 compares f_I of O_2 and N_2 with Xe. Note that as a consequence of the lower q_i data, the ionization integral factors of O_2 and N_2 are by the factor of 10 smaller (see Figure 2-2).

Figure 2-7 and Figure 2-8 show in which way the ionization rate – and thus the beam current I_i– of atmospheric gases may be increased by a rise of the electron temperature T_e.

As mentioned already (see Figure 2-3), T_e depends strongly on the discharge pressure p_I but not on the rf-power P_{rf}. Figure 2-9 shows the decrease of $T_e(p_I)$ and the increase of the plasma density $n_e(q_i)$ for a given RIT-10 beam current $I_i = 250\ mA$. Note, that kT_e should be near the 10 eV level (see Figure 2-10) to enable a sufficiently high ionization rate within the entire discharge vessel.

It should be emphasized that in all previous considerations a mean electron temperature is used. In fact, T_e increases in an rf-engine strongly from the axis towards the walls which results in a maximum ionization rate in the periphery of the rf-ionizer (see Figure 2-11). This fact is caused directly by the induction law $E_{ind} \sim r$ with $r \leq R$ as the distance from the axis. (The difference from the linearity $E_{ind}(r)$ is mainly caused by the skin effect.)

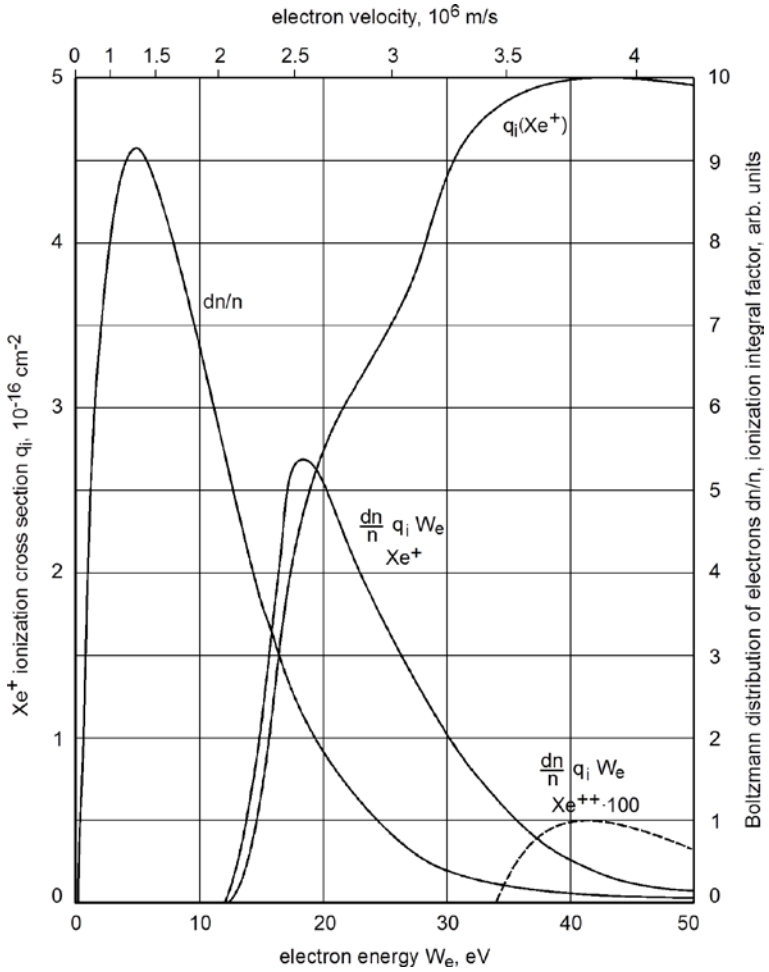

Figure 2-5: Maxwell-Boltzmann distribution dn/n of electrons with a maximum at 5 eV, ionization cross section q_i of Xe^+ and ionization integral factor $f_I = dn/n \cdot q_i \cdot W_e$ vs. the electron energy W_e note that 18 eV-electrons ionize the best; the dashed f_I-curve of the Xe^{++} shows the small percentage of double charged ions in an rf-thruster (11)

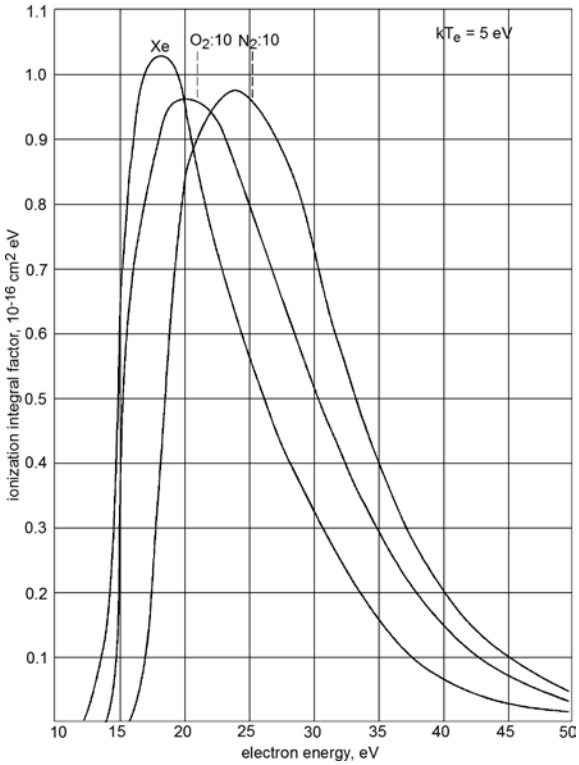

Figure 2-6: Calculated ionization integral factor $f_I = dn/n \cdot q_i \cdot W_e$ of Xe, O_2 and N_2 vs. the electron energy W_e ; the O_2 and N_2 curves are enlarged by a factor of 10 (11).

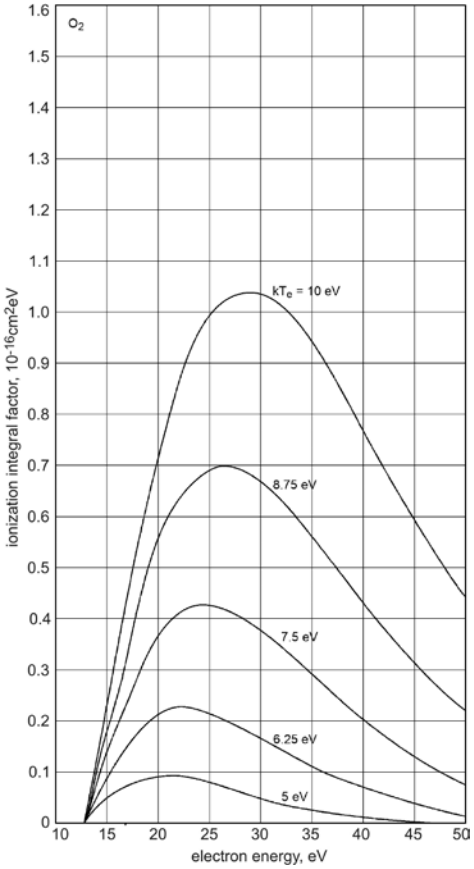

Figure 2-7: Calculated ionization integral factor of $O_2 \rightarrow O_2^+$ vs. the electron energy W_e for various electron temperatures kT_e (11)

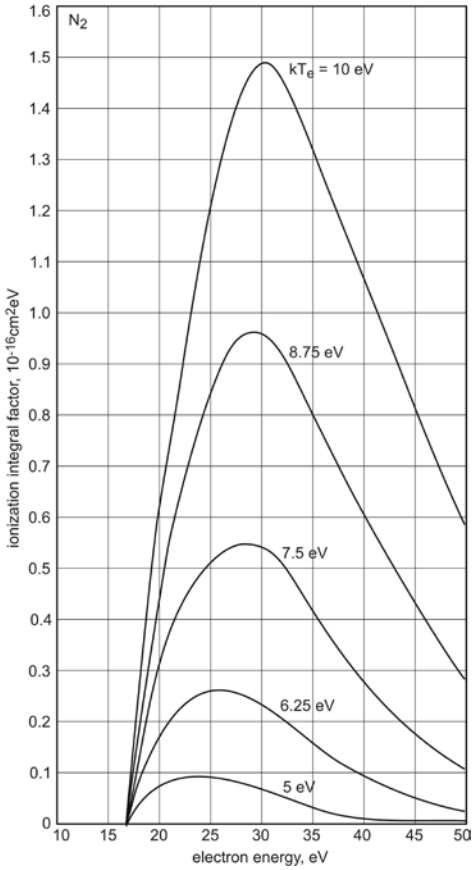

Figure 2-8: Calculated ionization integral factor of $N_2 \rightarrow N_2^+$ vs. the electron energy W_e for various electron temperatures kT_e (11)

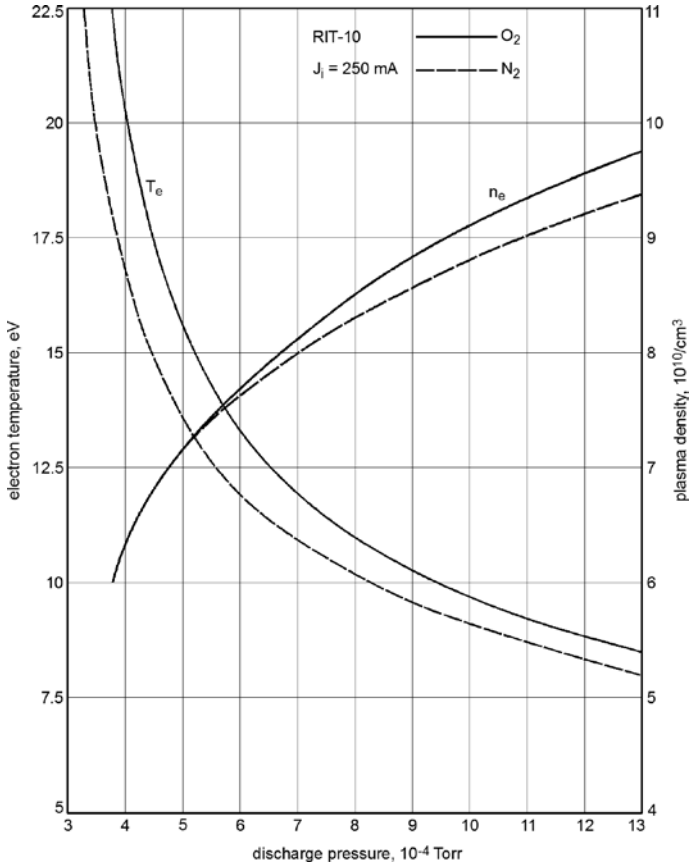

Figure 2-9: Calculated electron temperature T_e and plasma density n_e of O_2 and N_2 vs. the discharge pressure p_I in a RIT-10 engine running at 250 mA of beam current (11)

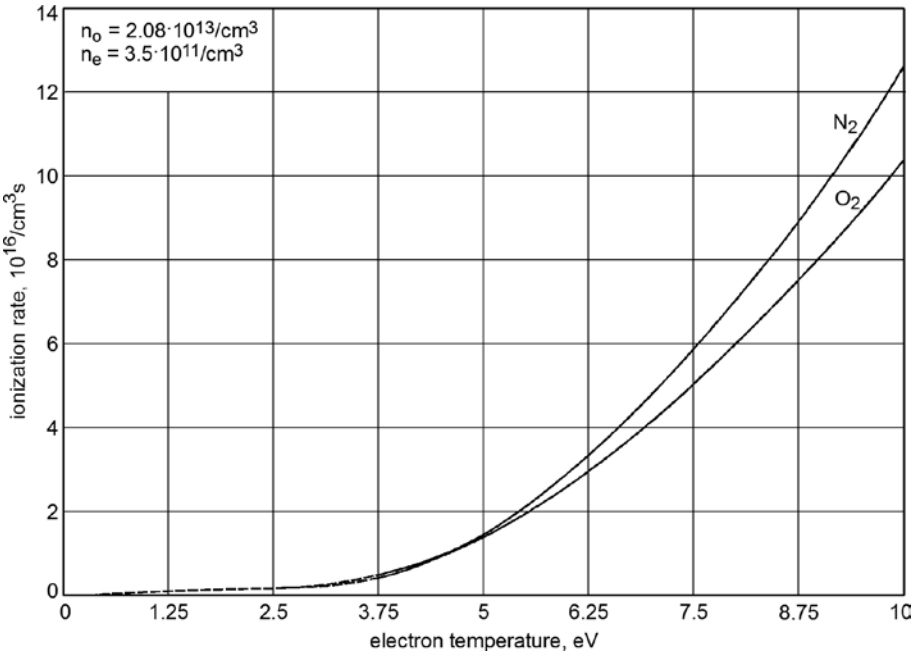

Figure 2-10: Calculated total ionization rate of N_2 and O_2 within a RIT-10 ionizer as a function of the electron temperature kT_e (11)

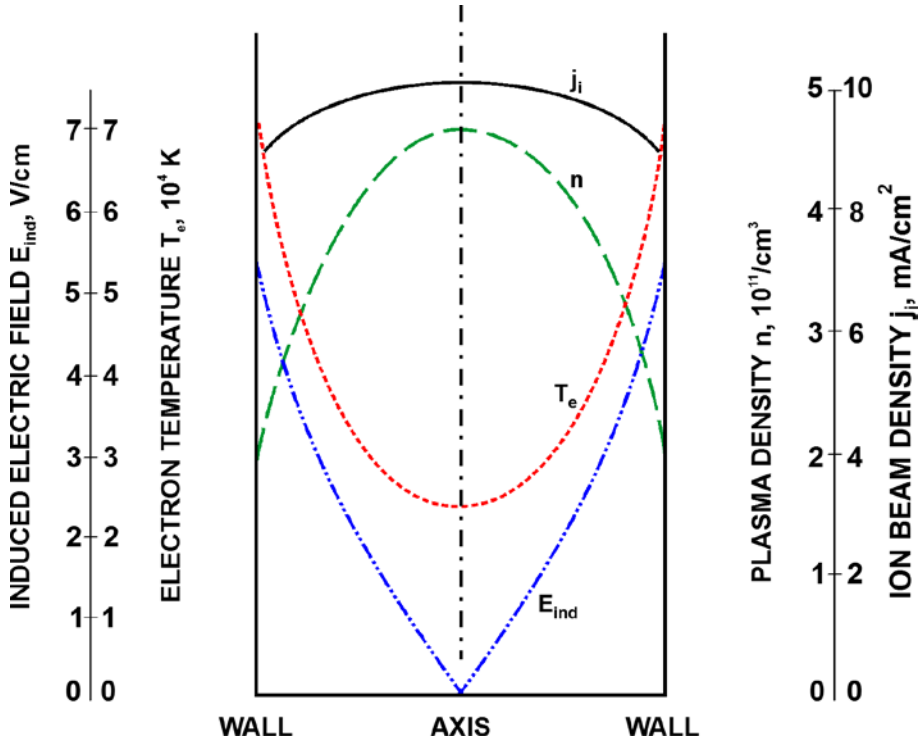

Figure 2-11: Radial distribution of the induced electrical field E_{ind} of a RIT-10 engine together with the electron temperature T_e, the plasma density n, and the extractable ion beam density j_i; the data have been obtained by Langmuir probes averaged over several test runs (9)

2.2.2. Plasma balance and yield

In the equilibrium, the number of generated ions and electrons (see above) must be equal to the number of carrier losses by recombination and by the extraction through the grid system (see below).

In a low-pressure discharge, i.e. in the plasma of a RIT-10 engine, ion-electron recombination takes place mainly at the walls.

To guarantee that the same number of ions and electrons reaches the (isolating) ionizer walls, a plasma-wall potential V_P is built up automatically, that accelerates the heavy ions and decelerates the very mobile electrons, i.e. repels all electrons of the Maxwellian distribution having less energy than eV_P. The plasma-to-wall current is called ambipolar current.

The plasma potential (being positive with respect to the wall) amounts to (12; 13):

$$V_P = \frac{kT_e}{2e} \cdot \ln\left(\frac{m_i}{2\pi m_e}\right) \qquad 2\text{-}4$$

Whereas m_i is the ion mass and $m_e$the electron mass. The logarithmic factor is for Xenon 10.55, for Oxygen 9.14 and for Nitrogen 9.01. Assuming an electron temperature of 5 eV, which is a good approximation for the RIT-10 as described above, the plasma potential in a Xe-discharge is about 26 V. Counting with $kT_e \geq 10\,eV$ for O_2 and N_2 (see above), the

potential V_P would in both cases exceed 45 V. The rf-power consumption of the plasma is required for the ionization, the ambipolar current losses and for dissociation and excitation processes.
The ionization power losses (10) are given by the ionization rate (see Equation 2-3) and the energy of the ionizing electrons W_e (see Figure 2-5) integrated over the discharge vessel volume V_I:

$$P_I = \int \frac{\partial^2 N_I}{\partial V \partial t} \cdot W_e dV \qquad 2\text{-}5$$

The ambipolar losses $P_A$depend on the ambipolar current density j_A, the plasma potential $V_P$and the surface of the ionizer walls A_I (without the extraction part) (14):

$$P_A = \int j_A V_P dA_I \qquad 2\text{-}6$$

With $j_A = q_{ion} n_i v_i$ and $v_i = \sqrt{2 q_{ion} V_P / m_i}$ one may write:

$$P_A = \sqrt{\frac{2}{m_i}} (q_{ion} V_P)^{-3/2} \cdot \int n_i dA_I \qquad 2\text{-}7$$

Hereby, $q_{ion} = 1.01\, e$ stands for the mean ion charge (at 1 % of doubly charged ions) (15); m_i means the mean ion mass (molecular and atomic ions), and $n_i = n_e = n$ is the plasma density.

Note that the plasma density decreases towards the walls due to the ambipolar current (see Figure 2-11).

The power losses by dissociation of the N_2 and O_2 molecules and by excitation collisions may be calculated by Equ. 2-3, too, provided that the related cross sections will be used for the dissociation and excitation rate.

Note that the very high dissociation energy of 9.79 eV (16) for $N_2 \rightarrow 2N$ and the very low cross-section of the dissociative ionization $N_2 \rightarrow N^+ + N$ (see Figure 2-2) suggest to neglect any dissociations of N_2; however, this statement is not valid for O_2 ($W_{diss} = 5.15\, eV$ (16), Figure 2-2).

As there exist several excitation levels (including rotation-vibrations), it is very difficult to calculate the excitation losses in the plasma.

In addition, non-plasma rf-power losses appear in a RIT-engine such as eddy currents in metallic thruster parts (e.g. in the screen grid) and dielectric losses in the isolating discharge vessel, both depending on the frequency and on material properties.

Therefore, it is practical to introduce the ion production costs w_i (given in eV/ion) that summarize all the named rf-power losses $P_{rf} = P_I + P_A + P_{diss} + \ldots$ necessary to generate one beam ion:

$$w_i = P_{rf}/I_i \qquad 2\text{-}8$$

This quality factor w_i, which will be used for RAM-EP modeling, depends mainly on the propellant species, the discharge frequency, the discharge pressure, and the thruster size.

Note that the extracted ion beam I_i depends on the extraction area A_{ex} of the first grid only, whereas P_I, P_A etc. depend on the volume V, or the wall surface A of the total ionizer, respectively. This fact suggests optimizing the discharge vessel length as well as the ionizer shape (cylindrical, semispherical, elliptical, etc.).

As a plasma-boundary transition sheath is built up in front of the extraction system in which the plasma ions are pre-accelerated and the electrons are decelerated, we get the extractable, i.e. by the plasma yield limited beam current (12) (13):

$$I_i = 0.6065 \cdot q_{ion} \cdot n_i \cdot \sqrt{\frac{kT_e}{m_i}} \cdot A_{ex} \quad with \quad A_{ex} = N\pi r_1^2 \qquad 2\text{-}9$$

Hereby N is the number of beamlets and r_1 the radius of the borings in the first grid.
Note that this plasma-saturation current cannot be calculated by the macroscopic operational parameters, i.e. the rf-power P_{rf} and the propellant flow rate $\dot{V}$. The microscopic plasma parameters n_i and T_e must be measured by a plasma diagnostic method (see Figure 2-3 and Figure 2-11). For a known or given beam current and a gas density n_o the plasma parameters could be calculated. For it the equation 2-3 (with $I_i = q_i dN_i/dt$) has to be equalized with the equation 2-9, taking V_I/A_{ex} into account.

As the result, the mean electron temperature T_e in a N_2 and O_2 discharge is 10 to 13 eV ($T_e(Xe) = 5\,eV$), whereas the mean plasma density n_e amounts to about $0.8 \cdot 10^{11}/cm^3$ ($n_e(Xe) = 3 \cdot 10^{11}/cm^3$). Following Equ. 2-4, the plasma potential V_P in N_2 and O_2 discharges is 45 to 60 V ($V_P(Xe) = 25\,V$).

2.2.3. Discharge characteristics

The performance mapping of the discharge yields the basic discharge curves $I_i(P_{rf}, \dot{V})$ as shown e.g. in Figure 2-4. The curves give the rf-power P_{rf} vs. the gas flow rate $\dot{V}$ needed to produce a beam current I_i as the parameter (provided that the grid system is able to extract the total plasma yield).

The curves show that the required rf-power could be throttled if the gas flow is increased and vice versa.

The analysis shows that the curves have a (nearly) hyperbolic shape (17):

$$I_i \approx a \cdot \left(P_{rf} - w_o \cdot I_i\right) \cdot \left(\dot{V} - g_o \cdot I_i\right) \qquad 2\text{-}10$$

(In the case of the former N_2 measurement of Figure 2-4, the P_{rf}-requirements increase somewhat again at high propellant flow rates which may be caused by increasing elastic collisions.)

The hyperbolic parameter a (given in $mA/W \cdot SCCM$) (11) increases strongly with the ion mass and affects the shape of the curves (which have in the case of Hg nearly a L-shape, note that Hg was used in the past as a propellant, but was replaced by Xe).

The horizontal asymptote $w_o \cdot I_i$ (with w_o in eV/ion) stands for all rf-power losses outside the plasma.

The vertical asymptote $g_o \cdot I_i$ gives the gas flow of the extracted ions only with $g_o = 13.93\ SCCM/A$ for all propellants.

If there are no other constraints (e.g. a limited power budget of a satellite), the optimum operational point (with the maximum overall efficiency of the thruster) is found at the bending points of the I_i-curves. When throttling the engine, the working line should cross the different bending points.

The discharge characteristics $I_i\left(P_{rf}, \dot{V}\right)$ give the main input for a RIT modeling.

2.2.4. Ion extraction and beam formation

The plasma ions are extracted out of the ionizer, accelerated, and focused to beamlets by three multi-hole electrodes namely the screen grid, the accel grid, and the decel grid or a decel ring (see Figure 2-12).

- **The screen grid** is biased on positive high voltage U_+ and it fixes the plasma potential which assumes at thrusting $U_+ + V_P$ (see Equ. 2-4) versus ground. Thus, the power output of the positive high voltage generator (PHV) should be $I_i \cdot U_+$, whereas the beam power would be $I_b\ (U_+ + V_P)$. Note that $I_b V_P$ is a contribution of the rf-generator. The beam current I_b is defined as the extracted ion current I_i minus the drain current I_{acc} on the accel grid.
  As been mentioned already, all ions entering the apertures of the screen grid are subjected to the electrostatic fields in the grid system. As this region is free of electrons, one can observe a positive space charge. To keep the discharge plasma quasi-neutral, an electron current, being equal to I_i, must be collected by the interspaces between the extraction holes of the screen grid.

- **The accelerator grid** is biased on negative high voltage U_- (NHV). Thus, the extraction voltage U_{ex} is given by U_+ plus the absolute value of U_-. Besides an extraction improvement, the negative accel grid stops also back-streaming electrons. The NHV power requirement amounts to $I_{acc} \cdot U_-$.

The drain current I_{acc} originates mainly from ion charge exchange processes (CEX) in the grid system. The slow CEX-ions may be attracted by the negative accel grid and sputter it by impact. This effect causes the lifetime limitation of the engine.

- **The decelerator grid** or decel ring is grounded, decelerates the beamlet ions down to the original energy of $q_i(U_+ + V_P)$, and protects the accel grid against back-streaming ions from the thruster exit or neighborhood (CEX-ions, neutralizer ions).
  If the extraction voltage U_{ex} is well adapted to the plasma yield, then the transition sheath, the plasma boundary and the upper equipotential planes are vaulted in a concave way (see Figure 2-12). This works as an ion-optical immersion lens and focuses the ions. In the optimum focusing case, the focal length should be equal to the accel length d. Then, the focal spot is found inside the accel grid borings, which consequently can be made smaller than the screen grid holes to save neutral gas losses (see below).

Note that the defocusing effect in the downstream, deceleration part of the grid system is less effective than the focusing effect due to the increased stiffness of the beamlets.

In the so-called over- or under-focused case, U_{ex} is either too high or too low. The plasma boundary vaults too much or not much enough into the plasma and the focal length is either too short or too long, respectively. In both cases, the accel drain current I_{acc} increases.

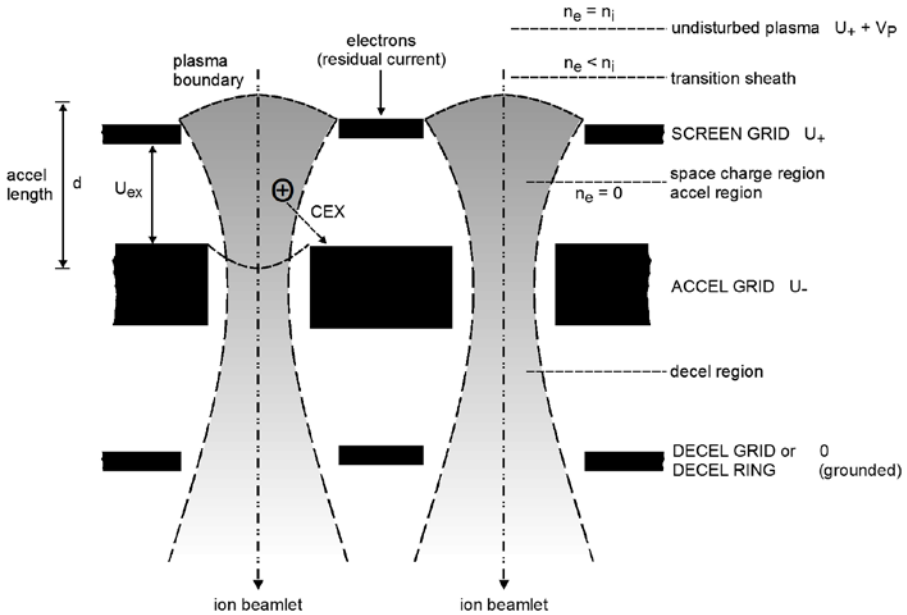

Figure 2-12: Sketch of the grid system of a RIT-engine with two exemplary beamlets (11).

Due to the space charge in the accel region, the extractable ion current I_i is limited by Langmuir-Schottky-Child's law (ε_0 = electric field constant) (18):

$$I_i = \frac{4}{9}\varepsilon_o \cdot \sqrt{\frac{2q_{ion}}{m_i}} \cdot \frac{U_{ex}^{3/2}}{d^2} \cdot A_{ex} \qquad 2\text{-}11$$

The designer of a grid system and the operator of an rf-engine must care for two conditions:

1st The ion current limited by the plasma yield (Equ. 2-9, depending on n_i, T_e or on P_{rf} and $\dot{V}$) should at least be equal to the space-charge limited current (Equ. 2-11, depending on U_{ex} and d). That means that all ions, offered by the plasma, should really be extracted, whereas too high extraction voltages don't enhance the beam current, but instead causes beamlet over-focusing and break downs between the grids as well.

2nd The grid geometry (grid thicknesses, boring diameters and interspaces) should be designed in such a way that for the envisaged working parameters ($\dot{V}$, P_{rf} and U_{ex}) the optimized focusing is maintained.

Figure 2-11 showed already that the ion current density $j_i = I_i/A_{ex}$ delivered by the rf-plasma has a rather flat profile across the extraction area. This is caused by the relation $j_i \sim n_i\sqrt{T_e}$ (see Equ. 2-9), since the electron temperature T_e increases and the plasma density $n_e = n_i$ decreases near the ionizer periphery. This flat $j_i(r)$ profile enables to keep the grid geometry unchanged across the total extraction system.

The optimum grid geometry depends not only on the desired beam voltage and the ion current density, but also on the propellant species. Transforming the Equation 2-11, one gets:

$$d \sim m_i^{-1/4} \cdot j_i^{-1/2} \cdot U_{ex}^{3/4} \qquad 2\text{-}12$$

It is clear, that not only the acceleration distance d but all geometrical data must be changed according to Equ. 2-11 and 2-12 with respect to the standard geometry of the RIT-2.5 (19), RIT-15 (20), and RIT-22 (15) (with e.g. 1.9 mm diam. of the screen grid holes (21)). In the case of the variation of the beam voltage, this rather simple scaling law has been proved already by ion trajectory simulation (IGUN-computer program) (22).

Thus, changing the propellant from Xe to O_2 or N_2 and keeping j_i and U_{ex} constant, the geometric values (grid thicknesses, extraction hole-diameters and interspaces) should be enlarged by a factor of 1.42 and 1.47, respectively according to Equ. 2-12 and using the masses of Xenon, Nitrogen and Oxygen. E.g., operating the thruster with an O_2/N_2 mixture, the screen grid holes should have diameters of 2.75 mm (for $j_i = 11.8\, mA/cm^2$ as RIT-22 with $175\, mN$). Naturally, the number of beamlets N should be reduced corresponding to $N \sim 1/d^2$ if the thruster size and the open area are kept constant.

Obviously, the neutral efflux through the grid system – and therefore also the propellant flow rate $\dot{V}$, the propellant efficiency, etc. – depend not only on the grids, but also on the gas species. To calculate the neutral gas flow, the gas flow conductivity L_G of a grid has to be defined ($d = grid\ thickness$, $r = hole\ radius$, $T_o = gas\ temp.\ in\ the\ ionizer$, $m_0 = mass\ of\ a\ neutral\ particle$) (23):

$$L_G = \frac{Nr^2}{\frac{3}{8}\frac{d}{r} + 1} \cdot \sqrt{\frac{\pi k T_0}{2m_0}} \qquad 2\text{-}13$$

In a two- or three-grid-system, the flow resistances $1/L$ are connected serial. Thus, one gets the total grid system conductivity L:

$$\frac{1}{L} = \frac{1}{L_{G1}} + \frac{1}{L_{G2}} + \frac{1}{L_{G3}} \qquad 2\text{-}14$$

Having L and the discharge pressure p_I (see above) the neutral gas-losses $\dot{V}_0$ can be calculated. To compute the total gas flow rate $\dot{V}$ the gas consumption of the ions $\dot{V}_i = 13.93\ SCCM/A \cdot I_i$ and V_0have to be added:

$$\dot{V}_0 = L \cdot p_i \ \ and \ \ \dot{V} = \dot{V}_i + \dot{V}_0 \qquad 2\text{-}15$$

2.3. Basic equations

The RIT-10 should be operated with Xenon (for comparison), Nitrogen, Oxygen, and with a combination of them. Looking at the q_i-curve of Figure 2-2 and regarding the high dissociation energy $W_{diss} = 9.76\ eV$ of Nitrogen, the portion of N^+ ions should be negligible. As the recombination rate of the collected Oxygen atoms from the atmosphere may be less than 100 % and due to the higher ionization cross sections of Figure 2-2, O^+ ions should not be omitted, even if the O_2^+ ions will be dominant.

The performance mapping tests yield the PHV-current I_i, the NHV-current I_{acc} (giving also the beam current $I_{Beam} = I_i - I_{acc}$) as functions of the rf-generator power P_{rf}, the total gas flow rate $\dot{V}$, the positive high voltage U_+, and the negative high voltage U_-.

The mass flow rate $\dot{m}$ can be calculated from the volume flow rate $\dot{V}$ taking the particle mass m into account (see Table 2-1).

The thrust F of an ion engine is given in general (18):

$$F = I_{Beam} \cdot \eta_{hom} \cdot \eta_{div} \cdot \sqrt{2\frac{m_{ion}}{q_{ion}}(U_+ + V_P)} \qquad 2\text{-}16$$

With the typical divergence efficiency $\eta_{div} = 0.98$, homogeneous efficiency $\eta_{hom} = 0.99$ (15) and a mean ion charge $q_i = 1.01\ e$, we get the simplification:

$$F = a \cdot \frac{I_{Beam}}{[A]} \cdot \sqrt{\frac{U_+ + V_P}{[kV]}} \qquad 2\text{-}17$$

Table 2-1 collates the thrust coefficients for the different ion species. With the same beam current and the same voltages, $O_2^+$and N_2^+ generate a thrust that amounts only 0.494 times and 0.462 times of the Xe^+-thrust, respectively.

The power consumption P of the thruster may be written as the sum of all individual contributions:

$$P = I_i U_+ + I_{acc} U_- + P_{rf} = I_i (U_+ + \beta U_- + \omega_i) \qquad 2\text{-}18$$

Note that I_{acc} or $\beta = I_{acc}/I_i$ depends strongly on $\dot{V}$, i.e. the pressure between the grids, because the drain currents is caused mainly by CEX processes. As the ambipolar power losses $P_A \sim 1/\sqrt{m_i}$ (see Equ. 2-7) increase with decreasing ion mass, we may suppose that the ion production costs for O_2 and N_2 are approximately 2.02 times or 2.17 times higher than with Xe (assumed that the other parameters like V_P and n_i are the same).

As usual, we write for the power or electric efficiency (18):

$$\eta_e = \frac{I_b (U_+ + V_P)}{P} \qquad 2\text{-}19$$

The propellant or mass efficiency is given by (18):

$$\eta_m = \frac{\dot{V}_i}{\dot{V}_i + \dot{V}_0} = \frac{13.93\ SCCM/A \cdot I_b}{\dot{V}} \qquad 2\text{-}20$$

As the gas conductivity of the RIT-engine used for the RAM EP-tests is $L \sim 1/\sqrt{m_0}$ (see Equ. 2-13), the neutral gas losses of O_2 and N_2 should be 2.02 times and 2.17 times, respectively, higher than those of Xe (see Table 2-1); thus, the propellant efficiency η_m will be significantly smaller in the case of the atmospheric gases.

This seems to compensate more or less the radical m_i-benefit in the formula of the specific impulse (18):

$$I_{sp} = \frac{1}{g} \cdot \eta_{div} \cdot \eta_m \cdot \sqrt{2 \frac{q_{ion}}{m_{ion}} (U_+ + V_P)} \qquad 2\text{-}21$$

We write again a simplification and include the I_{sp}-coefficient b in Table 2-1:

$$I_{sp} = b \cdot \eta_m \cdot \sqrt{\frac{(U_+ + V_P)}{kV}} \qquad 2\text{-}22$$

Note that O_2 and N_2 have a coefficient b being again 2.02 times and 2.17 times greater than the value of Xe.

	$\dot{V}/\dot{m}$ $\left[\frac{SCCM}{mg/s}\right]$	a $[mN]$	b $[s]$	L $[10^4\ cm^3/s]$	T_0 $[K]$
Xe	10.24	50.87	3849	3.756	~400
O_2	42.02	25.11	7797	8.291	~475
N_2	48.00	23.49	8335	8.863	~475
O	84.04	17.76	11027	11.725	-

Table 2-1: Comparison of atmospheric gases with Xenon including volume to mass ratio $\dot{V}/\dot{m}$ (at 273.15°K), the coefficients a and b for the thrust and specific impulse, the gas flow conductivity L at ionizer temperature T_0 (depending on P_{rf}), and the optimum discharge vessel length l_{opt} (see chapter 2.2.2).

2.4. Atmospheric model

The gas composition which has to be used during the gas mixture test campaign was calculated by the NRLMSISE-00- atmospheric model of Alta and ESA and crosschecked and verified by the Master of Science student Michael Becker (1). The gas distribution is based on the assumption of 200 km mission altitude and the solar activity, and a sun-synchronous orbit is taken under account. The individual values of the target time windows have been calculated and the average values of the mixture were determined. Two different configurations have been selected for the tests by ESA. The first composition represents the environmental condition calculated for the target height and mission window and the second mixture has 10 % Xenon in addition as a supporting gas. The behavior of the thruster and the advantages and disadvantages operated with these propellant mixtures should be investigated. The two derived compositions are given in the following lines.

- Mixture Composition 1 : 1.27 N_2 + O_2

  (55.95 % N_2 + 44.05 % O_2)

- Mixture Composition 2: (1.27 N_2 + O_2)+10 % Xe

  (50.35 % N_2 + 39.65% O_2 + 10 % Xe)

2.5. Plasma processes

This small chapter gives a rough overview of the main processes taking part in the discharge plasma. To demonstrate even more complex processes, including dissociation, the O_2 molecule was chosen.

2.5.1. Excitation

If an accelerated electron collides with an atom or molecule it transfers parts or all of its energy to the collision partner. If the transferred energy is lower or much higher than the ionization energy of the atom or molecule, one or more electrons can be lifted into higher energy orbits. The equations 2-23 to 2-25 describe the process of selected excitations.

$$O_2 + e^- \rightarrow O_2^* + e^- \qquad 2\text{-}23$$

$$O_2^+ + \mathrm{e}^- \rightarrow O_2^{+*} + \mathrm{e}^- \quad \textit{2-24}$$

$$O_2 + h\nu \rightarrow O_2^* \quad \textit{2-25}$$

For plasma discharge these excitations result in power losses but they cannot be fully avoided. The emitted light of the discharge, caused by the relaxation of the excited atoms, can be used for spectroscopic diagnostic of the plasma.

2.5.2. Ionization

The gathered energy of the electrons has to be high enough to allow a possible ionization. If the required energy is provided, the transferred energy can strike out an electron of the atom or molecule. The positive charge of the affected particle is increased by the amount of electrons stroked out of their orbits. In certain cases it is also possible that the atom or a molecule captures an additional electron and the resulting ion has not a positive but a negative charge. The equations 2-26 to 2-28 describe some of the possible ionization processes.

$$O_2 + e^- \rightarrow O_2^+ + 2e^- \quad \textit{2-26}$$

$$O_2^+ + e^- \rightarrow O_2^{2+} + 2e^- \quad \textit{2-27}$$

$$O_2 + e^- \rightarrow O_2^- \quad \textit{2-28}$$

For the used RF-Discharge the single ionization is the dominating process. Negative and or higher ionization grades are more or less negligible.

2.5.3. Dissociation

The dissociation is an important process for molecules inside of a plasma discharge, because if the molecule is dissociated, the former physical properties will be slightly different, for example the masses. Especially if the dissociation energy is in the same range as the ionization energy the dissociation might play a big role inside the discharge. The differing masses have a direct impact on the extraction, beam focusing and grid lifetime. Equation 2-29 is an example for the Oxygen dissociation.

$$O_2 + e^- \rightarrow O + O + e^- \quad \textit{2-29}$$

The reverse process is described in equation 2-30.

$$O + O \rightarrow O_2 \quad \textit{2-30}$$

2.5.4. Recombination

As shown in equation 2-31 the recombination process requires a third collision partner to comply with the momentum conservation. The particle densities inside a plasma discharge of an rf-ion-thruster are comparably low. Therefore the number of particle collision with the matching momentum and with an available electron in the capture cross section is quite low in the discharge volume. The recombination mainly takes place at the wall of the discharge vessel, as the wall acts as a collision partner and can also provide the required electron. This

was already validated by Langmuire probe measurements as mentioned in chapter 2.2.1 and in Figure 2-11.

$$O_2^+ + e^- + momentum\ partner \rightarrow O_2 + momentum\ partner \qquad 2\text{-}31$$

2.5.5. Disexcitation / Relaxation

The populated excitation states are meta-stable states. After certain times the lifted electrons will relax to deeper energy states or even their basic states, by emitting photons of the related energies. These emitted photons let the plasma glow. As describes above, these energies are mainly lost for the ongoing discharge process, but can be used for plasma diagnostic purposes. In several cases the excited atom or molecule can transfer its stored energy to another colliding atom or molecule. The following equation 2-32 describes the firstly mentioned case.

$$O_2^* \rightarrow O_2 + h\nu \qquad 2\text{-}32$$

3. Experiments

Test article is the RIT-10-EBB ion thruster as described in detail in (24). An EBB model of the RIT-10 was used in this test. It is equipped with an additional water cooling system, as higher power consumptions and therefore higher temperatures were expected for atmospheric propellants. The water cooling system is also necessary because of the usage of a direct thrust balance. To minimize the occurring thermal drift the whole system including the thruster is water-cooled. This water cooling won't be required for the flight hardware. The RIT-10 is an ion engine with a 10 cm in diameter ionizer and a classic three grid system. The thruster is optimized for a thrust level of 15 mN (Xenon).

The thruster has the same thruster parameters as the RIT-10 ARTEMIS. The ion optics and the discharge chamber as well as the radio frequency design parameters like inductivity and impedance are the same. The grid system and the interface between the discharge chamber and the extraction system were designed for the maximum flexibility and to simplify changing the parts.

The extraction system is made up of three grids as for the RIT-10 ARTEMIS. The grid system parameters like distance between the grids, grid thicknesses, and aperture or hole diameters are all kept unchanged.

For the tests with N_2+O_2 mixtures the thruster is equipped with an acceleration grid made up of Titanium instead of Graphite, which showed an excessive corrosion due to the chemical interaction with O_2. The Titanium grid has the same geometry parameters as the Graphite grid. The ion optics and the thickness are the same.

In comparison to the flight hardware, besides the water cooling, the thruster is heavier and cannot stand a vibration test. It is however much more flexible and the changes in the discharge chamber, radio frequency design (coil design, thruster internally installed capacitors) and extraction system can be performed very easily if required.

Besides the changing in the extraction system of the RIT-10-EBB, there was another modification done on the thruster/rf-generator. During the tests of the thruster with N_2 and O_2 in the section one and two of the activity, it was seen, that the thruster had very low impedance. It caused a limitation of the maximum rf-power, which could be matched to the thruster, as the rf-generator can work up to a specific current. A new rf-design was performed and an impedance transformation was carried out by installing some capacitors inside the rf-generator and inside the thruster. This resulted in lower currents in the coil but higher voltages. The optimized version of the RIT-10-EBB is named as RAM-RIT-10.

3.1. Experimental setup

The equipment list consisted of:

- RAM-EP10 Thruster
- Vacuum facility
- Pressure gauge
- Oscilloscope for measurement of rf-frequency
- Thrust balance
- Mass flow controller and pressure transducer
- Positive high voltage supply part of TPS 4
- Negative high voltage supply part of TPS 4
- Radio Frequency Generator "RFG-400 SN 01”
- Radio Frequency Generator voltage supply part of TPS 4
- Auxiliary voltage supply providing voltages for valves, MFCs and RFG-electronic
- Computers for data acquisition and thruster control
- Camera for grid erosion measurement
- Camera for documentation of visual inspection

3.1.1. Test setup

The test setup used for the entire test consisted of the test power supply of EADS, two different flow panels; the EADS thrust balance and the RAM-EP-10 Thruster. The Jumbo vacuum test facility has provided the environmental vacuum condition to operate the thruster. For the first and the second test session (N_2 and O_2 Test campaign) the flow panel from EADS was used. After the completion of these tests the flow panel was replaced by the new developed gas mixing panel. The total layout of the FCU and PSCU (TPS4) used during the whole test campaign is summarized in the following figures and described in more detail in the next chapters. The thrust balance could only be used in the first two test campaigns due to the limitations of the construction work of the new chemistry building directly next to the lab. The vibrational and oscillating loads created by the building machines prevent a possible and reliable measurement during the mixture test campaign. Several tries to measure a realistic value were not successful. Also the complete balance setup was misaligned by these loads; even in the night and without the daily noises the measured results were not acceptable and realistic. Therefore the thrust was only computed for this gas mixture test campaign.

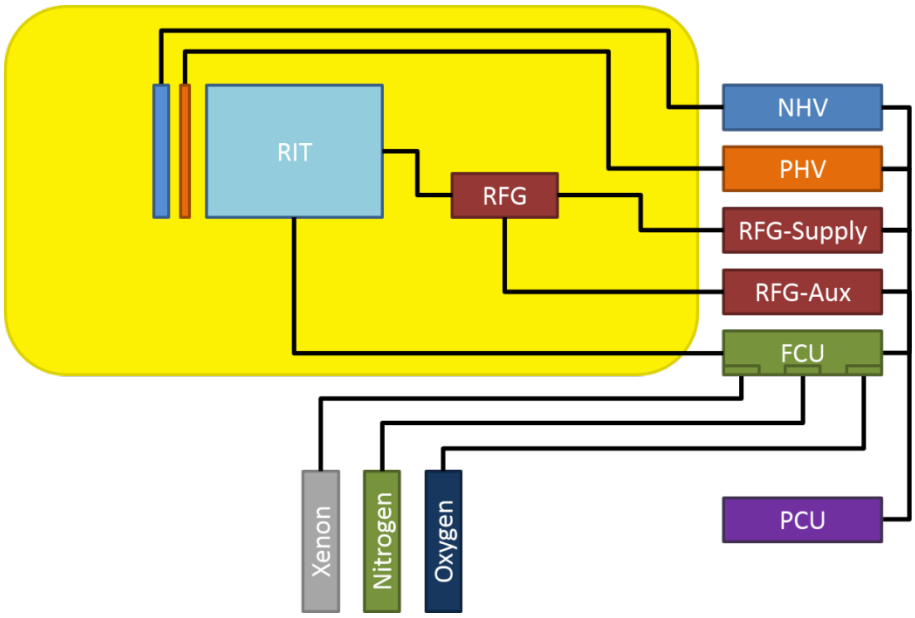

Figure 3-1: Overview of the schematically electrical setup

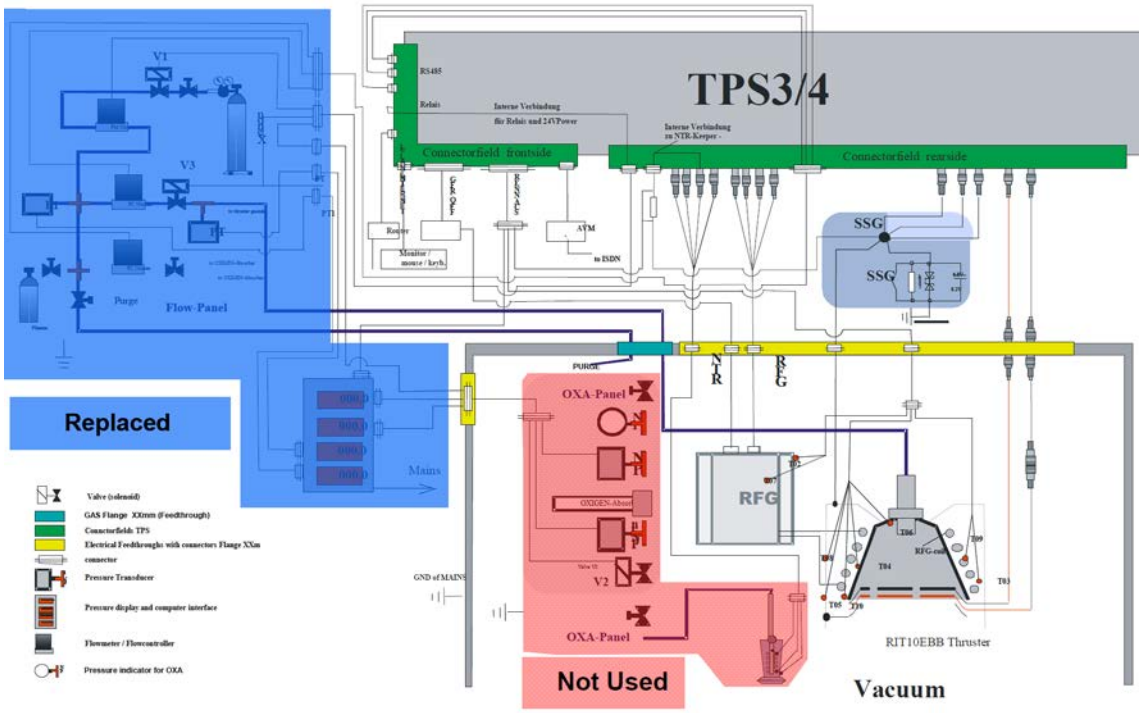

Figure 3-2: Electrical test setup and gas flow system

The blue marked flow section was replaced for the gas mixture test by the new flow board as described above. Figure 3-3 shows an overview of the setup used for the Oxygen and Nitrogen test campaign. The identical setup was used also for the mixture test campaign except the flow panel, which was replaced by the one shown in Figure 3-21.

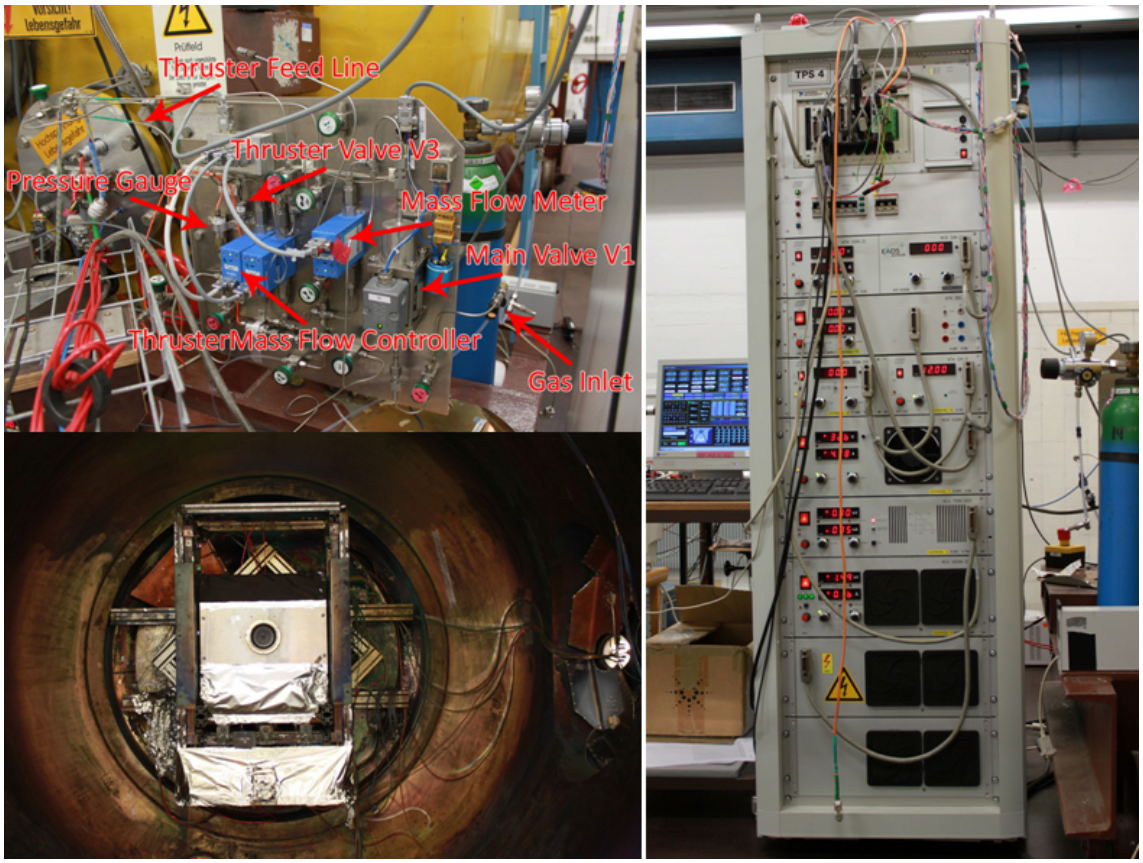

Figure 3-3: Test setup 1 for the Nitrogen and Oxygen test campaign

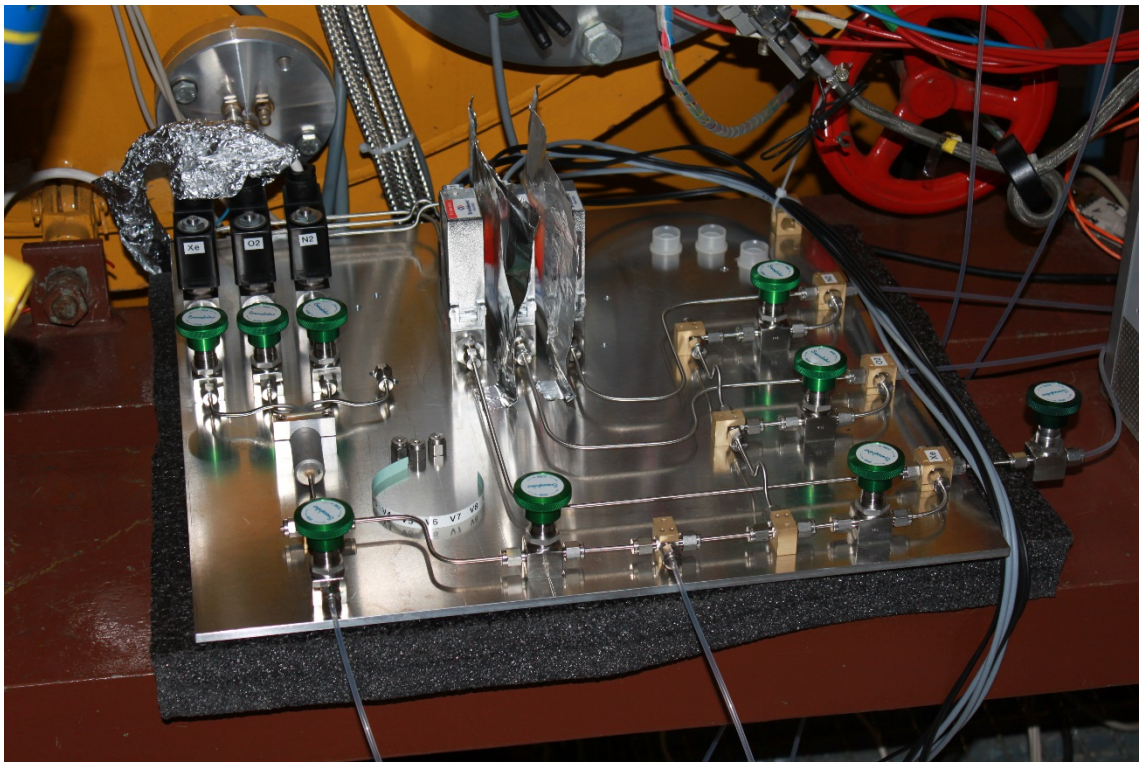

Figure 3-4: The new developed flow panel for gas mixing

3.1.2. Thruster setup

Test article is the ion thruster RIT-10-EBB /RAM-RIT-10, a Radio-Frequency-Ion-Thruster (RIT) which generates thrust by accelerating propellant ions in the electrostatic field of a grid system. The ions are generated in an alternating electro-magnetic field.

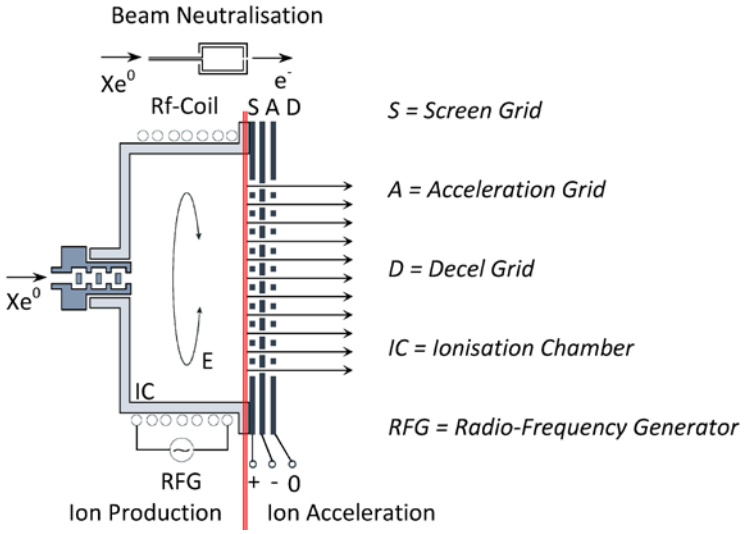

Figure 3-5: Scheme of RF-Ion Thruster

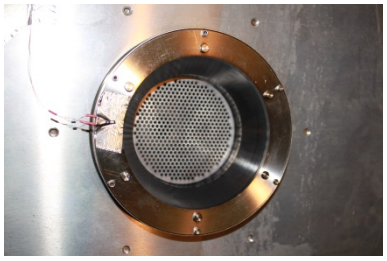

Figure 3-6: View on grid-system

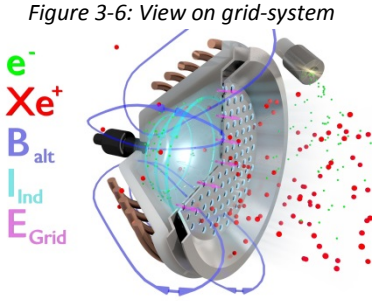

Figure 3-7: 3D-drawing by J. Mankiewicz

The propellant flow enters the ionizer via an isolator and a gas distributor. The ionizer vessel is made from an insulating material (quartz glass for these tests, Al_2O_3 will be used for space), and it is surrounded by the induction coil connected to rf-generator. The rf-generator is driving an AC current through the coil (Figure 3-5).

The axial magnetic field of the rf-coil induces an electrical eddy field, which accelerates the discharge electrons and enables them to ionize the Xe-atoms by inelastic collisions. Thus, an electrode-less, self-sustaining rf-gas discharge (plasma) is generated. By thermal movement the ions from the bulk plasma find the way towards the grid system. The rf-frequency is about 850-900 kHz. Finally the ions are accelerated in a system build-up of at least two grids. Concentric holes in these grids form a large number of single extraction channels. Every aperture of these channels is representing a single ion optical system. Their properties are determined by the diameters of the holes, the grid spacing and the applied voltages.

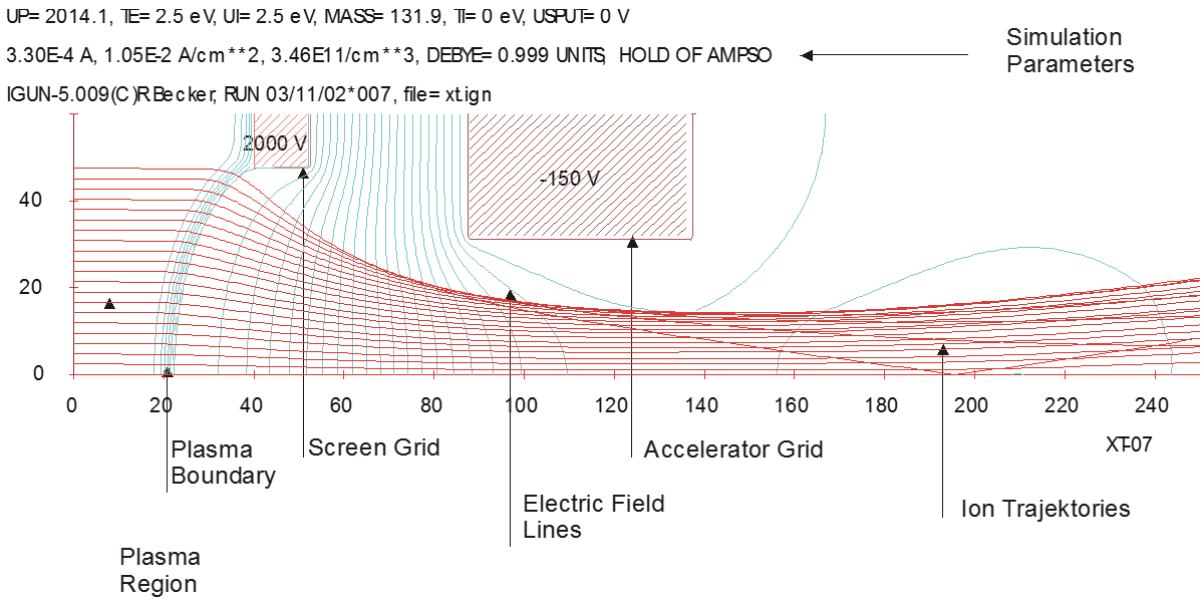

Figure 3-8: Simulation of one extraction aperture with Igun (simulated by R.Becker in 2002)

A positive voltage U_+ in respect to spacecraft ground is applied at the plasma sided screen grid and a negative voltage U_- at the second one. The negative voltage U_- at the "accelerator" grid prevents back-streaming of electrons from the downstream surroundings of the thruster into the ionization chamber and allows a higher voltage for ion extraction ($U_+ + |U_-|$) than for beam acceleration (U_+ only). Not all propellant atoms and or molecules leave the ionization chamber as ions, some remain neutral. The efflux of non-ionized atoms through the apertures of the grid system determines the propellant efficiency.

For the ignition of the radio frequency ion thruster it is necessary to insert free electrons to the discharge chamber. These electrons can gain energy through the rf-electric field to make an avalanche process to produce more electrons. The increase of the electron density stops when the discharge reaches the self-consistent state. The ignition of the RIT-10-EBB will be done using "pressure shock" as there will be no neutralizer used during this test campaign. In this method, the pressure in the thruster will be increased very fast to very high pressures. This, in combination with rf-power and (if necessary) high voltage, results in an increase in electron density which will be used for ignition. For the flight hardware this will be done by switching the polarity of the accel-grid to pull the electrons from the neutralizer to the discharge chamber. After the ignition the polarity of the accel-grid will be set to NHV again.

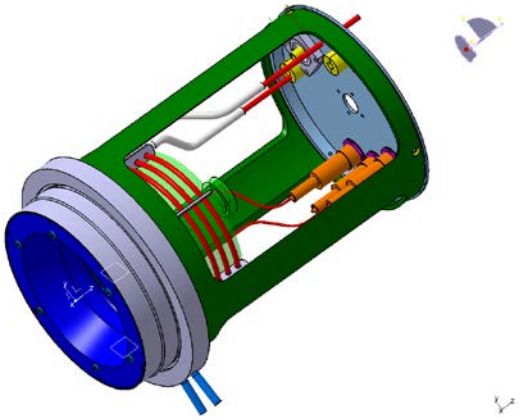

Figure 3-9: CAD-drawing of the RIT-10-EBB

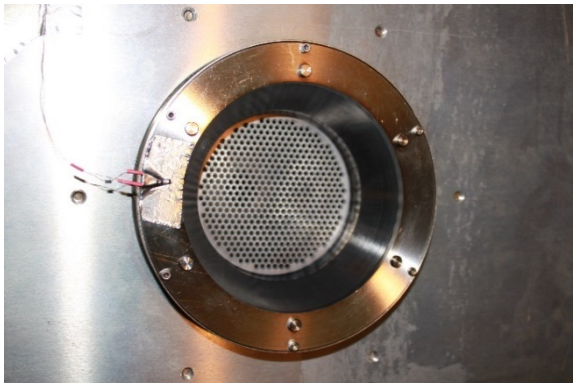

Figure 3-11: Mounted RIT-10-EBB frontal view

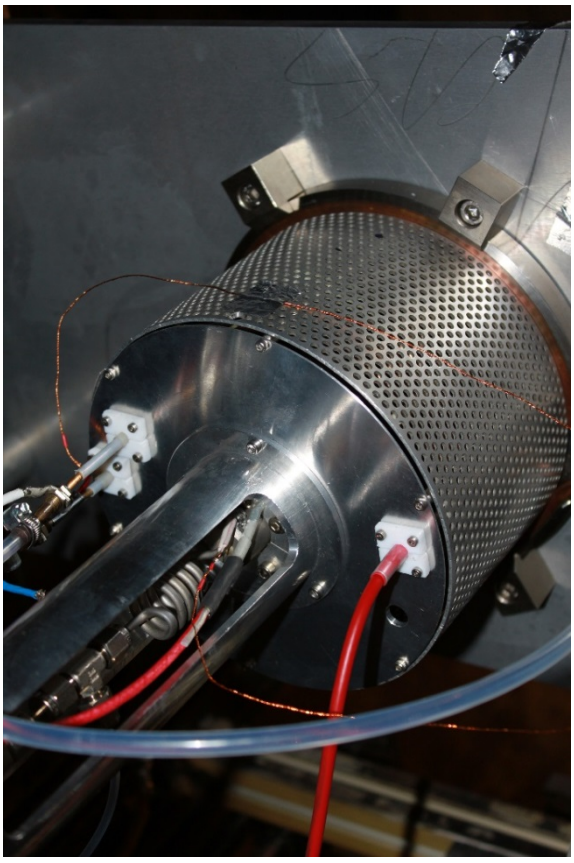

Figure 3-10: Mounted RIT-10-EBB from backside

An EBB model of the RIT-10 was used in these tests, with a water cooling system, as higher power consumption and therefore higher temperatures are expected for atmospheric propellants. Figure 6.3 shows the CAD-view and the mock-up of the RIT-10-EBB.

The EBB model has been used in two different configurations. The first configuration is similar to the original design with a Molybdenum screen grid and a Graphite accel grid. The coil is directly connected to the RFG with a short triax cable. This configuration was used for the Nitrogen and the Oxygen test campaign. During these tests a power limitation of the RFG was recognized based on the electrical limitations of the maximum allowed current. Also the Graphite grid was identified as a critical component due to the chemical erosion of Oxygen, which impacts directly the thruster lifetime. Based on these two facts an improved configuration has been realized (RAM-RIT-10) with a Titanium grid instead of the Graphite grid and also by the use of an impedance transformation in the rf-circuit. The voltage and the current were transformed and the available rf-power could be increased. The capacitor bank, the integration and the new Titanium grid are shown in Figure 3-12 to Figure 3-15 .

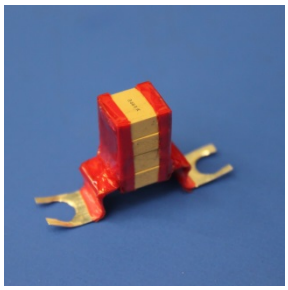

Figure 3-12: Capacitor-bank for impedance-transf.

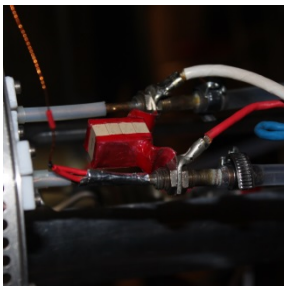

Figure 3-13: Integrated capacitor on rf-coil

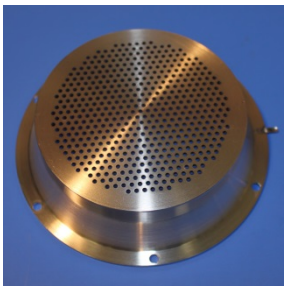

Figure 3-14: Isometric view of the Titanium accel grid

Figure 3-15: Top view of the Titanium accel grid

3.1.3. Test facility

The JUMBO test facility of the I. physics Institute of Giessen University was used as space simulator for the thruster testing and diagnostics. It has a diameter of 2.6 meter and a length of roughly 6 meters, with a usable volume of$\sim 30\ m^3$. The chamber is equipped with eight special designed cold heads and three turbo molecular pumps to achieve an effective pumping speed of up to 120.000 l/s for Xenon.

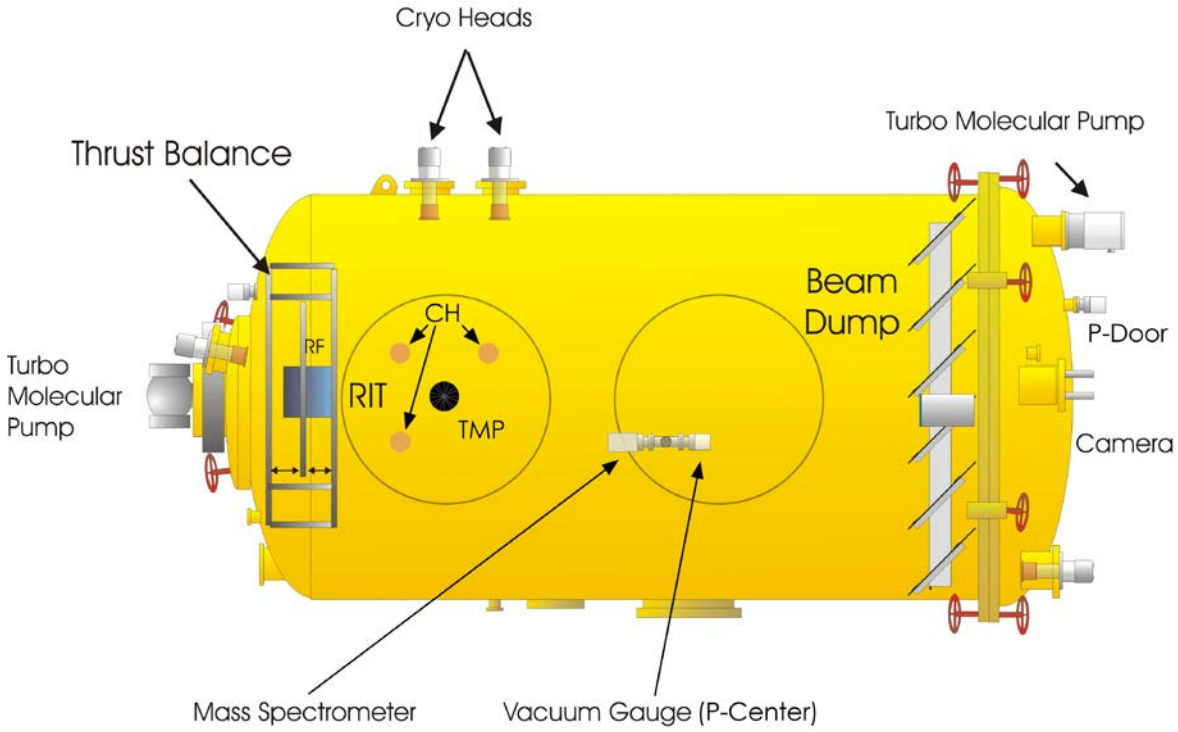

Figure 3-16: Schematic of the Jumbo test facility

The pumping system is arranged as follows:

- Rough vacuum is performed using a rough vacuum system at 2000 m^3/h, consisting of a Roots Blower backed by a rotary pump and separated from the chamber by an angle valve;
- Three turbo molecular pumps backed by rotary pumps with a total pumping speed of 4200 l/s Xenon,
- Cryo pumps system, consisting of a special system of eight cryo pumps. The cryo system has a pumping speed of $\sim 118.000\ l/s$ at 38 SCCM of Xenon.

The overall vacuum setup is drawn in the complete vacuum diagram, shown in Figure 3-17.

It is possible to operate thrusters running with nominal thrust without leaving the 10^{-6} mbar pressure range. Ultimate pressure without mass flow is below $4 \cdot 10^{-7}$ mbar. Two full range Pfeiffer vacuum PKR 251 gauges, consisting of a Pirani as 1st stage and a cold cathode as 2nd stage, are used to monitor the chamber pressure. One is located at the door with the beam dump (P-Door) and the other is located at the center of the Chamber (P-Center). They can be identified in Figure 3-16.

The vacuum gauges are factory calibrated for Nitrogen therefore a Gas Correction Factor is used for other gases. A water-cooled beam chevron type target is integrated, which is able to dissipate ion beams up to 50 kW at room temperature. To reduce sputter contaminations, the whole target is covered with Graphite tiles. Thruster mounting point is located inside the main chamber on the forward chamber door. All supply lines are connected to the thruster through feed-throughs located near to the thruster. At its mounting point, the thruster resides in the free beam region of the chamber, so that influences of the wall are as minimal as possible.

During thruster operation, the inside of the main chamber is monitored by a video camera installed outside. The camera has included a zoom objective with a zoom factor of max. 400x for fast inspection of the thruster. A set of large feed-throughs gives direct view onto the beam and onto the thruster mounted on mounting point.

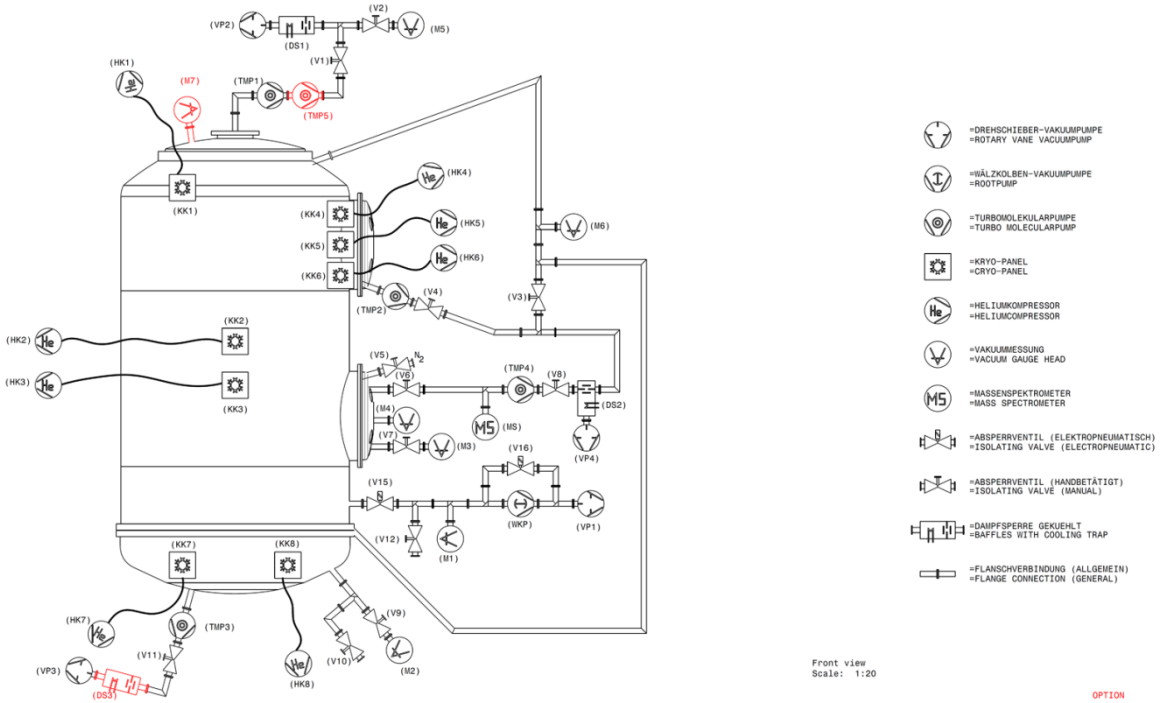

Figure 3-17: Jumbo vacuum diagram

3.1.4. Mechanical setup

The thruster is mounted on the EADS thrust balance, which is installed inside the Jumbo test facility at the thruster mounting point of the chamber. The balance and the thruster were located close up to the 2000 l/s turbo-molecular pump, installed in the center of the flange. This setup provides good environmental vacuum conditions. The mounting setup can be

seen in Figure 3-16. Some photos of the final setup are summarized below in Figure 3-18 and Figure 3-19 .

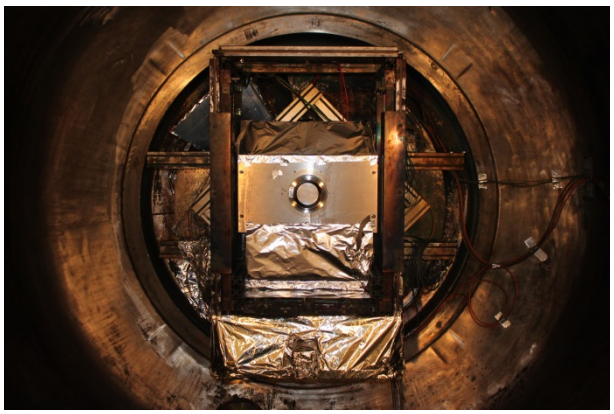

Figure 3-18: Total view on thruster setup

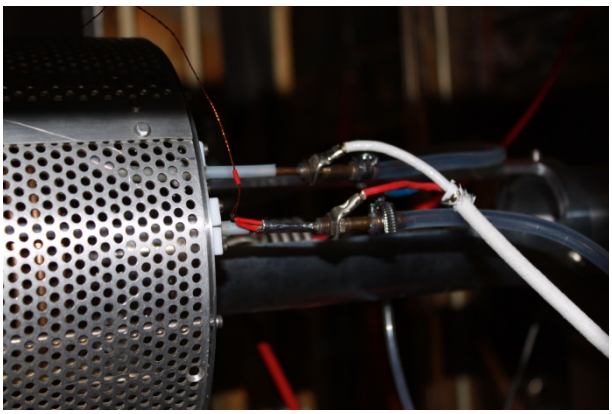

Figure 3-19: Side view of mounted thruster with the coil connection

3.1.5. Flow system

The flow system provides the propellant feed to the Thruster and the entire gas-consuming devices. It delivers an adjustable mass flow and a reduced outlet-pressure to supply the parts. Beside the mass flow regulation the flow system has to provide several valves to isolate and to purge the gas feed lines. For the complete test campaign two different flow setups have been used, a flow panel for single gases and a flow panel for defined gas mixtures. They are described in the next chapters.

3.1.5.1. Flow setup A: EADS – flow-panel for single gas

The EADS flow panel is suitable to operate a Thruster and a Neutralizer in parallel. The propellant feed is limited to a single gas bottle and the MFCs are calibrated for Xenon. To enable the thruster operation even with Nitrogen and Oxygen (not mixed) an additional junction and valves were adapted to switch between the gas bottles. The remaining inline pressure supports a seamless thruster operation even if the isolation valves of the bottles were completely closed (for a short time, during the switching, to prevent gas back streaming).

The Xenon is used to ignite the thruster, as the ignition with O_2 and N_2 was found to be difficult. The Xenon has much lower ionization energy and therefore needs lower pressures and electric field to start the self-sustaining discharge (ignition). After the ignition the isolation valves close the Xenon flow and open the N_2 or O_2 flow. This has been done manually.

At this flow panel the flow control unit (FCU) is represented by two digital flow controllers (MFC 1 -Thruster; MFC2 – NTR) for laboratory use. As a cross-check a flow meter (MFM1) is measuring the total flow into the thruster branch. The propellants are stored in commercial gas bottles and are interconnected for this test with the above mentioned isolating valves.

The propellants are stored in a bottle at high pressure. A pressure regulator unit reduces the high pressure to a constant low pressure. The propellant enters subsequently into a flow-control-unit which regulates the flow. The propellant enters into the discharge chamber of the RIT via the gas inlet. Two pressure transducers are used: for the thruster flow line one pressure transducer is located directly behind the propellant bottle and one at the thruster gas-inlet. The flow schematic of the EADS flow setup used for the test is shown in Figure 3-20.

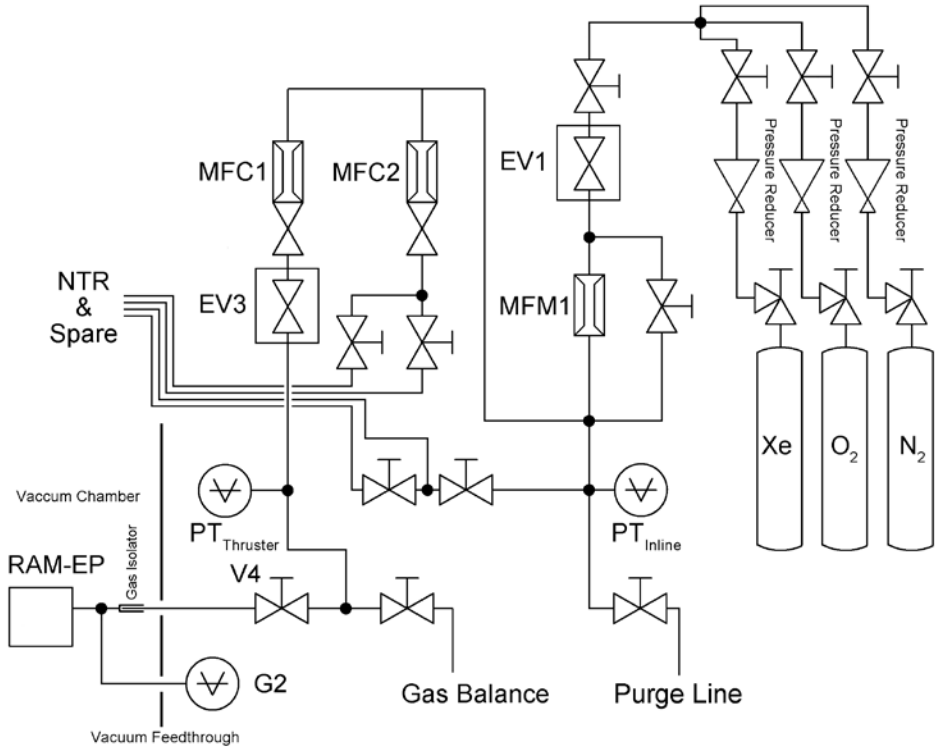

Figure 3-20: EADS flow panel used for RAM-EP

3.1.5.2. Flow setup B: Uni-Giessen – flow-panel for gas mixtures

For the gas mixture test a new gas flow table was developed, which can provide the required flow distribution capabilities. Three separate flow-branches were realized, which are united in a special developed mixing chamber (MC1). Manual and electrical valves isolate the not used branches and the purge line.

As mentioned in the last chapter the Xenon was always used to ignite the thruster, as the ignition with O_2 and N_2 was found to be much more difficult. In the new developed test setup the flow control unit (FCU) is represented by three digital flow controllers (MFC1 = Xenon, MFC2 = Oxygen and MFC3 = Nitrogen) for laboratory use. These three flow controllers provide single gas feeding and also the required gas mixing for the different test parts. The propellants are stored in commercial gas bottles.

Each propellant is stored in a pressurized tank. A pressure regulator unit reduces the high pressure to a constant low pressure. The propellant enters subsequently into a flow control

unit which supplies the thruster branch. The propellant enters into the discharge chamber of the RIT via the gas inlet.

Each propellant has its own pressure reducer, mass flow controller, electrical valve and manual valve. A completely separated single propellant usage and also a combined mixing were possible. The Flow Control Software allows individual control for each mass flow controller and supports automated ratio mixing. The propellant was mixed in the mixing chamber MC1, before it enters the final thruster branch. The manual valve V4 isolates the thruster from the flow panel. If required the flow panel could be easily extended to four MFCs. A schematic drawing of the flow control and mixing panel is shown in Figure 3-21.

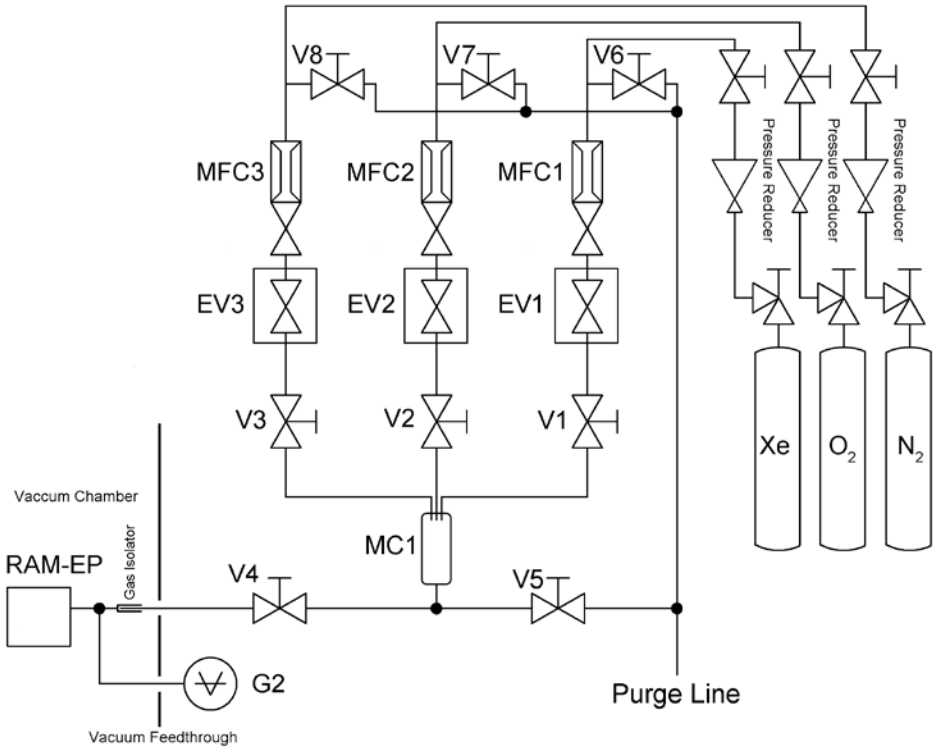

Figure 3-21: New gas flow and mixing panel for RAM-EP

3.1.6. Test power supply

The power supplies are all mounted on the EADS TPS4. The data are acquired via GPIB interface and recorded using LabVIEW™. This software enables to command and monitor all thruster operational procedures with the option to interrupt and modify the sequences.

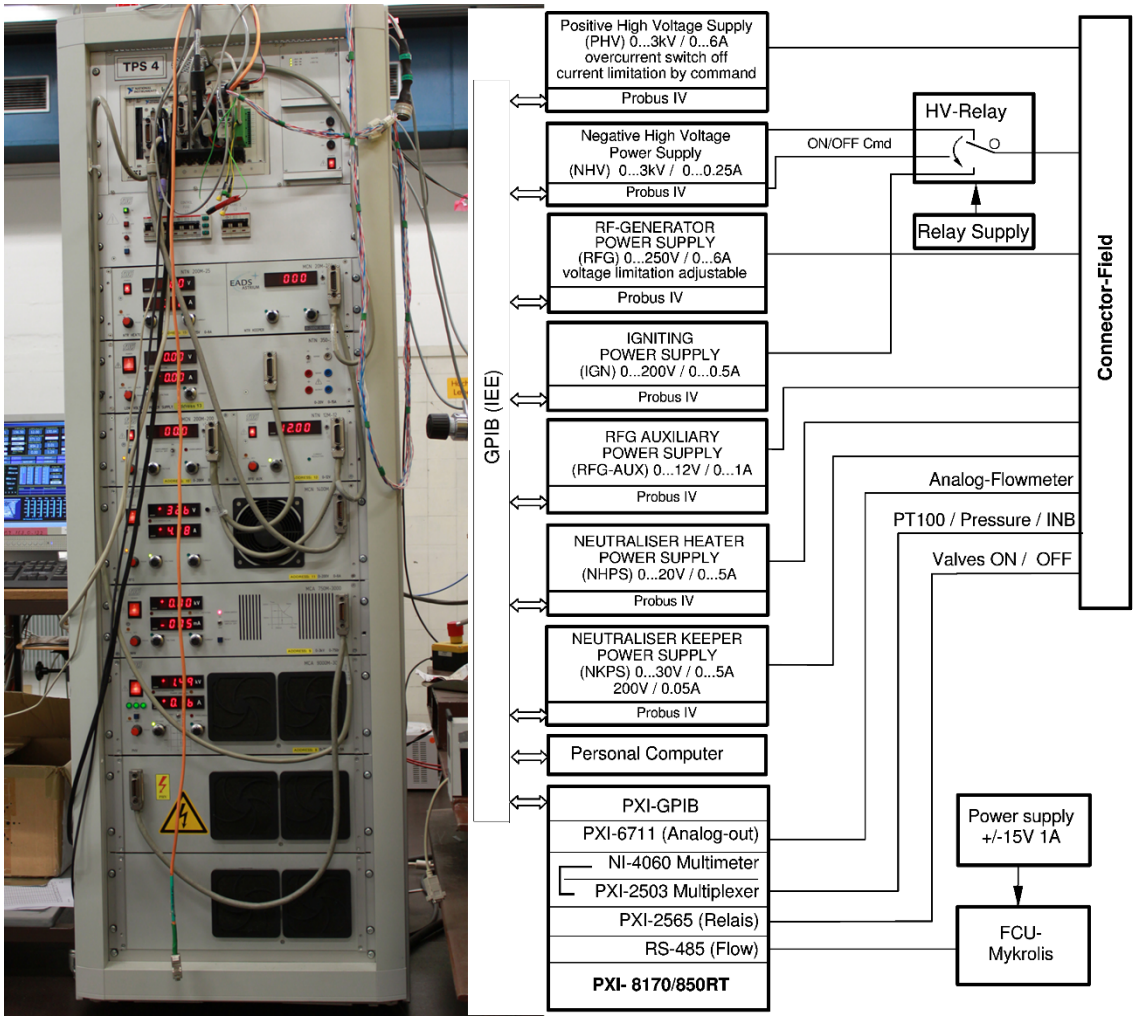

Figure 3-22: Test power supply (25)

3.1.7. Type and serial numbers of the used hardware

In Table 3-1 the type, the serial number and other details about the used hardware are listed. Table 3-2 provides further details of the mass flow controllers installed on the flow-panel.

Device	Type	Range	Ser. No.	Test
PHV	MCA 9000M-3000	3 kV / 9 A	12202-10-02 2002/11	1, 2 + 3
NHV	MCA 750M-3000	3 kV / 0.75 A	12202-02-01 2002/10	1, 2 + 3
RFG-Supply	MCN 1400M-200	200 V / 6 A	12202-04-02 2002/11	1, 2 + 3
RFG-Aux	NTN 12M-12	12 V / 1A	12202-05-01 2002/10	1, 2 + 3
Supply Voltages	RG 24-24	24 V / 1 A; 15 V /2 A; -15 V / 2 A	12022-11-02 2002/11	1, 2 + 3
Mass Flow Meter	Intelli Flow	50 SCCM Xenon	LC03093003	1 + 2
Mass Flow Controller	Intelli Flow	50 SCCM Xenon	LC03093002	1 + 2
Mass Flow Controller	Bronkhorst EL-FLOW	50 SCCM Xenon	M10200746A	3
Mass Flow Controller	Bronkhorst EL-FLOW	50 SCCM Oxygen	M11210559A	3
Mass Flow Controller	Bronkhorst EL-FLOW	50 SCCM Nitrogen	M11210559B	3
Isolation Valve (V1)	COAX MK15NCV4A	90 bar max	014480	1 + 2
Pressure Gauge Tank (Center 2)	IMR 265 Pfeiffer Vacuum	1E-06 to 1000 mbar	44045372	1, 2 + 3
Pressure Gauge Gas-Inlet	TPR 265 Pfeiffer Vacuum	5E-04 to 1000 mbar	44028881	1, 2 + 3
Pressure Gauge Tank (Door)	PKR 251 Pfeiffer Vacuum	1E-08 to 1000 mbar	44070252	1, 2 + 3
Pressure Gauge Tank (Center 1)	PKR 251 Pfeiffer Vacuum	1E-08 to 1000 mbar	44094535	1, 2 + 3
Pressure Meter	Maxi Gauge TPG 256A (PV)	6 Channel Pressure Meter	44139411	1, 2 + 3
TPS 4 Software	03 12.02.2006	flexible	N.A.	1, 2 + 3
Flow Control Software	Flow Control 1.0 2011	flexible	N.A.	3
Gas Balance	Mettler Toledo PB503-S/FACT	0-2000 mg	1126223987	1, 2 + 3

Table 3-1: Details on the used hardware

Description	Type	Range	Gas	Add. Gases	Interface	Calibration	SN
Mass Flow Controller	Bronkhorst EL-Flow F-201CV-050-ABD-11-V	50 SCCM +/-1%	O_2	Xe, N_2, Ar	A +D RS232	Nov. 2011	M11210559B
Mass Flow Controller	Bronkhorst EL-Flow F-201CV-050-ABD-11-V	50 SCCM +/-1%	N_2	Xe, O_2, Ar	A +D RS232	Nov. 2011	M11210559A
Mass Flow Controller	Bronkhorst EL-Flow F-201CV-050-ABD-11-V	50 SCCM +/-1% (25 SCCM Mode used)	Xe	N_2, O_2, Ar	A +D RS232	Feb. 2010	M10200746A

Table 3-2: Further details on the MFCs used on the gas mixing flow panel

3.2. Test schedule

The schedule of the work performed for this dissertation is based on half iterative test sequences. After a defined test section has ended certain checks, verifications and if necessary modifications where investigated and carried out. After that the test campaign was continued. The main test action has been separated in three different sections: tests with Nitrogen (N_2), tests with Oxygen (O_2) and finally tests with Nitrogen-Oxygen mixture (N_2+O_2). To gain further details on the performance of the Thruster operated with N_2+O_2 a high performance test was attached.

3.2.1. Test session with Nitrogen

The first test section with Nitrogen as a propellant has started with initial verification tests with Xenon to provide a comparable dataset for the following measurements and to verify the thruster performance compared to the original RIT-10 used on Artemis. After these tests with Xenon the performance mapping of the thruster operated with Nitrogen has been performed. Therefore the beam currents of 75, 100, 150, 200 and 234 mA have been chosen. Finally the Thruster has been operated for 10 hours continuously with Nitrogen.

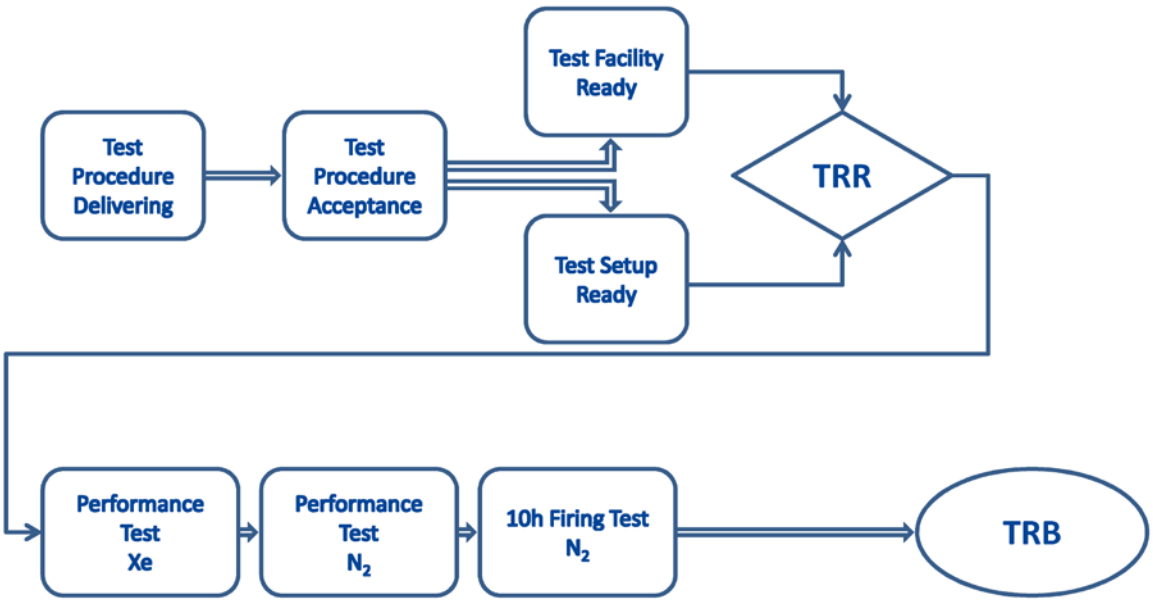

Figure 3-23: Test schedule for the first test section (Nitrogen)

No.	Description	Date
1	Visual inspection of selected thruster components	25.09.2010
2	First thruster grid inspection	25.09.2010
3	Q and L of rf coil	25.09.2010
4	Check of high voltage elements	25.09.2010
5	Visual inspection of complete engine	25.09.2010
6	Install engine in vacuum facility on thrust balance	25.09.2010
7	Vacuum pump down	26.09.2010
8	Cold flow test	08.10.2010
9	Performance test with Xe for 75 mA, 100 mA, 150 mA, 200 mA, 234 mA	08.10.2010 - 12.10.2010
10	Performance test with N_2 for 75 mA, 100 mA, 150 mA, 200 mA, 234 mA	13.10.2010 - 16.10.2010
11	Continuous thruster operation 10 h at 150 mA	16.10.2010
12	Shut down of engine and vacuum facility	16.10.2010
13	Open vacuum chamber and remove engine	18.10.2010
14	Thruster grid inspection	18.10.2010
15	Q and L of rf coil	18.10.2010
16	Check of high voltage elements	18.10.2010
17	Visual inspection of complete engine	18.10.2010
18	Grid erosion measurement	18.10-22.10.2010
19	Recalibration of gas flow controller	22.10-28.10.2010

Table 3-3: Test schedule for Nitrogen test campaign

3.2.2. Test session with Oxygen

After the successful end of the first test section the second test section was started. This second section is quite similar to the first section but this time Oxygen was used instead of Nitrogen. Prior to the performance mapping, a performance check with Xenon was performed at the reference beam current of 150 mA. The Thruster was operated with Oxygen at the same beam currents as mentioned above (75, 100, 150, 200 and 234 mA). A short 10 hours long run test was also part of this section. At the end a second performance check with Xenon was measured and the erosion measurement was performed. The detailed description of this test section is shown in Figure 3-24.

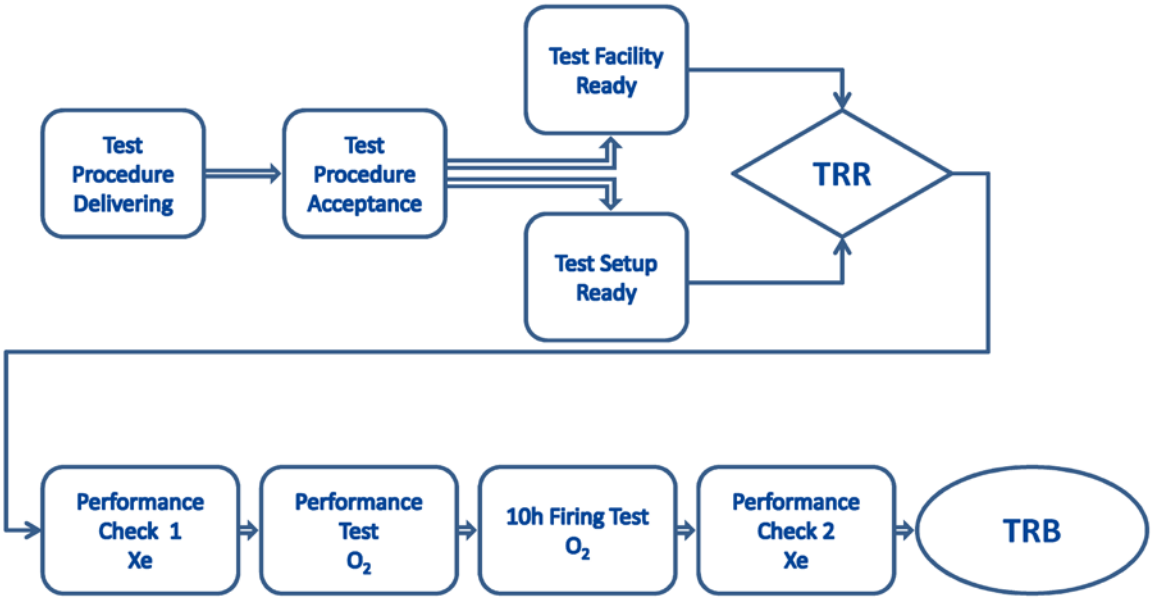

Figure 3-24: Test schedule for the second test section (Oxygen)

No.	Description	Date
1	Visual inspection of selected thruster components	11.11.2010
2	Q and L of rf coil	11.11.2010
3	Electrical check of high voltage elements	11.11.2010
4	Visual inspection of complete engine	11.11.2010
5	Install engine in vacuum facility on thrust balance	11.11.2010
6	Calibration of gas flow controller for O_2	12.11.2010
7	Vacuum pump down	15.11.2010
8	Cold flow test with O_2	17.11.2010
9	Performance check with Xe for 234 mA + contingency	17.11.2010
10	Performance test with O_2 for 75 mA, 100 mA, 150 mA, 200 mA, 234 mA	18.11.2010 – 24.11.2010
11	Continuous thruster operation for 10 h with O_2 at 150 mA	25.11.2010
12	Performance check with Xe for 234 mA	25.11.2010
13	Shut down of engine and vacuum facility	25.11.2010
14	Open vacuum chamber and remove engine	26.11.2010
15	Thruster grid inspection	27.11.2010
16	Q and L of rf coil	29.11.2010
17	Electrical check of high voltage elements	29.11.2010
18	Visual inspection of complete engine	29.11.2010
19	Grid erosion measurement 2	29.11.2010

Table 3-4: Test schedule for Oxygen test campaign

After the grid inspection of the second test section a high erosion rate of the grid system was noticed. This erosion cold be determined as a mainly chemical erosion. The second grid was originally manufactured out of Graphite, during the use of Oxygen as propellant the Graphite oxidizes and explains the high erosion rates. To increase the resistance of the grid system the Graphite grid was replaced with a Titanium grid. Also the observed power limitations were solved, by changing the impedance of the rf-circuit.

3.2.3. Test session with gas mixture

The third test section finally takes care about the gas mixtures which have to be used for the thruster operation. These mixtures are based on an atmospheric model, taking under account the wind, solar cycle and the orbit altitude. The expected gas distributions are defined to 1.27 times Nitrogen to Oxygen. The detailed schedule is given in Figure 3-25.

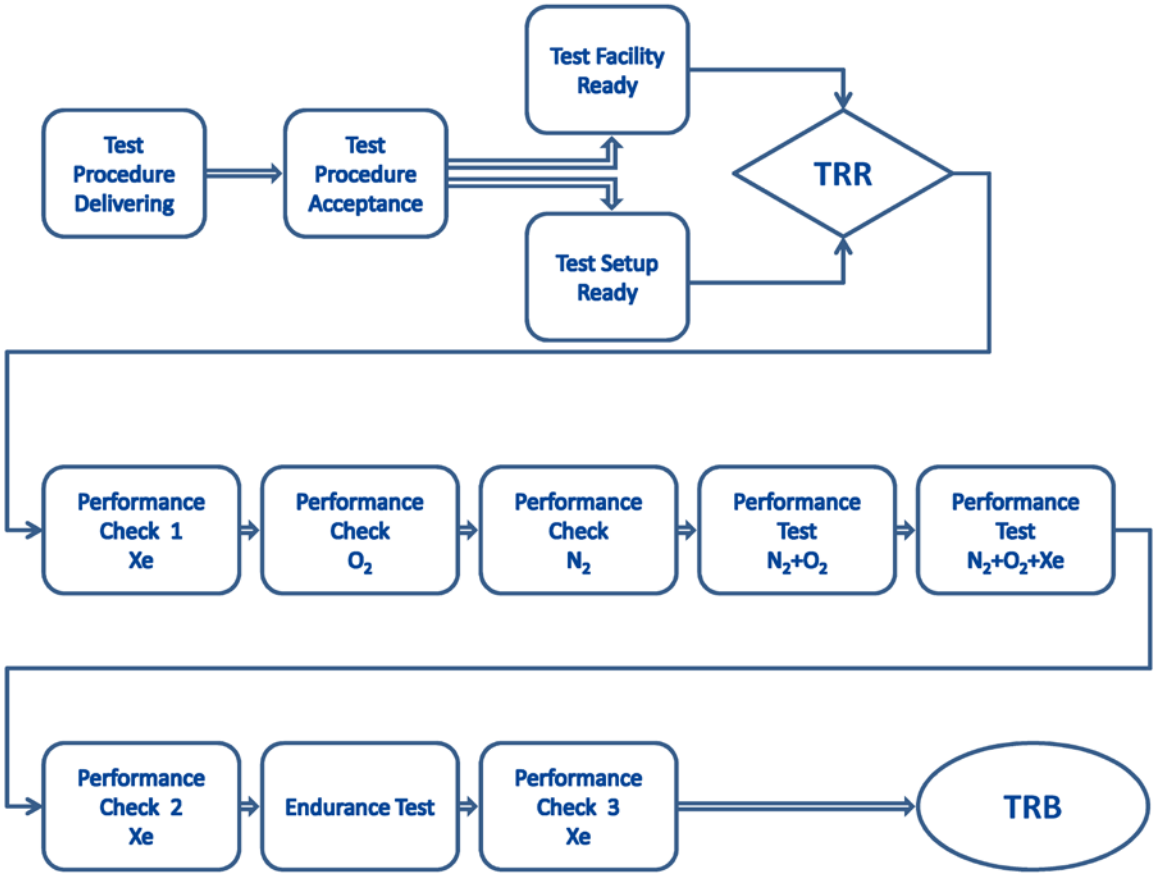

Figure 3-25: Schedule of the third test section

No.	Description	Date
1	Visual inspection of selected thruster components	15.12.2011
2	Q and L of rf coil	15.12.2011
3	Electrical check of high voltage elements	15.12.2011
4	Visual inspection of complete engine	15.12.2011
5	Install engine in vacuum facility on thrust balance	15.12.2011
7	Vacuum pump down	15.12.2011
6	Calibration check of gas flow controller for N_2	17.12.2011
7	Calibration check of gas flow controller for O_2	19.12.2011
8	Calibration check of gas flow controller for Xe	19.12.2011
9	Calibration check of gas flow controller for 1.27 N_2+O_2	19.12.2011
10	Calibration check of gas flow controller for (1.27 N_2+O_2) + 10 % Xe	20.12.2011
11	Cold flow test with N_2+O_2	22.12.2011
12	Performance check 1 with Xe for 150 mA + contingency	27.12.2011
13	Performance check with N_2 for 150 mA + contingency	28.12.2011
14	Performance check with O_2 for 150 mA + contingency	28.12.2011
15	Performance test with N_2+O_2; 75 mA, 100 mA, 150 mA, 200 mA, 234 mA	29.12-30.12.2011
16	Performance test with N_2+O_2 + 10% Xe; 75 mA, 100 mA, 150 mA, 200 mA, 234 mA	30.12-31.12.2011
17	Performance check 2 with Xe for 150 mA + contingency	31.12.2011

18	Shut down of engine and vacuum facility	31.12.2011
19	Remove grid system	03.01.2012
20	Grid erosion measurement 1	04.01.2012
21	Install grid system	05.01.2012
22	Vacuum pump down	05.01.2012
23	Continuous thruster operation for 500 h at 150 mA N_2+O_2	09.01-23.02.2012
24	Performance check 3 with Xe for 150 mA	24.02.2012
25	Shut down of engine and vacuum facility	24.02.2012
26	Open vacuum chamber and remove engine	25.02.2012
27	Thruster grid inspection	25.02.2012
28	Q and L of rf coil	25.02.2012
29	Electrical check of high voltage elements	25.02.2012
30	Visual inspection of complete engine	25.02.2012
31	Grid erosion measurement 2	25.02-06.03.2012

Table 3-5: Test schedule for gas mixture test

The development of a numerical model to describe the thruster performance with this atmospheric propellants based on the measured values is ongoing.

3.2.4. High performance test with N_2 + O_2

The high performance test was performed to identify the upper thrust limit of the actual design. The initial voltage test has delivered the necessary voltages for the NHV and PHV for this high performance test. Based on these voltages, the thruster was operated with a beam current of 300 mA, 350 mA and 400 mA. Different extraction voltages were used and the mass flow was varied. The required power consumption to generate the actual thrust level was determined and all electrical parameters were measured.

3.2.5. Special test procedures

The used main test procedures are summarized in this chapter. These procedures are the performance mapping and the grid measurement procedure. They are described here in more detail, because they are used more often in the test schedule. Procedures like the flow calibration and the cold flow test are described directly in the content of their test results. Also the electrical checks, concerning the conductivity, the resistance and the rf-parameters like the coil impedance are not part of this section. The usage of an ohmmeter, multi-meter and an rf-measuring-setup are assumed to be known and are not described in detail.

3.2.5.1. Performance mapping

For a specific I_{Beam}, (which in contact with a specific voltage defines a specific thrust) the rf-power and the mass flow are dependent to each other. This dependency function is characteristic for the thruster and the propellant. The performance mapping means the characterization of this dependency. Generally for a specific thrust, less power would be needed, the higher the gas flow is.

For the performance mapping, the I_{Beam} (thrust) should be kept constant and the gas-flow should be changed. The needed rf-power should then be measured. For higher gas flows the rf-power consumption would be less and for lower gas flows the power consumption would be higher. It should be emphasized, that this power is independent of the beam power ($= I_{PHV} \cdot U_{PHV} + I_{NHV} \cdot U_{NHV}$).

To keep the I_{Beam} (thrust) constant, a Beam Current Controller (BCC) or software can be used or the rf-power has to be regulated manually.

Generally the procedure follows a simple schedule. The thruster has to be ignited first if not already done. After the discharge and the pressure conditions have been stabilized the thruster can be switched to thrust-on mode (extraction voltages applied to the grids). The first beam current has to be commanded by adjusting the rf-power or by using a BCC. After that the mass flow has to be reduced stepwise to determine the lower mass flow limit (given by temperature and needed rf-power). Each step has to be measured. After the lower limit is reached the thruster has to be operated for a certain time as defined in the Table 3-6. Then, the mass flow is stepwise increases and the needed rf-power has to be adjusted. After the actual point has reached equilibrium the measurement has to be performed. The mass flow should be increased until the defined upper limits are reached.

The limitations for this test are the required RFG-power to achieve the desired beam current, the maximum thruster temperature and the accelerator-current, which is directly proportional to the grid lifetime. If one or more of these limits are exceeded the actual stepping has to be interrupted and the procedure has to be continued as described in the Table 3-6. The defined limit for the beam losses on the accelerator grid (NHV) is $\sim 10\ \%$ of the commanded beam current or ~ 15 mA. These values should not be exceeded or operated for longer intervals to prevent damage to the grid system.
In any case the thruster has to be operated at each individual point until the needed rf-power did not change any more to generate the actual thrust. This can take some minutes and depends on the setup. The thruster could be commanded much faster, but to measure reproducible values the steady state condition should be reached. If a malfunction or a thruster shut-off occurs, the thruster has to be reignited, operated for a few minutes to reach equilibrium and at least the last point has to be re-measured, before the remaining test can be continued. If the thermal condition of the thruster is too bad, a cool down might be required first.

1	Set U_{NHV} to -600 V and U_{PHV} to 1500 V
2	Set beam to 75, 100, 150, 200 and 234 mA, according to the correlated table
3	Reduce mass flow to find minimum mass flow per current level (rf-power or temperature too high or thruster shut-off)
3a	Operate engine for t=15 min (at least)

4	Increase mass flow in small steps ~ 0.5 SCCM
5	Operate engine for t=5 min, measure dataset (rf-power has to be nearly stable)
6	Repeat 4 and 5 until mass flow is increased to 16 SCCM, or I_{acc} is too high
7	Perform a back check to the first initial value to verify thruster health

Table 3-6: Performance mapping procedure

The thrusts are calculated from the ion current, ion voltage and ion mass according to the following formulas:

$$Thrust = \sqrt{\frac{2\times m_{Ion}}{q_i}} \cdot I_{Beam} \cdot \eta_{hom} \cdot \frac{(1+\cos\theta)}{2} \cdot \sqrt{(U_+ + V_P)} \qquad 3\text{-}1$$

$$Thrust = I_{Beam} \cdot \eta_{hom} \cdot \frac{(1+\cos\theta)}{2} \cdot \sqrt{\frac{2\times m_{Ion}\times(U_+ + V_P)}{q_{ion}}} \qquad 3\text{-}2$$

Both equations are identically, they are only written in different ways. The effects of beam divergence and the energy distribution of the ions (η_{hom} is > 0.999) are under the precision of the thrust-measurement (about 3 %).As long as nothing different is described, the thrust is calculated with $\eta_{hom} = 1$ and $\frac{(1+\cos\theta)}{2} = 1$. Also the dissociation of the molecules and the correlated thrust losses (described later in 5.3 in more detail) are not considered as long as not mentioned in another way. The given equations (X+Y) can be used in a superposition, to calculate the thrust of gas mixtures. Therefore the total beam current is spread up into the single beam currents of each molecule/gas type and multiplied by the correlated masses. The ratio of these individual currents is computed, based on the commanded flow distribution.

3.2.5.2. Optical grid measurement

The optical grid measurements are an important and useful method to exam and measure the hole-diameter of an aperture even without touching it, it is also not necessary to disassemble the grid system. The alignment of the grids is not affected nor the grid health. The grid system has to be dismounted from the thruster carefully by loosening the six screws at the outside of the grid system. The measurement setup consists of a revolving table with an attached lateral movable arm. The high resolution camera has a fixed focal length and is mounted on this arm (Figure 3-31). The specs of the camera are given in Table 3-7. The distance between the camera and the revolving table can be adjusted with a precision thread for fine regulation and by loosening the fixing structure and by shifting the arm by hand, to change the distance in a wider range. This might be necessary to cover the top and bottom measurements of the assembled grid system. The grid system has to be placed on the revolving table and the upwards facing grid has to be covered with the grid-mask (Figure 3-33) to identify the relevant holes. The selected holes of interest are shown in Figure 3-32.The camera has to be aligned to the masked holes and the distance has to be adjusted for each single hole to focus on it. A picture of the actual hole has to be taken and to be saved according the defined name-structure, to guarantee a correct identification during the

post processing. The naming convention is defined to be two to three letters plus a number. The first letter indicates the branch (A, B or C), the second and third describe the grid (AS= accel screen-side, AD = accel decel-side, D = decel and S=screen) and finally the number defines the hole. For example the hole-number 3 of the branch B in the accel grid, measured from the screen side, has the name BAS3. After the picture is taken, the next hole has to be photographed and so on until all selected holes are measured. By changing the distance of the camera, the inner grid has to be accessed and measured and afterwards the grid system has to be rotated to grant access to the other grid side. When all pictures are taken, the grid-system has to be reinstalled in the thruster. The calibration has to be performed by taking photos of defined slits from 0.5 to 2.5 mm in 0.5 mm steps (Figure 3-26 to Figure 3-30). The pixel to length ratio has to be measured and computed by the use of the measuring tool of Photoshop 5 Extended and should be 1 pixel = 0.0023 mm. The post-processing of each individual picture including the measurement with the ellipse-measuring tool of Photoshop has to be performed, the measured values exported and processed with excel. If possible also the edge diameter and not only the inner hole-diameter have to be measured. To indicate the measured selection, it has to be marked with a color (the rest of the picture remains black and white, see Figure 3-34). The complete procedure is summarized in the following Table 3-8.

Figure 3-26: 0.5 mm

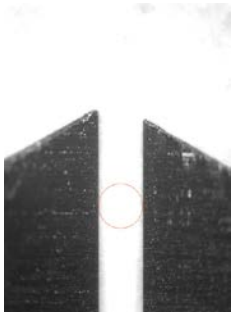

Figure 3-27: 1.0 mm

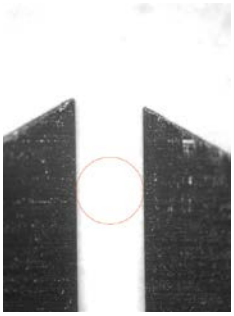

Figure 3-28: 1.5 mm

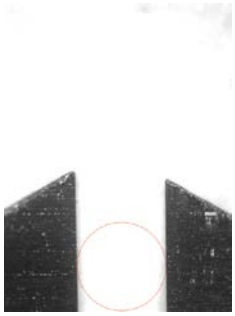

Figure 3-29: 2.0 mm

Figure 3-30: 2.5 mm

Camera	Pixelink Firewire System monochrom Resolution 3000 x 2208 pixels Sensor size 10.5mm x 7.7mm
Objective	SILL 100mm mounted via adapter ring Linearity: deviation < 0.01% Object size 6mm x 6mm
Settings for test	Used camera resolution: 3000 x 2208 pixel (10.5 x 7.7 mm, sensor size) (5.5mm x 5.5mm, object size)

Table 3-7: Details of the Pixelink camera

1	Remove grid system (the use of glows during the complete sequence is recommended)
2	Place it on the revolving table

3	Check and initialize the measuring setup
4	Take calibration pictures of slits with 0.5 to 2.5 mm with 0.5 mm steps
5	Adjust distance between camera and screen grid to focal length
6	Take six photos starting at point A1 following A/-A Axis from accelerator grid. Convention for naming: AAS1…AAS6
7	Take six photos starting at point B1 following B/-B Axis from accelerator. Convention for naming: BAS1…BAS6
8	Take six photos starting at point C1 following C/-C Axis from accelerator grid. Convention for naming: CAS1…CAS6
9	Redo this procedure for the screen, decel and accel grid (upstream). The naming will change to AS, AD, and AAD (for Axis A).
10	Mount the grid system back to the thruster
11	Post-process pictures with Photoshop end export tables
12	Post-process tables with excel

Table 3-8: Summarized measurement schedule for the optical grid measurement

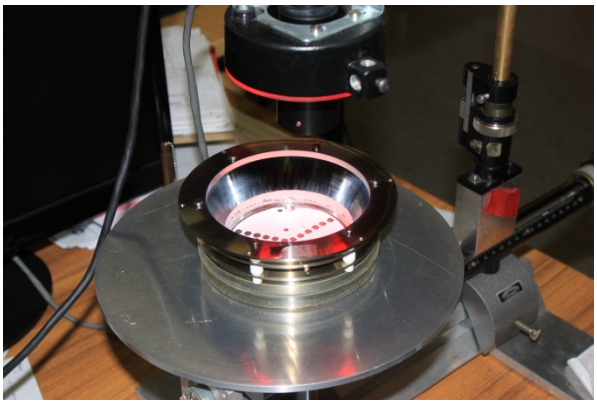

Figure 3-31: Grid measurement setup

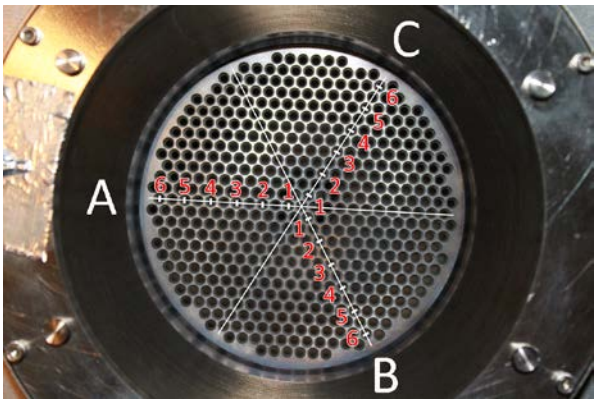

Figure 3-32: Frontal view of grid with marked holes

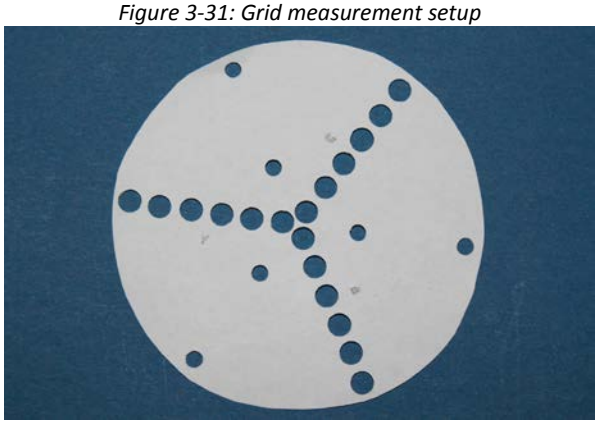

Figure 3-33: Paper grid-mask to identify holes

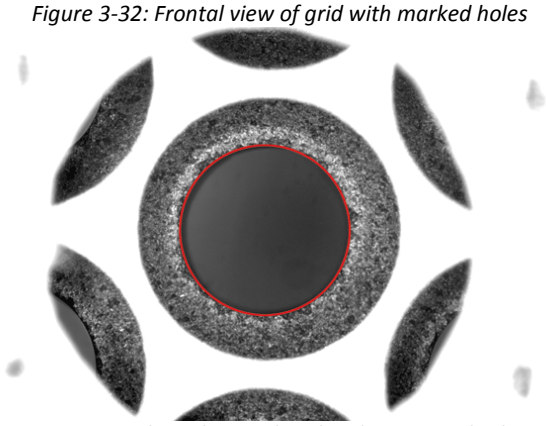

Figure 3-34: Hole in the accel grid with measured selection

4. Test results

This chapter presents the measured data of the individual campaigns. All the described procedures and schedules have been performed step by step and the resulting data has been recorded and post-processed. The correlated errors, which have been calculated, are left out for readability reasons; there will be just one example for each kind. The detailed relevant error datasets are provided in the discussion in the Table 5-4 to Table 5-8.

4.1. Flow board calibration

For the first test sessions the original flow board of EADS has been used. This flow panel can supply a neutralizer and a thruster with the same propellant in parallel. The gas-flow-controllers are Millipore devices and several isolation valves are available. The calibration of this ready assembled flow panel has been performed at the beginning of the test campaign. The different calibration measurements were repeated for each gas distribution. After these measurements had been done, the correlation and calibration tables were calculated. Therefore the mass flow controller was operated with different mass flows and the amount of gas vs. time was measured with the gas balance. The gas balance is a modified Mettler Toledo device with a mounted recipient. At the beginning of each measurement the gas recipient was evacuated and the balance zeroed.

The gas flow control system is calibrated to ensure the precise amount of the gas flow. The calibration was done with the help of a gas balance. In the Figure 4-1 the test setup and gas balance is shown. The gas flows through the commercial gas bottle and gas flow controller to a small gas recipient mounted on the balance instead of the normal weighting plate. In the beginning of each measurement the whole system is purged until the measured weight did not change anymore. Then the purge valve was closed and the balance was zeroed. The individual set points were commanded and the thruster line valve was opened. A Clock counter started in parallel to the valve opening. The weight of the incoming gas was measured at different time stamps as described in Table 4-1, Table 4-2 and Table 4-3. This was done for each mass flow starting from 0.5 V to 2.5 V in steps of 0.5 V. The first two values were not taken into account for the calibration due the error of the valve opening. After these initial values the flow is stable and linear.

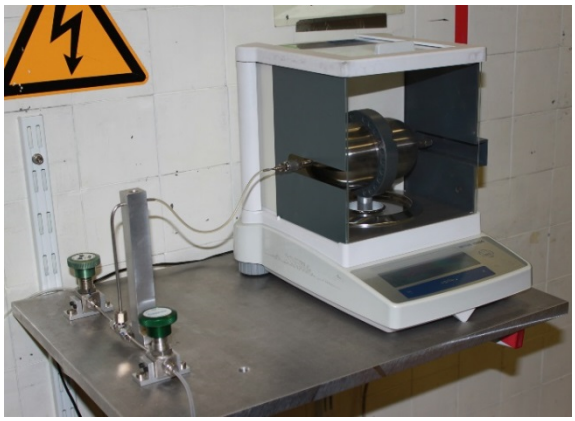

Figure 4-1: Gas balance from Mettler Toledo with a resolution of 1 mg

Time [s]	Flow 0.5 V [mg]	Flow 1.0 V [mg]	Flow 1.2 V [mg]	Flow 1.5 V [mg]	Flow 2.0 V [mg]	Flow 2.5 V [mg]
0	0	0	0	0	0	0
60	109	137	145	165	194	224
120	128	186	206	243	302	363
180	146	235	265	322	408	500
240	165	283	325	399	515	636
300	184	331	385	477	621	772
360	203	379	444	553	728	908
420	222	428	503	632	832	1044
480	240	476	563	708	938	1180
540	259	524	622	785	1043	1315
600	278	572	682	862	1148	1451
660	297	621	741	939	1254	1585
780	335	717	858	1092	1464	1855
900	373	814	976	1246	1674	2125
1200	468	1052	1271	1628	2198	2796
2400	845	2007	2447	3149	4285	5473

Table 4-1: Calibration data for Xenon

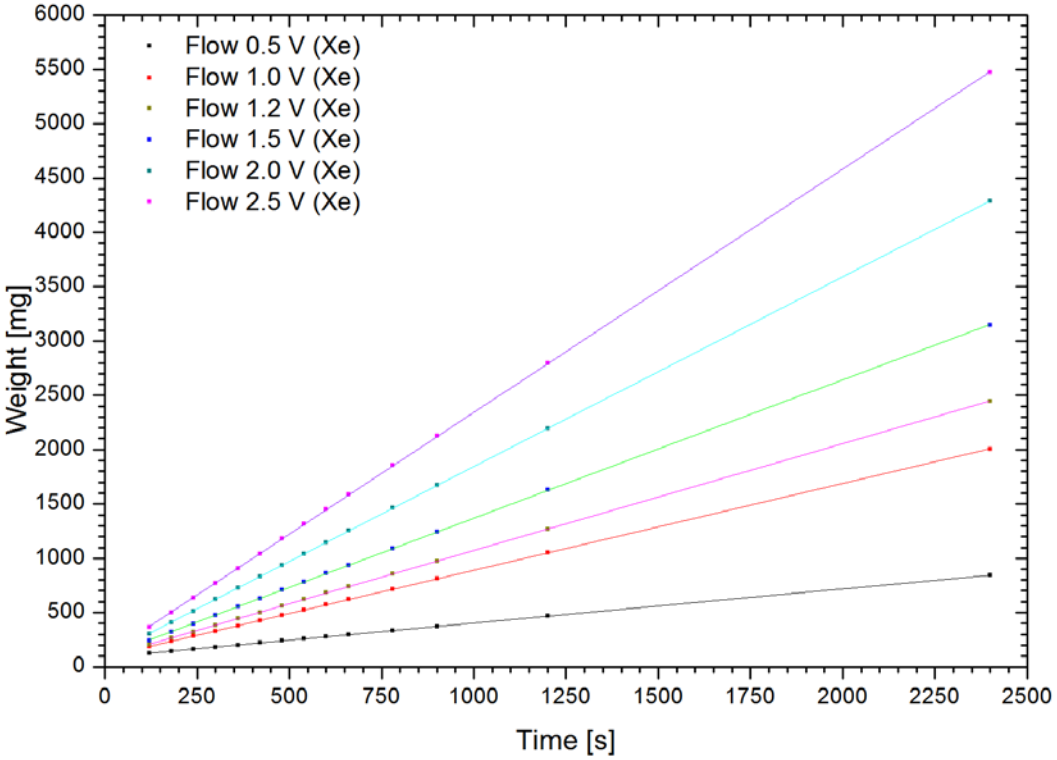

Figure 4-2: Calibration data for Xe, measured with gas balance (the error is in the range of only ~1 mg, it is not visible)

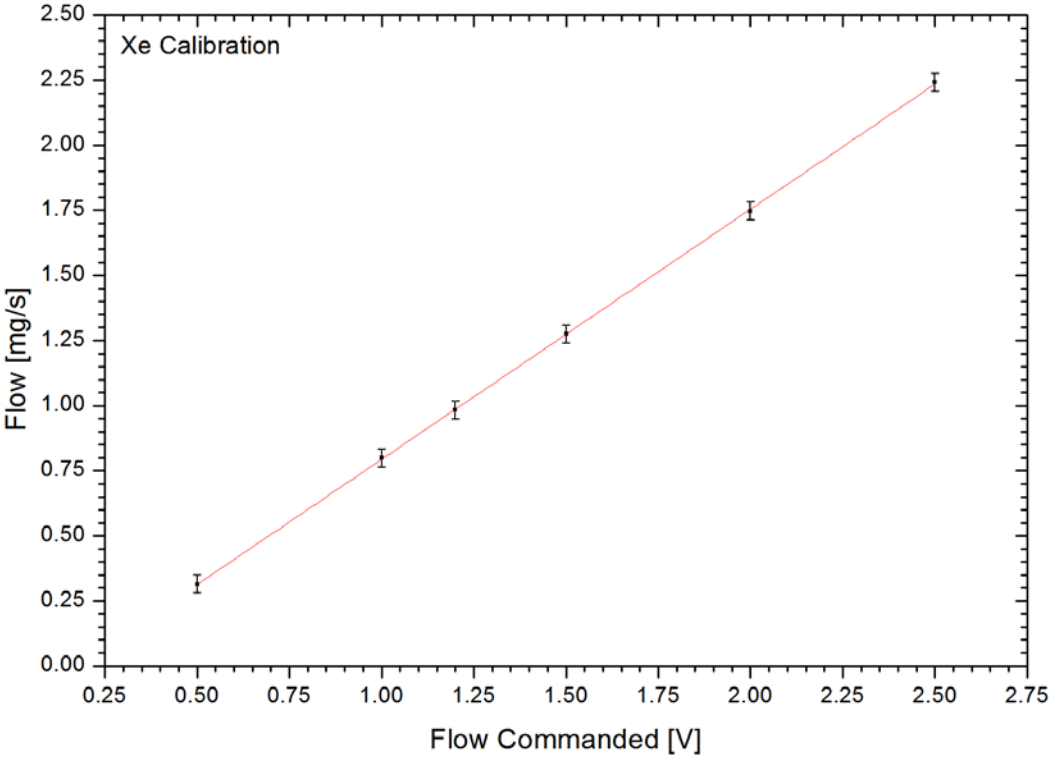

Figure 4-3: Calibration values for Xe with resulting conversion fit: Y=0.9601x - 0.165 [mg/s]

Time [s]	Flow 0.5 V [mg]	Flow 1.0 V [mg]	Flow 1.5 V [mg]	Flow 2.0 V [mg]	Flow 2.5 V [mg]
0	0	0	0	0	0
60	22	26	31	36	40
120	25	33	44	52	61
180	28	40	55	68	82
240	31	48	67	84	102
300	34	55	79	100	123
360	37	62	90	116	144
420	40	69	102	132	164
480	42	76	114	148	184
540	45	83	126	164	205
600	48	90	138	180	226
660	51	97	149	196	246
780	57	112	173.5	228	286
900	63	128	195	260	326
1200	77	162	254	340	428
2400	135	306	484	658	832

Table 4-2: Calibration data for N_2

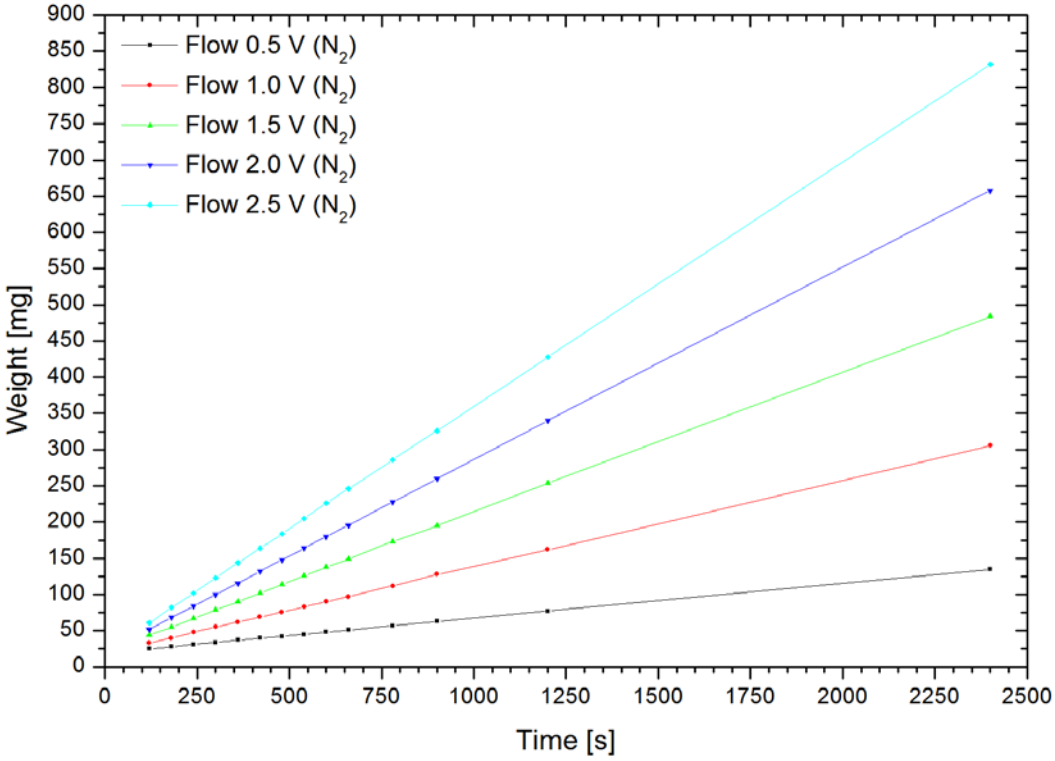

Figure 4-4: Calibration data for N_2, measured with gas balance

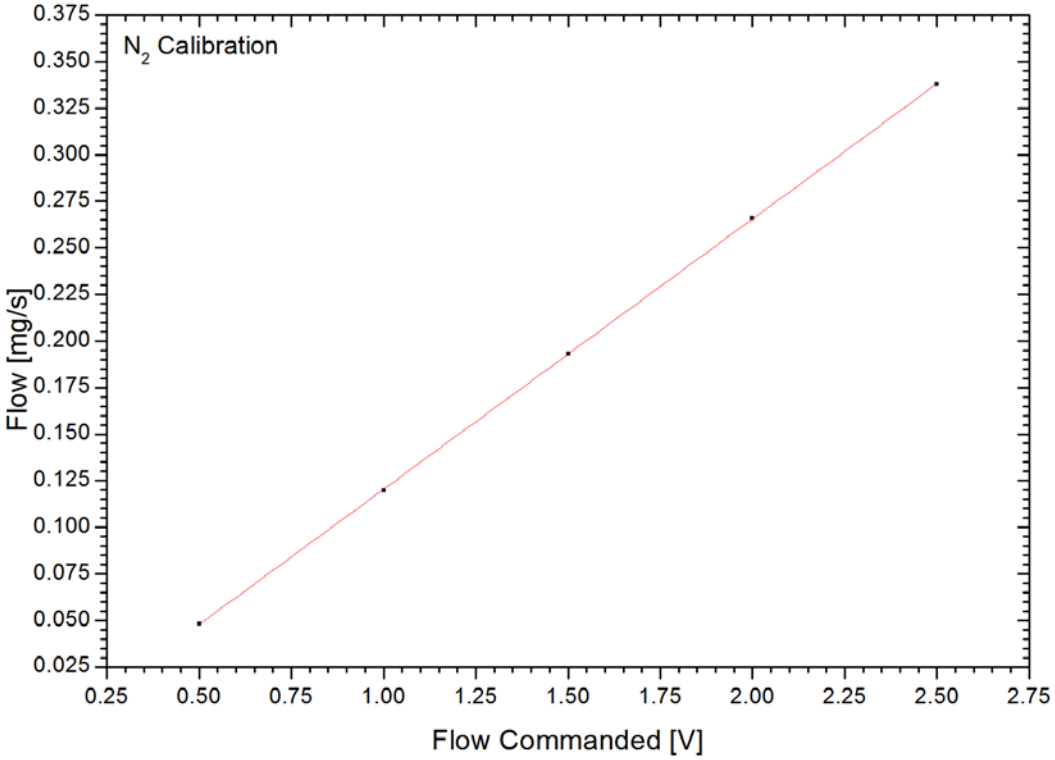

Figure 4-5: Calibration values for N_2 with resulting conversion fit: Y=0.1452x - 0.0247 [mg/s]

Time [s]	Flow 0.5 V [mg]	Flow 1.0 V [mg]	Flow 1.5 V [mg]	Flow 2.0 V [mg]	Flow 2.5 V [mg]
0	0	0	0	0	0
60	16	30	35	39	45
120	19	38	48	58	67
180	22	46	61	76	90
240	25	54	74	95	114
300	28	62	87	112	137
360	31	71	101	130	160
420	34	79	114	148	182
480	37	87	127	166	206
540	40	95	140	184	228
600	43	103	153	201	250
660	46	111	166	219	273
780	53	128	193	255	318
900	60	144	218	291	364
1200	76	186	285	381	479
2400	139	350	547	741	933

Table 4-3: Calibration data for O_2

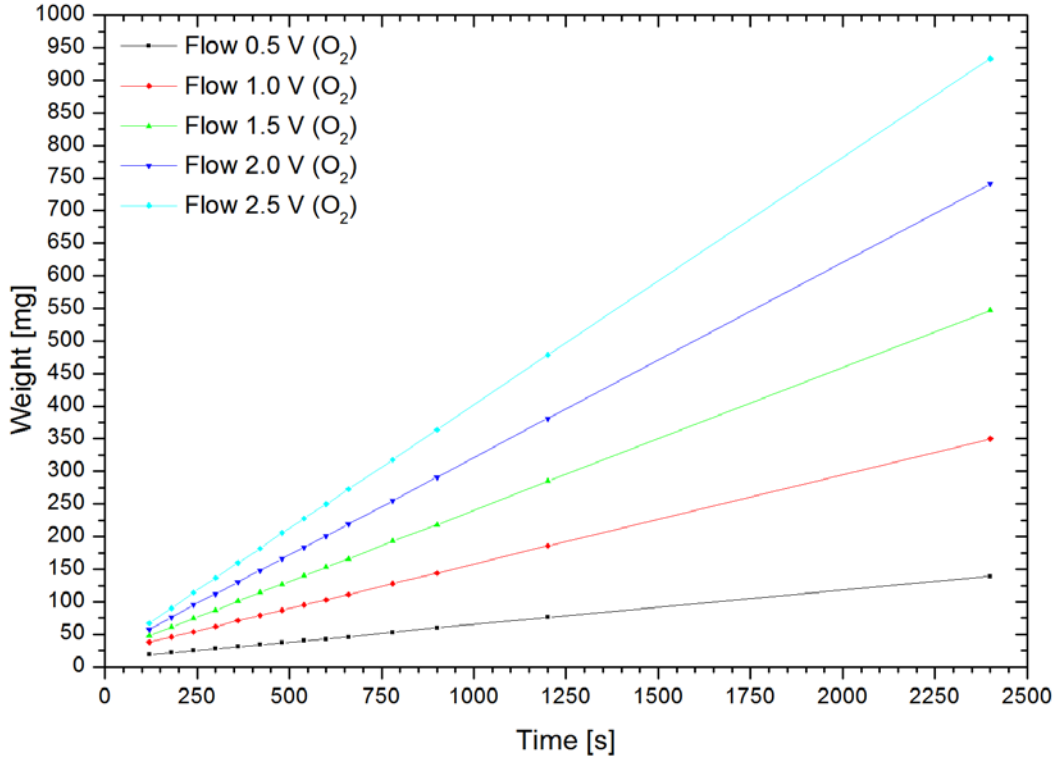

Figure 4-6: Calibration data for O_2, measured with gas balance

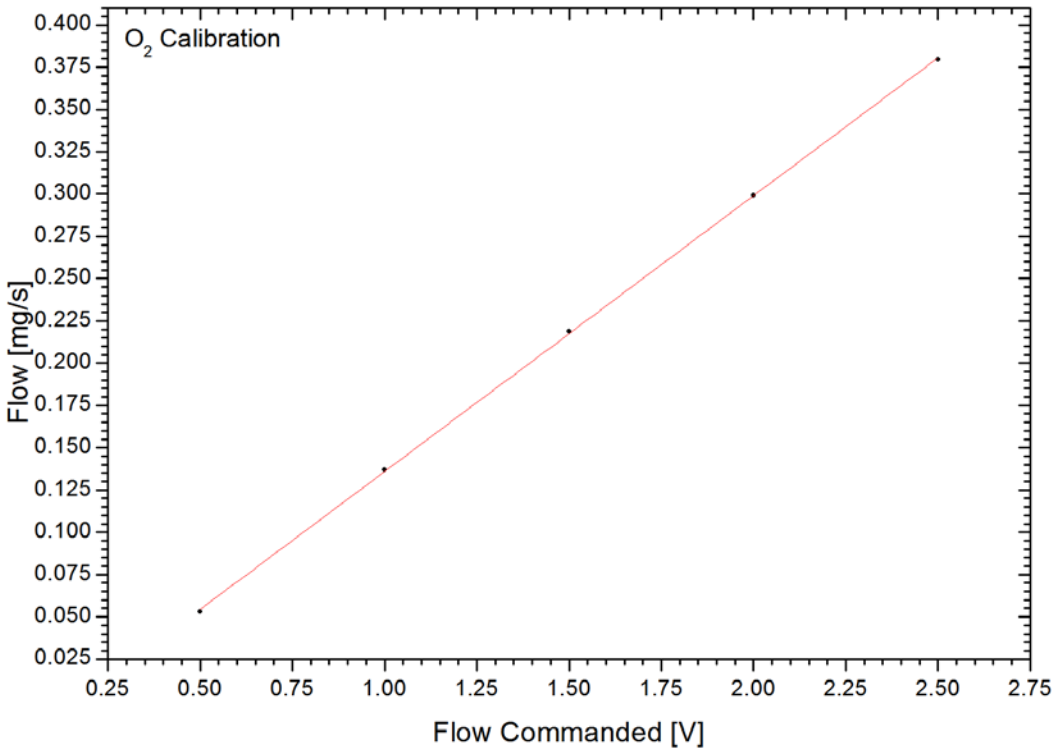

Figure 4-7: Calibration values for O_2 with conversion fit : Y=0.1631x – 0.02713 [mg/s]

Finally the fitted data provide the conversion formula for Xenon, Nitrogen and Oxygen. They are provided in Table 3-1 (below). For the conversion from [mg/s] to [SCCM] the following equations were used:

$$1\,SCCM = \frac{6.022 \cdot 10^{23}}{\left(22.4\left[\frac{L}{mol}\right] \cdot 10^{3}\left[\frac{cc}{l}\right] \cdot 60\left[\frac{s}{min}\right] \cdot \left(\frac{293.15K}{273.15K}\right)\right)} = 4.17246 \cdot 10^{17}[\text{Atoms/s}]$$

$$Xe\text{: } 1\,SCCM = 4.1725 \cdot 10^{17} \cdot 1.660539 \cdot 10^{-27} \cdot m_{Xe} \cdot 10^{6} \cdot CC = 9.16633318 \cdot 10^{-2}[\frac{mg}{s}]$$

$$N_2\text{: } 1\,SCCM = 4.1725 \cdot 10^{17} \cdot 1.660539 \cdot 10^{-27} \cdot m_{N_2} \cdot 10^{6} \cdot CC = 1.94149802 \cdot 10^{-2}[\frac{mg}{s}]$$

$$O_2\text{: } 1\,SCCM = 4.1725 \cdot 10^{17} \cdot 1.660539 \cdot 10^{-27} \cdot m_{O_2} \cdot 10^{6} \cdot CC = 2.21837606 \cdot 10^{-2}[\frac{mg}{s}]$$

Propellant	Mass flow [mg/s]	Mass flow [SCCM]
Xe	$Y = 0.9601 * X - 0.16500$	$Y = \frac{(0.9601 * X - 0.16500)}{9.16633318 \cdot 10^{-2}}$
N_2	$Y = 0.1452 * X - 0.02470$	$Y = \frac{(0.1452 * X - 0.02470)}{1.94149802 \cdot 10^{-2}}$
O_2	$Y = 0.1631 * X - 0.02713$	$Y = \frac{(0.1631 * X - 0.02713)}{2.21837606 \cdot 10^{-2}}$

Table 4-4: Conversion equations for Xe, N_2 and O_2

These conversion equations were used to calculate the required command voltages of the EADS MFCs and to convert the measured flow values to SCCM and mg/s. The values and the correctness of these equations were also verified. The maximum errors calculated for these measurements are shown in Table 4-5.

Propellant	Δ Mass flow [mg/s]	Δ Mass flow [SCCM]
Xe	0.035	3 %
Nitrogen	0.004	3 %
Oxygen	0.007	3 %

Table 4-5: Calculated maximum errors for the gas flow calibration performed with the Mettler Toledo gas balance

The Bronkhorst MFCs have been newly calibrated and are directly command-able without using a special calculated conversion factor.

4.2. Cold-flow test with EADS flow board

The following mass flow stepping was done to validate the pumping capability for Xenon, Nitrogen and Oxygen of the Jumbo test facility. Additionally it is also the cold flow test. According to our calibration problems we commanded different voltages to the MFC and measured the behavior of the chamber pressure at the center and at the door. The correlation of the commanded voltages and the resulting mass flow was separately measured and calculated for Xenon, Nitrogen and Oxygen. The used procedures are described in the next chapter. The cold flow measurement consists of two parts. The up and the down stepping is measured sequentially and drawn in two graphs. Figure 4-8 and Figure 4-9 show the linear dependency of the commanded flow rates (converted to SCCM) to the chamber pressure. It could be recognized, that the door pressure is a little higher than the

pressure in the center of the chamber. This is caused by vaporizing water, which is located in the graphite shielded beam dump mounted on the door.

4.2.1. Cold-flow test with Nitrogen

1	Increase propellant mass flow from 0 to 4 V in the following steps: 0.0, 0.5, 1.0, 1.5, 2.0, 2.5, 3.0, 3.5 and 4.0 V. Hold each mass flow level for 3 minutes, then measure the pressures of the chamber.
2	Decrease propellant mass flow from 4 to 0 V in the following steps: 4.0, 3.5, 3.0, 2.5, 2.0, 1.5, 1.0, 0.5 and 0.0 V. Hold each mass flow level for 3 minutes, then measure the pressures of the chamber.

Table 4-6: Cold-flow and pumping capability test for N_2

Mass-flow [V]	Mass-flow [SCCM]	Mass-flow [mg/s]
0.50	2.47	0.0479
1.00	6.21	0.1205
1.50	9.95	0.1931
2.00	13.69	0.2657
2.50	17.42	0.3383
3.00	21.16	0.4109
3.50	24.90	0.4835
4.00	28.64	0.5561

Table 4-7: Conversion table N_2

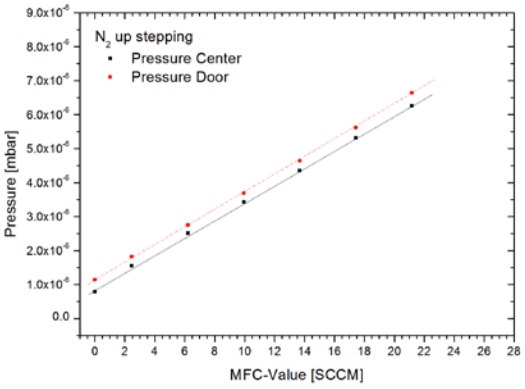

Figure 4-8: Cold-flow test for N_2, up stepping (0.5 V steps)

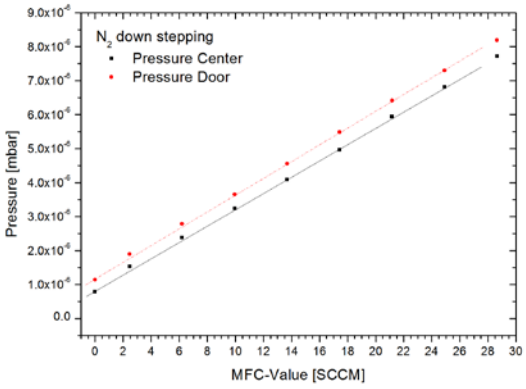

Figure 4-9: Cold-flow test for N_2, down stepping (0.5 V steps)

4.2.2. Cold-flow test with Oxygen

1	Increase propellant mass flow from 0-18.55 SCCM as described in Table 4-9. Hold each mass flow level for 3 minutes and measure the pressures of the chamber.
2	Decrease propellant mass flow from 18.55-0 SCCM as described in Table 4-9. Hold each mass flow level for 3 minutes and measure the pressures of the chamber.

Table 4-8: Cold-flow and pumping capability test for O_2

Conversions values from applied voltage to flow rate are reported on the following table (as resulting from calibration).

O_2 [SCCM]	MFC command [V]	O_2 [mg/s]
0.00	0.166	0.000
0.58	0.245	0.013
1.16	0.324	0.026
1.74	0.403	0.039
2.32	0.482	0.051
2.89	0.560	0.064
3.48	0.639	0.077
4.06	0.718	0.090
4.64	0.797	0.103
5.22	0.876	0.116
5.80	0.955	0.129
6.37	1.033	0.141
6.95	1.112	0.154
7.53	1.191	0.167
8.11	1.270	0.180
8.70	1.349	0.193
9.28	1.428	0.206
9.85	1.506	0.219
10.43	1.585	0.231
11.01	1.664	0.244
11.59	1.743	0.257
12.17	1.822	0.270
12.75	1.900	0.283
13.33	1.979	0.296
13.91	2.058	0.309
14.49	2.137	0.321
15.07	2.216	0.334
15.65	2.295	0.347
16.22	2.373	0.360
16.80	2.452	0.373
17.39	2.531	0.386
17.97	2.610	0.399
18.55	2.689	0.411

Table 4-9: Conversion table O_2

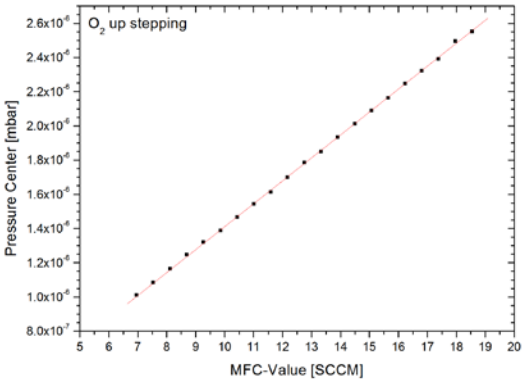

Figure 4-10: Cold-flow test for O_2, up stepping (0.5 V steps)

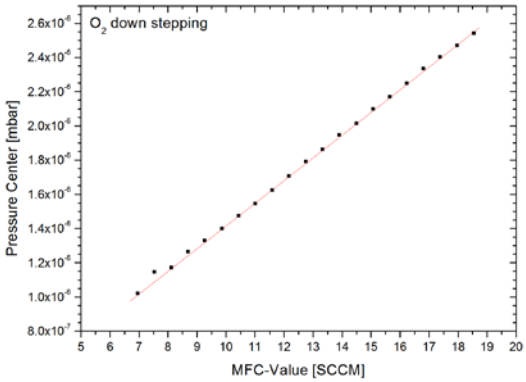

Figure 4-11: Cold-flow test for O_2, down stepping (0.5 V steps)

4.3. Cold-flow test with new gas mixture flow board

This test is performed to verify the pumping capacity of the facility when testing with Oxygen, Nitrogen, Xenon, N_2+O_2 and N_2+O_2+Xe. The thruster is not ignited or operated during these test, only the mass flow is varied.

Different mass flows were commanded to the MFCs and the chamber pressure was measured at the center and at the door. The cold flow measurement consists again of two parts. The up and the down stepping is measured sequentially and drawn in two graphs. This procedure is described in Table 4-10. Figure 4-12 to Figure 4-21 show the linear dependency of the commanded flow rates (converted to SCCM) to the chamber pressure. It could be recognized, that the door pressure is a little higher than the center. This is caused by vaporizing water, which is located in the graphite shielded beam dump.

1	Increase propellant mass flow from 0 to 18 SCCM in 1 SCCM steps (0.5 for Xenon). Hold each mass flow level for 3 minutes (until stabilization of the backpressure in the facility) and measure the pressures of the chamber.
2	Decrease propellant mass flow from 18 to 0 SCCM in 1 SCCM steps (0.5 for Xenon). Hold each mass flow level for 3 minutes (until stabilization of the backpressure in the facility) and measure the pressures of the chamber.

Table 4-10: Cold-flow and pumping capability test

4.3.1. Cold-flow test with Xe

Gas	MFC-setpoint [SCCM]	Inlet pressure [mbar]	Pressure center [mbar]	Pressure door [mbar]
Xe	0	4.44E-02		6.900E-07
Xe	0	2.11E-01		6.834E-07
Xe	0.5	5.05E-01		7.180E-07
Xe	1	7.97E-1		9.095E-07
Xe	1.5	9.40E-01		1.195E-06
Xe	2	1.03E+00	1.227E-06	1.409E-06
Xe	2.5	1.10E+00	1.544E-06	1.700E-06
Xe	3	1.15E+00	1.898E-06	2.010E-06
Xe	3.5	1.20E+00	2.336E-06	2.380E-06

Xe	4	1.23E+00	2.584E-06	2.610E-06
Xe	4.5	1.27E+00	2.966E-06	2.928E-06
Xe	5	1.30E+00	3.239E-06	3.220E-06
Xe	5.5	1.32E+00	3.600E-06	3.548E-06
Xe	6	1.34E+00	4.009E-06	3.906E-06
Xe	6.5	1.36E+00	4.296E-06	4.183E-06
Xe	7	1.38E+00	4.701E-06	4.555E-06
Xe	7.5	1.40E+00	4.927E-06	4.756E-06
Xe	8	1.41E+00	5.169E-06	4.966E-06
Xe	8.5	1.43E+00	5.442E-06	5.254E-06
Xe	9	1.44E+00	5.761E-06	5.539E-06
Xe	9.5	1.45E+00	6.099E-06	5.840E-06
Xe	10	1.46E+00	6.447E-06	6.135E-06
Xe	10.5	1.47E+00	6.810E-06	6.474E-06
Xe	11	1.48E+00	6.964E-06	6.375E-06
Xe	11.5	1.49E+00	7.298E-06	6.672E-06
Xe	12	1.50E+00	7.600E-06	6.950E-06
Xe	12.5	1.51E+00	7.912E-06	7.205E-06
Xe	13	1.52E+00	8.328E-06	7.514E-06
Xe	13.5	1.53E+00	8.609E-06	7.790E-06
Xe	14	1.54E+00	8.912E-06	8.114E-06
Xe	14.5	1.55E+00	9.293E-06	8.422E-06
Xe	15	1.56E+00	9.551E-06	8.668E-06
Xe	15.5	1.57E+00	9.802E-06	8.890E-06
Xe	16	1.57E+00	1.114E-05	9.249E-06
Xe	16.5	1.57E+00	1.041E-05	9.542E-06
Xe	17	1.58E+00	1.071E-05	9.845E-06
Xe	17.5	1.59E+00	1.102E-05	1.013E-05
Xe	18	1.60E+00	1.129E-05	1.051E-05
Xe	18	1.59E+00	1.129E-05	1.052E-05
Xe	17.5	1.58E+00	1.103E-05	1.030E-05
Xe	17	1.58E+00	1.071E-05	9.833E-06
Xe	16.5	1.57E+00	1.041E-05	9.565E-06
Xe	16	1.56E+00	1.031E-05	9.260E-06
Xe	15.5	1.56E+00	9.809E-06	8.943E-06
Xe	15	1.56E+00	9.558E-06	8.679E-06
Xe	14.5	1.55E+00	9.239E-06	8.402E-06
Xe	14	1.54E+00	8.919E-06	8.027E-06
Xe	13.5	1.53E+00	8.665E-06	7.725E-06
Xe	13	1.52E+00	8.274E-06	7.434E-06
Xe	12.5	1.51E+00	7.912E-06	7.154E-06
Xe	12	1.50E+00	7.621E-06	6.900E-06
Xe	11.5	1.49E+00	7.241E-06	6.624E-06
Xe	11	1.48E+00	6.964E-06	6.314E-06
Xe	10.5	1.47E+00	6.646E-06	6.069E-06
Xe	10	1.46E+00	6.318E-06	5.777E-06
Xe	9.5	1.45E+00	6.060E-06	5.506E-06
Xe	9	1.44E+00	5.663E-06	5.204E-06
Xe	8.5	1.42E+00	5.357E-06	4.913E-06
Xe	8	1.41E+00	5.053E-06	4.632E-06
Xe	7.5	1.39E+00	4.736E-06	4.346E-06
Xe	7	1.37E+00	4.419E-06	4.064E-06
Xe	6.5	1.35E+00	4.076E-06	3.754E-06
Xe	6	1.33E+00	3.735E-06	3.460E-06
Xe	5.5	1.31E+00	3.406E-06	3.189E-06

Xe	5	1.29E+00	3.086E-06	2.896E-06
Xe	4.5	1.25E+02	2.754E-06	2.635E-06
Xe	4	1.22E+00	2.438E-06	2.362E-06
Xe	3.5	1.18E+00	2.104E-06	2.097E-06
Xe	3	1.13E+00	1.799E-06	1.863E-06
Xe	2.5	1.08E+00	1.458E-06	1.620E-06
Xe	2	1.01E+00	1.128E-06	1.376E-06
Xe	1.5	9.15E-01		1.143E-06
Xe	1	7.60E-01		9.040E-07
Xe	0.5	4.00E-01		6.712E-07
Xe	0	2.02E-01		6.231E-07
Xe	0	1.40E-01		6.201E-07

Table 4-11: Cold flow and pumping capability test for Xenon

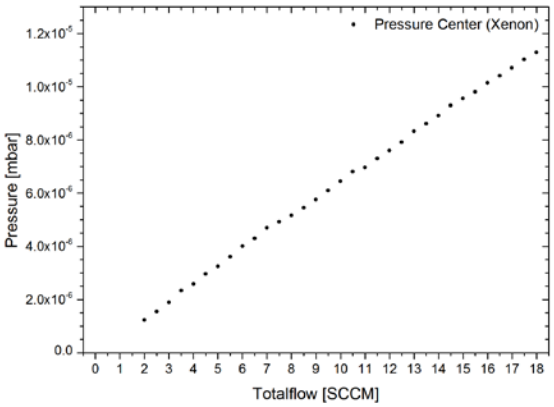

Figure 4-12: Cold-flow test for Xe, up stepping (0.5 SCCM steps)

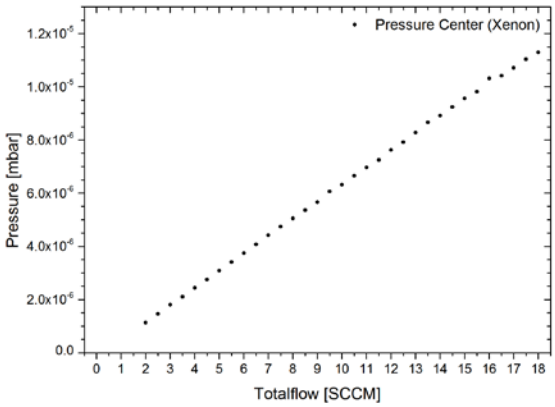

Figure 4-13: Cold-flow test for Xe, down stepping (0.5 SCCM steps)

4.3.2. Cold-flow test with Nitrogen

Gas	MFC-setpoint	Inlet pressure	Pressure center	Pressure door
	[SCCM]	[mbar]	[mbar]	[mbar]
N_2	0	4.63E-02		5.388E-07
N_2	0	2.58E-01		5.299E-07
N_2	1	3.30E+00		7.009E-07
N_2	2	4.64E+00		8.894E-07
N_2	3	5.70E+00		1.073E-06
N_2	4	6.65E+00		1.258E-06
N_2	5	7.50E+00		1.456E-06
N_2	6	8.28E+00	1.170E-06	1.662E-06
N_2	7	9.02E+00	1.374E-06	1.840E-06
N_2	8	9.74E+00	1.487E-06	2.018E-06
N_2	9	1.03E+01	1.691E-06	2.214E-06
N_2	10	1.10E+01	1.826E-06	2.413E-06
N_2	11	1.16E+01	2.000E-06	2.569E-06
N_2	12	1.21E+01	2.152E-06	2.741E-06
N_2	13	1.27E+01	2.343E-06	2.896E-06
N_2	14	1.32E+01	2.511E-06	3.117E-06
N_2	15	1.37E+01	2.629E-06	3.262E-06
N_2	16	1.43E+01	2.783E-06	3.410E-06
N_2	17	1.47E+01	2.946E-06	3.591E-06
N_2	18	1.52E+01	3.092E-06	3.750E-06
N_2	18	1.52E+01	3.066E-06	3.727E-06

N_2	17	1.47E+01	2.926E-06	3.510E-06
N_2	16	1.43E+01	2.783E-06	3.317E-06
N_2	15	1.37E+01	2.633E-06	3.098E-06
N_2	14	1.32E+01	2.524E-06	2.900E-06
N_2	13	1.27E+01	2.343E-06	2.735E-06
N_2	12	1.21E+01	2.203E-06	2.542E-06
N_2	11	1.16E+01	2.021E-06	2.382E-06
N_2	10	1.10E+01	1.851E-06	2.197E-06
N_2	9	1.03E+01	1.717E-06	2.028E-06
N_2	8	9.75E+00	1.522E-06	1.876E-06
N_2	7	9.04E+00	1.393E-06	1.697E-06
N_2	6	8.30E+00	1.227E-06	1.539E-06
N_2	5	7.50E+00	1.045E-06	1.359E-06
N_2	4	6.66E+00		1.191E-06
N_2	3	5.71E+00		1.026E-06
N_2	2	4.64E+00		8.721E-07
N_2	1	3.29E+00		6.925E-07
N_2	0	3.53E-01		5.037E-07
N_2	0	2.03E-01		5.248E-07

Table 4-12: Cold-flow and pumping capability test with Nitrogen

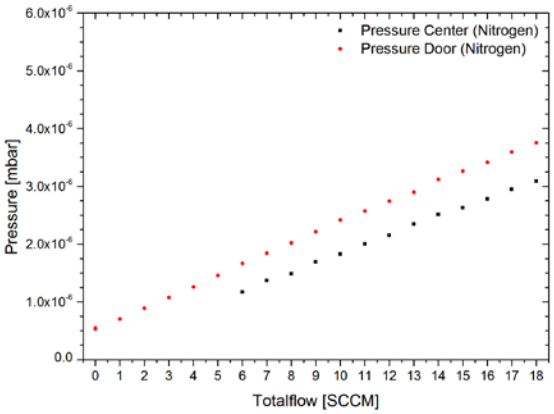

Figure 4-14: Cold-flow test for N_2, up stepping (1 SCCM steps)

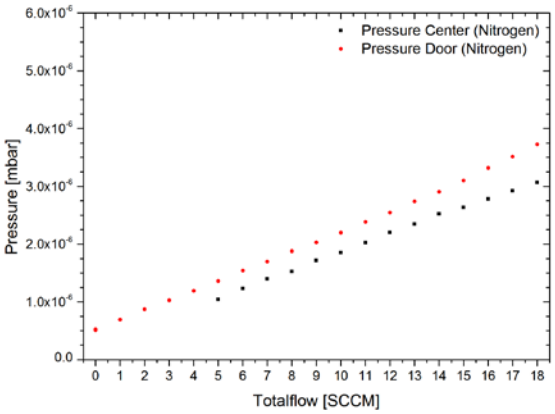

Figure 4-15: Cold-flow test for N_2, down stepping (1 SCCM steps)

4.3.3. Cold-flow test with Oxygen

Gas	MFC-setpoint	Inlet pressure	Pressure center	Pressure door
	[SCCM]	[mbar]	[mbar]	[mbar]
O_2	0	5.80E-01		5.105E-07
O_2	0	2.36E-01		5.075E-07
O_2	1	3.52E+00		6.793E-07
O_2	2	5.13E+00		7.931E-07
O_2	3	6.36E+00		9.249E-07
O_2	4	7.28E+00		1.032E-06
O_2	5	8.20E+00		1.136E-06
O_2	6	9.07E+00		1.257E-06
O_2	7	9.90E+00	1.007E-06	1.368E-06
O_2	8	1.07E+01	1.137E-06	1.481E-06
O_2	9	1.14E+01	1.235E-06	1.584E-06
O_2	10	1.22E+01	1.397E-06	1.712E-06
O_2	11	1.29E+01	1.476E-06	1.823E-06
O_2	12	1.35E+01	1.585E-06	1.945E-06
O_2	13	1.42E+01	1.713E-06	2.067E-06

O_2	14	1.48E+01	1.832E-06	2.176E-06
O_2	15	1.54E+01	1.958E-06	2.303E-06
O_2	16	1.60E+01	2.098E-06	2.443E-06
O_2	15	1.66E+01	2.213E-06	2.563E-06
O_2	16	1.72E+01	2.302E-06	2.689E-06
O_2	18	1.72E+01	2.306E-06	2.692E-06
O_2	17	1.66E+01	2.200E-06	2.587E-06
O_2	16	1.60E+01	2.076E-06	2.466E-06
O_2	15	1.54E+01	1.961E-06	2.348E-06
O_2	14	1.48E+01	1.856E-06	2.233E-06
O_2	13	1.42E+01	1.718E-06	2.097E-06
O_2	12	1.35E+01	1.593E-06	1.982E-06
O_2	11	1.29E+01	1.497E-06	1.865E-06
O_2	10	1.22E+01	1.358E-06	1.744E-06
O_2	9	1.15E+01	1.236E-06	1.628E-06
O_2	8	1.07E+01	1.140E-06	1.507E-06
O_2	7	9.94E+00	1.004E-06	1.386E-06
O_2	6	9.07E+00		1.260E-06
O_2	5	8.20E+00		1.140E-06
O_2	4	7.22E+00		1.012E-06
O_2	3	6.15E+00		8.784E-07
O_2	2	4.92E+00		7.532E-07
O_2	1	3.38E+00		6.231E-07
O_2	0	2.76E-01		4.877E-07
O_2	0	2.16E-01		4.866E-07

Table 4-13: Cold-flow and pumping capability test with Oxygen

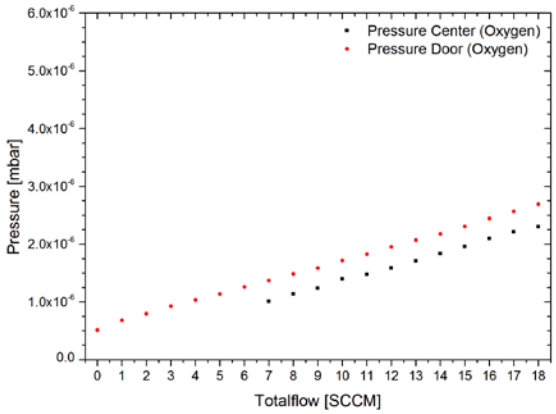

Figure 4-16: Cold-flow test for O_2, up stepping (1 SCCM steps)

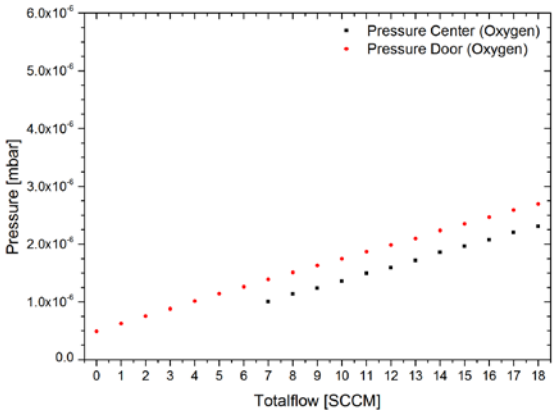

Figure 4-17: Cold-flow test for O_2, down stepping (1 SCCM steps)

4.3.4. Cold-flow test with N_2 + O_2

The gas distribution used for this test was directly mixed with the new flow panel. The gas composition was $1.27 \cdot N_2 \ + \ 1.00 \cdot O_2$.

Gas	MFC-setpoint	Inlet pressure	Pressure center	Pressure door
	[SCCM]	[mbar]	[mbar]	[mbar]
$N_2 + O_2$	0	3.47E-01		5.25E-07
$N_2 + O_2$	0	3.28E-01		4.98E-07
$N_2 + O_2$	1	3.73E+00		7.19E-07
$N_2 + O_2$	2	5.12E+00		8.76E-07
$N_2 + O_2$	3	6.26E+00		1.05E-06

$N_2 + O_2$	4	7.14E+00		1.21E-06
$N_2 + O_2$	5	8.04E+00		1.37E-06
$N_2 + O_2$	6	8.79E+00	1.120E-06	1.52E-06
$N_2 + O_2$	7	9.55E+00	1.270E-06	1.68E-06
$N_2 + O_2$	8	1.03E+01	1.419E-06	1.83E-06
$N_2 + O_2$	9	1.09E+01	1.564E-06	1.99E-06
$N_2 + O_2$	10	1.17E+01	1.736E-06	2.15E-06
$N_2 + O_2$	11	1.23E+01	1.883E-06	2.31E-06
$N_2 + O_2$	12	1.29E+01	2.014E-06	2.47E-06
$N_2 + O_2$	13	1.35E+01	2.171E-06	2.61E-06
$N_2 + O_2$	14	1.41E+01	2.316E-06	2.78E-06
$N_2 + O_2$	15	1.47E+01	2.493E-06	2.93E-06
$N_2 + O_2$	16	1.52E+01	2.610E-06	3.12E-06
$N_2 + O_2$	17	1.57E+01	2.728E-06	3.26E-06
$N_2 + O_2$	18	1.62E+01	2.877E-06	3.41E-06
$N_2 + O_2$	18	1.62E+01	2.869E-06	3.40E-06
$N_2 + O_2$	17	1.57E+01	2.748E-06	3.26E-06
$N_2 + O_2$	16	1.52E+01	2.605E-06	3.09E-06
$N_2 + O_2$	15	1.47E+01	2.470E-06	2.91E-06
$N_2 + O_2$	14	1.41E+01	2.321E-06	2.74E-06
$N_2 + O_2$	13	1.35E+01	2.185E-06	2.58E-06
$N_2 + O_2$	12	1.29E+01	2.020E-06	2.42E-06
$N_2 + O_2$	11	1.23E+01	1.881E-06	2.26E-06
$N_2 + O_2$	10	1.17E+01	1.730E-06	2.11E-06
$N_2 + O_2$	9	1.09E+01	1.572E-06	1.95E-06
$N_2 + O_2$	8	1.03E+01	1.443E-06	1.79E-06
$N_2 + O_2$	7	9.55E+00	1.265E-06	1.63E-06
$N_2 + O_2$	6	8.79E+00	1.137E-06	1.48E-06
$N_2 + O_2$	5	7.98E+00		1.32E-06
$N_2 + O_2$	4	7.03E+00		1.16E-06
$N_2 + O_2$	3	6.11E+00		9.98E-07
$N_2 + O_2$	2	4.93E+00		8.38E-07
$N_2 + O_2$	1	3.55E+00		6.88E-07
$N_2 + O_2$	0	4.37E-01		4.77E-07
$N_2 + O_2$	0	2.60E-01		4.85E-07

Table 4-14: Cold-flow and pumping capability test with N_2+O_2 mixture

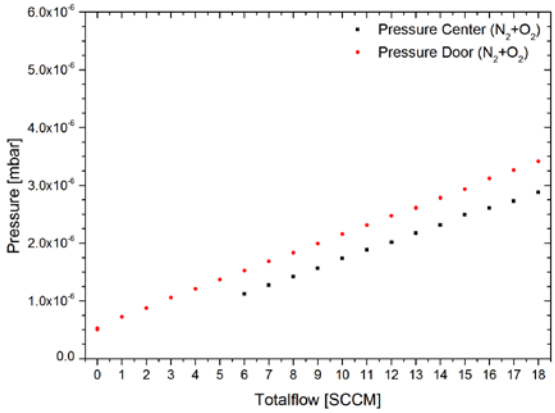

Figure 4-18: Cold-flow test for N_2+O_2, up stepping (1 SCCM steps)

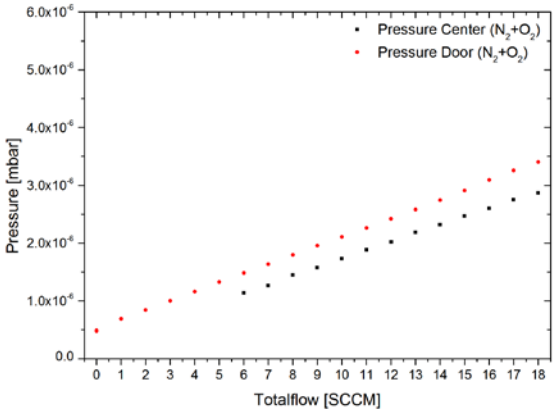

Figure 4-19: Cold-flow test for N_2+O_2, down stepping (1 SCCM steps)

4.3.5. Cold-flow test with N_2 + O_2 + Xe

The gas distribution used for this test was directly mixed with the new flow panel. The gas composition was $1.27 \cdot N_2 + 1.00 \cdot O_2 + 10\,\% Xe$. Due to the limitations of the hardware the mass flow rates < 5 SCCM could not be stable mixed easily, because the Xenon flow controller (0.5 - 50 SCCM) would have been operated beyond the lower linear limit. Therefore the mass flow rates from 0 to 4 SCCM were mixed without Xenon, at least during this test.

Gas	MFC-setpoint [SCCM]	Inlet pressure [mbar]	Pressure center [mbar]	Pressure door [mbar]
$N_2 + O_2$	0	3.74E-02		5.248E-07
$N_2 + O_2$	0	4.92E-01		5.185E-07
$N_2 + O_2$	1	3.44E+00		7.196E-07
$N_2 + O_2$	2	4.72E+00		8.879E-07
$N_2 + O_2$	3	5.76E+00		1.068E-06
$N_2 + O_2 + Xe$	4	6.44E+00		1.180E-06
$N_2 + O_2 + Xe$	5	7.33E+00	1.051E-06	1.357E-06
$N_2 + O_2 + Xe$	6	8.12E+00	1.295E-06	1.540E-06
$N_2 + O_2 + Xe$	7	8.82E+00	1.409E-06	1.696E-06
$N_2 + O_2 + Xe$	8	9.50E+00	1.579E-06	1.867E-06
$N_2 + O_2 + Xe$	9	1.02E+01	1.774E-06	2.048E-06
$N_2 + O_2 + Xe$	10	1.08E+01	1.997E-06	2.235E-06
$N_2 + O_2 + Xe$	11	1.14E+01	2.182E-06	2.419E-06
$N_2 + O_2 + Xe$	12	1.20E+01	2.404E-06	2.641E-06
$N_2 + O_2 + Xe$	13	1.26E+01	2.597E-06	2.818E-06
$N_2 + O_2 + Xe$	14	1.31E+01	2.787E-06	3.039E-06
$N_2 + O_2 + Xe$	15	1.36E+01	2.981E-06	3.251E-06
$N_2 + O_2 + Xe$	16	1.42E+01	3.178E-06	3.456E-06
$N_2 + O_2 + Xe$	17	1.46E+01	3.394E-06	3.687E-06
$N_2 + O_2 + Xe$	18	1.50E+01	3.593E-06	3.883E-06
$N_2 + O_2 + Xe$	18	1.50E+01	3.593E-06	3.892E-06
$N_2 + O_2 + Xe$	17	1.46E+01	3.406E-06	3.691E-06
$N_2 + O_2 + Xe$	16	1.41E+01	3.241E-06	3.510E-06
$N_2 + O_2 + Xe$	15	1.35E+01	3.007E-06	3.309E-06
$N_2 + O_2 + Xe$	14	1.30E+01	2.834E-06	3.136E-06
$N_2 + O_2 + Xe$	13	1.25E+01	2.629E-06	2.896E-06
$N_2 + O_2 + Xe$	12	1.20E+01	2.436E-06	2.692E-06
$N_2 + O_2 + Xe$	11	1.13E+01	2.244E-06	2.508E-06
$N_2 + O_2 + Xe$	10	1.08E+01	2.049E-06	2.303E-06
$N_2 + O_2 + Xe$	9	1.01E+01	1.819E-06	2.107E-06
$N_2 + O_2 + Xe$	8	9.45E+00	1.620E-06	1.919E-06
$N_2 + O_2 + Xe$	7	8.78E+00	1.425E-06	1.731E-06
$N_2 + O_2 + Xe$	6	8.05E+00	1.236E-06	1.541E-06
$N_2 + O_2 + Xe$	5	7.22E+00	1.061E-06	1.357E-06
$N_2 + O_2 + Xe$	4	6.30E+00		1.164E-06
$N_2 + O_2$	3	5.73E+00		1.054E-06
$N_2 + O_2$	2	4.71E+00		8.911E-07
$N_2 + O_2$	1	3.42E+00		7.214E-07
$N_2 + O_2$	0	5.54E-01		4.931E-07
$N_2 + O_2$	0	3.54E-01		4.819E-07

Table 4-15: Cold-flow and pumping capability test with N_2+O_2+Xe mixture

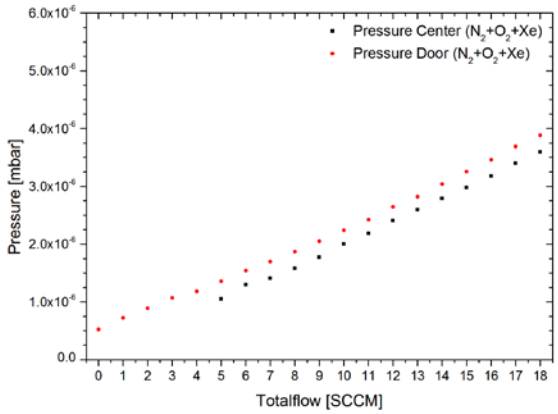

Figure 4-20: Cold-flow test for N_2+O_2+Xe, up stepping (1 SCCM steps)

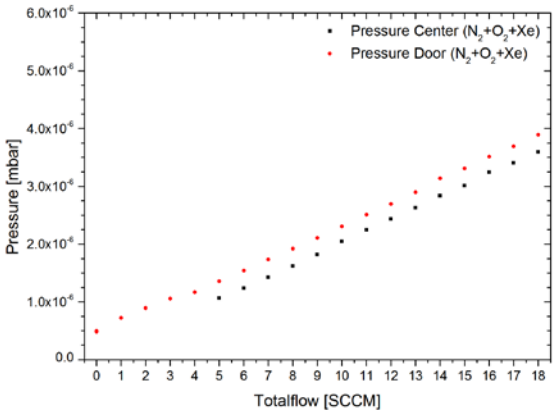

Figure 4-21: Cold-flow test for N_2+O_2+Xe, down stepping (1 SCCM steps)

The cold-flow tests were successfully performed and it was shown, that the pressure level of the vacuum facility fulfills the test pressure requirements for all tested propellants ($P < 5.0 \cdot 10^{-5}$ mbar, concerning the environmental conditions in the atmosphere). The functionality of the flow boards and the propellant feed system has also been demonstrated.

4.4. Ignition and functional test with Xenon

The RAM-EP-10 thruster was successfully ignited with Xenon and the ignition process with a pressure shock was validated. Due to the fact that a neutralizer was not present this method was chosen. The thruster operation with Xenon at different extraction levels was performed without any problems. First ignition tests with Nitrogen and Oxygen have also been performed, but were not successful, because the in coupled rf-power was too low during the ignition. Once the thruster was ignited with Xenon, the thruster could be operated after the propellant swapping with Nitrogen and Oxygen in defiance of this power limitation. As described later in this thesis the impedance and the rf-circuit have to be modified to lift up the power limit. But for the first test campaigns the thruster has to be untouched. The modification was implemented after the second test section in preparation for the gas mixture test (RIT-10-EBB → RAM-RIT-10).

4.5. Test campaign with Nitrogen

The performance mapping of a Radio Frequency Ion Thruster is done as described below:

For a specific I_{Beam}, (which in contact with a specific voltage defines a specific thrust) the RF-power and mass flow are dependent on each other. This dependency function is a characteristic of the thruster and the propellant. The performance mapping means the characterization of this dependency. Generally for a specific thrust, less power would be needed, the higher the gas flow is.

For the performance mapping, the I_{Beam} (thrust) should be kept constant and the gas flow should be changed. The needed rf-power should then be measured. For higher gas flows the rf-power consumption would be less and for lower gas flows the power consumption would

be higher. It should be emphasized, that this power is independent of the beam power ($= I_{PHV} \cdot U_{PHV} + I_{NHV} \cdot U_{NHV}$).

To keep the I_{Beam} (thrust) constant, a beam current controller or software can be used.

4.5.1. Performance mapping with Xenon

The performance mapping of the RIT-10-EBB, constructed for this activity, was to be cross checked with the performance values of the original RIT-10 thruster flown on Artemis and to generate a reference dataset for the comparison to the N_2 test. The operation point of the former RIT-10 is defined with a screen voltage of 1500 V, accel grid voltage of -600 V and a beam current of 234 mA (24). The characterization of the thruster's performance was, according the described procedure in 3.2.5.1, done by variation of the mass flow while the beam current was held constant. The thruster was operated with 5-7 different mass flow rates on each beam current level. For each point of operation the full set of parameters were recorded. Each single operational point had been operated until performance equilibrium was reached. Normally the performance equilibrium was reached after few minutes.

The thruster performance was characterized for the 5 levels of beam current:
75 mA, 100 mA, 150 mA, 200 mA and 234 mA.

To compare the RIT-10-EBB performance with Xenon and the nonconventional propellants, according to ESA recommendation we had to compare the thruster performance by the same maximum available power. The maximum available power for the RIT-10 on Artemis was 100 W of RF power and ($1500\,V \cdot 234\,mA =$) 351 W of beam power. i.e. the whole power for the thruster was 451 W. Based on this fact, the thruster performance should be done with the restriction on power consumption. In Table 4-16 the used parameters for this test are listed for every thrust and beam current level.

No	I_{Beam} [mA]	U_{PHV} [V]	U_{NHV} [V]	Max. RF-Power (Artemis) [W]	Thrust (calc.) [mN]	Mass flow [SCCM]	Operation Time [min]
1	75	1500	-600	338	4.82	1.5 - 13	> 15
2	100	1500	-600	299	6.43	1.5 - 13	> 15
3	150	1500	-600	226	9.65	3 - 12.5	> 15
4	200	1500	-600	151	12.86	3.5 - 11	> 15
5	234	1500	-600	100	15.05	3.5 - 9.5	> 15

Table 4-16: Settings for performance test with Xe

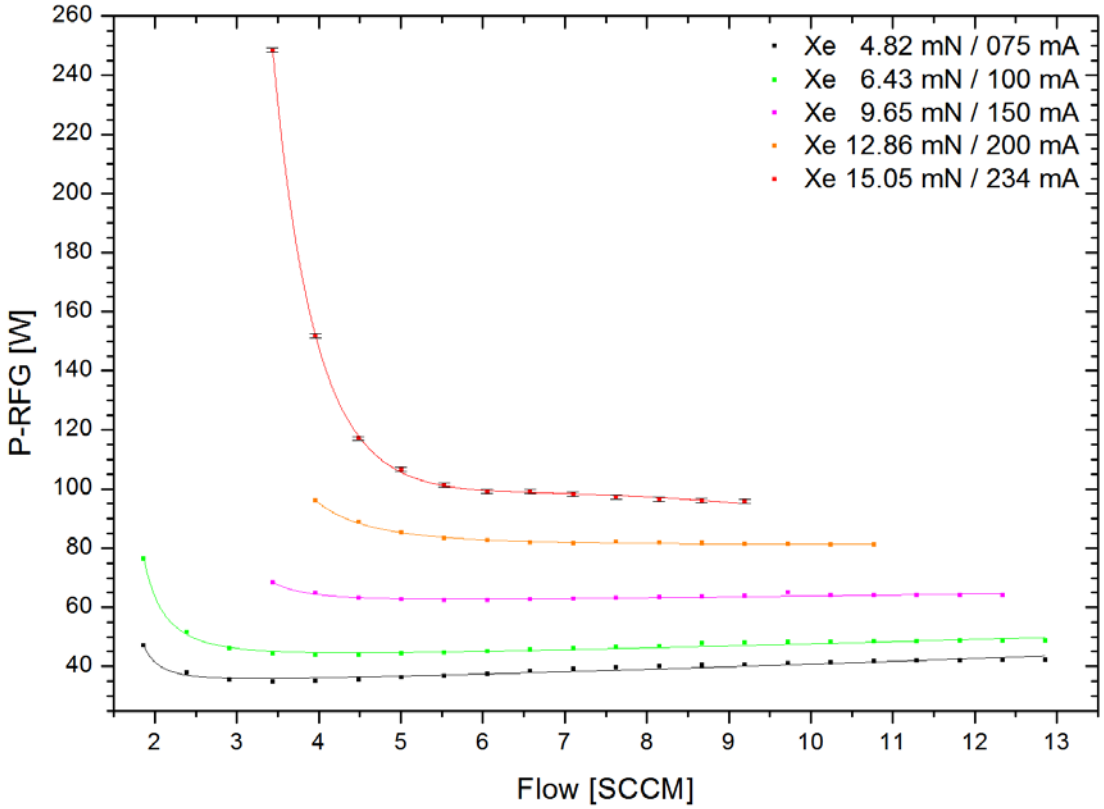

Figure 4-22: Performance overview for Xenon of the unmodified RAM-EP-10 thruster

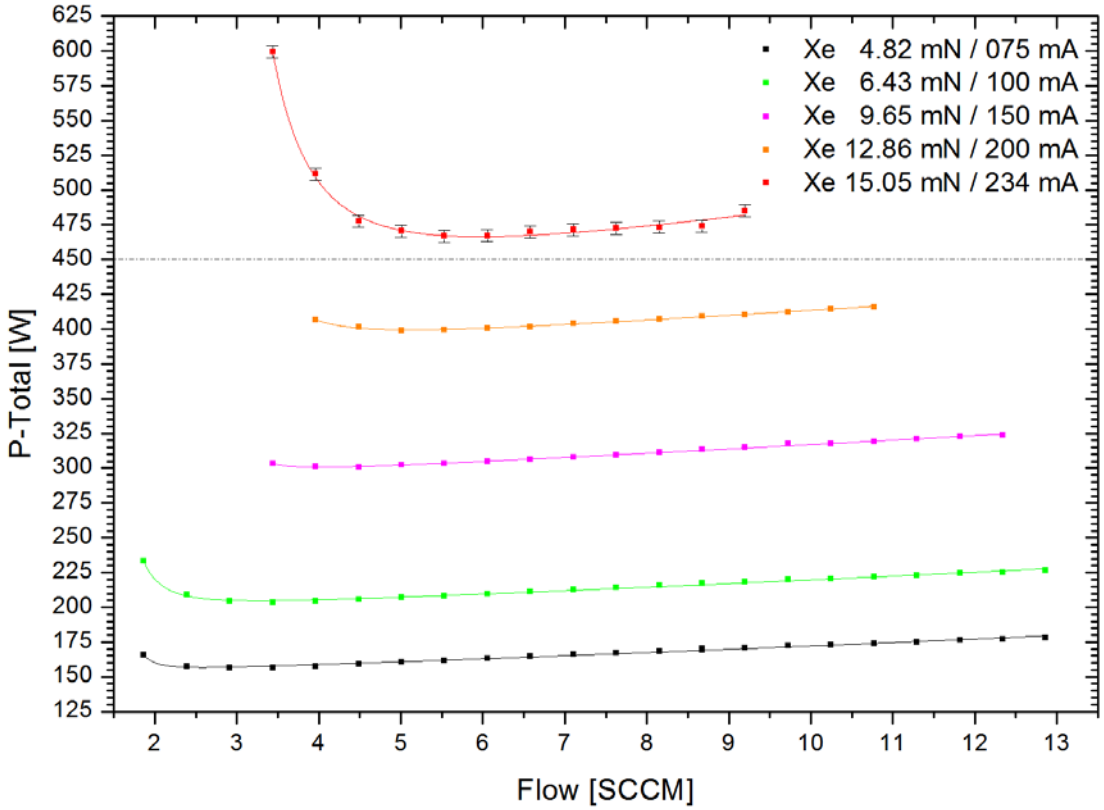

Figure 4-23: Performance overview for Xenon of the unmodified RAM-EP-10 thruster, P-Total

4.5.2. Performance mapping with Nitrogen

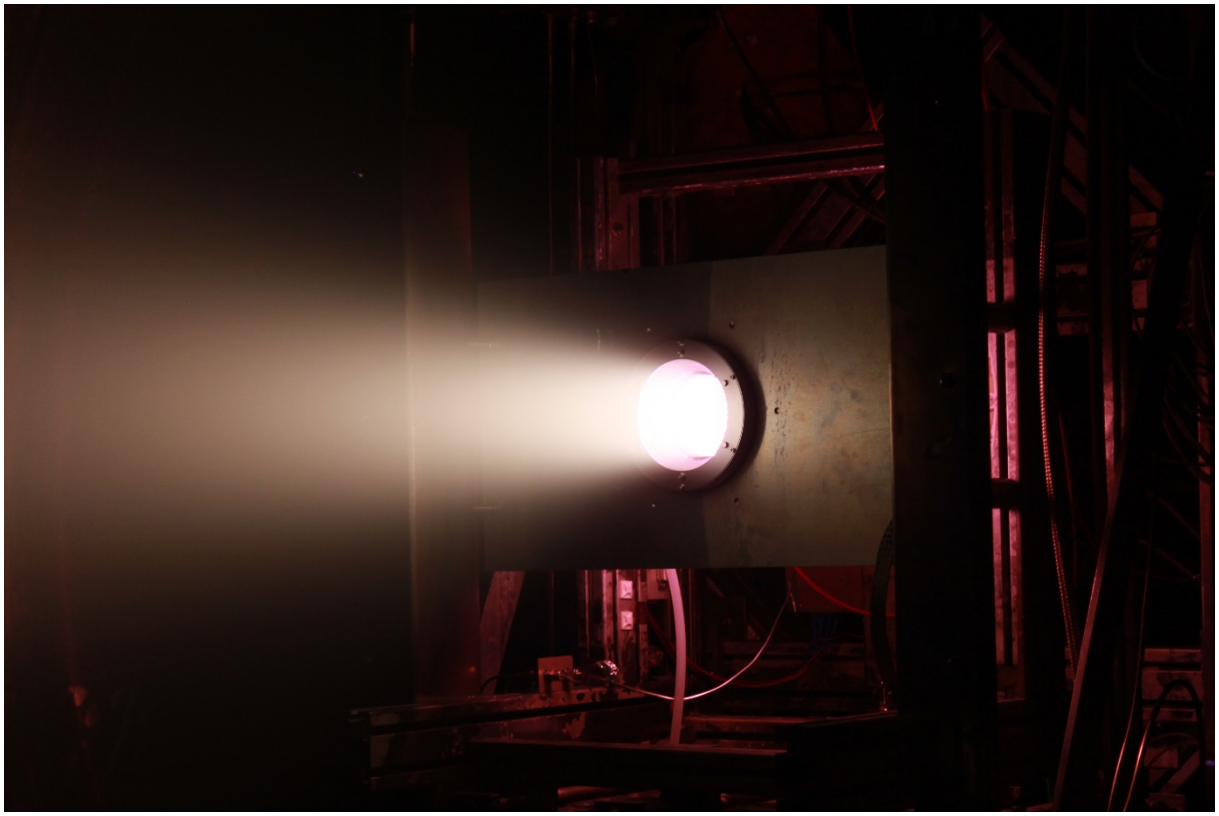

Figure 4-24: RAM-EP-10 thruster running with N_2

As described in 3.2.5.1 the thruster's performance was characterized by a variation of the mass flow whilst the beam current was kept constant. The thruster was operated with 15-20 different mass flow rates on each beam current level. For each point of operation the full set of parameters described above was recorded. It is proposed to characterize 5 levels of beam current. Each single operational point had been operated until performance equilibrium was reached. Normally the performance equilibrium was reached after few minutes whereas the full thermal equilibrium was reached after 3-4 hours.

The thruster performance was characterized for the 5 levels of beam current:
75 mA, 100 mA, 150 mA, 200 mA and 234 mA.

The effects of beam divergence and plasma potential are under the precision of the thrust measurement (about 3%).

No	I_{Beam} [mA]	U_{PHV} [V]	U_{NHV} [V]	Max. RF-Power (Artemis) [W]	Thrust (calc.) [mN]	Mass flow [SCCM]	Operation Time [min]
1	75	1500	-600	338	2.23	4 - 22	> 15
2	100	1500	-600	299	2.97	4.5 - 23	> 15
3	150	1500	-600	226	4.46	5.5 - 22	> 15
4	200	1500	-600	151	5.94	7 - 22	> 15
5	234	1500	-600	100	6.95	7.5 - 22	> 15

Table 4-17: Used parameters for performance mapping with N_2

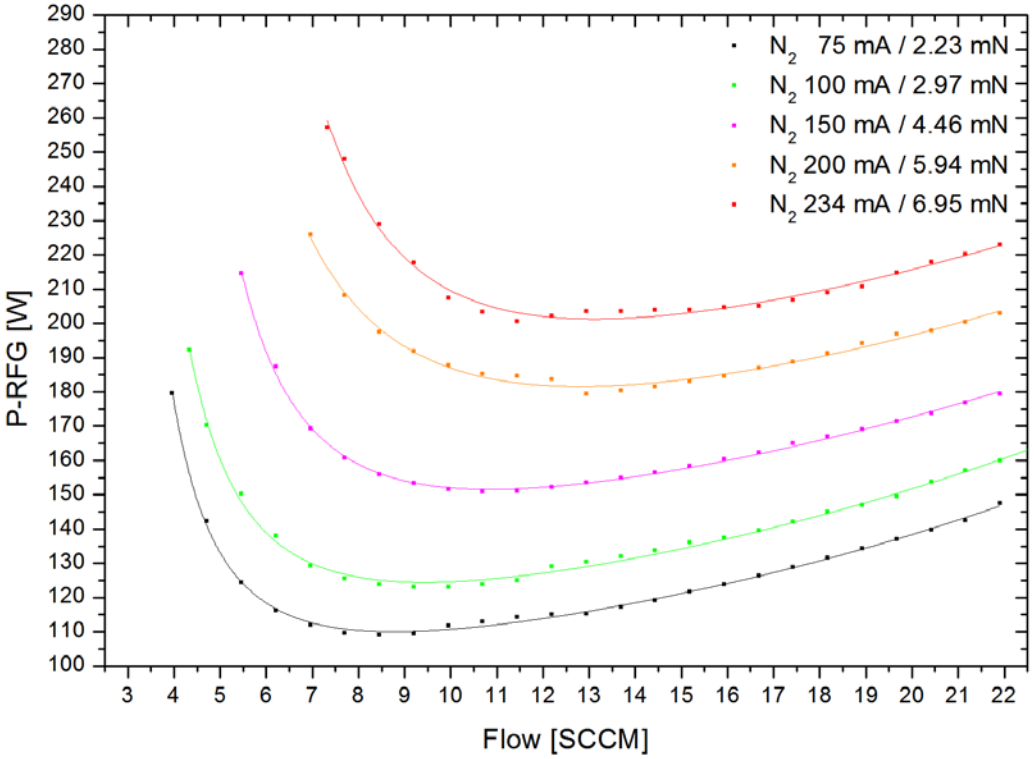

Figure 4-25: Performance overview for N_2

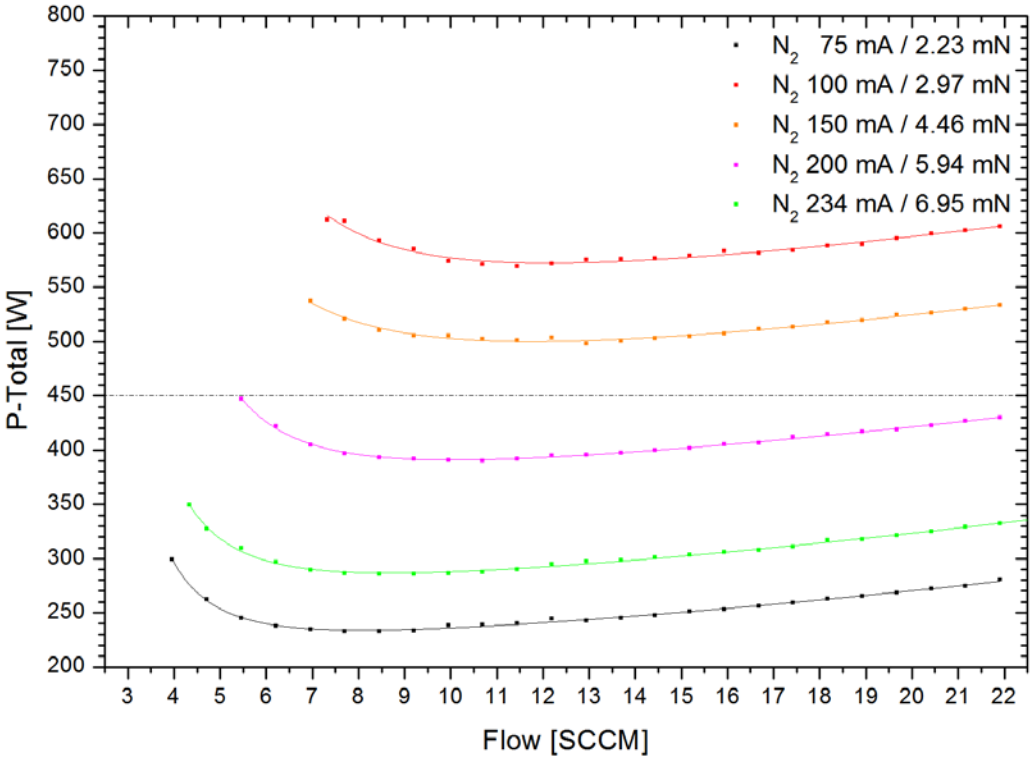

Figure 4-26: P-Total performance overview for N_2

The power demand for the RFG and the total power consumption of the thruster working with Nitrogen is shown in Figure 4-25 and Figure 4-26. Figure 4-28 shows the both measurements with other post processing. It covers the measurements on Xe and N_2

simultaneously. In this graph, the total needed power for different thrusts and different gas flows is shown. The horizontal line shows the maximum available power for the RIT thruster (Artemis). Obviously, the RIT-10-EBB thruster needs a higher amount of gas and total power, while running with N_2 in comparison to Xe and delivers lower thrusts. The post processing of the curves shows that at optimal N_2 gas flow (8.5 SCCM) and 450 W total-power, the thruster can achieve 5.14 $\pm$0.20 mN. The same thrust can be also reached with lower gas flows (down to 6 SCCM) but higher powers or with higher gas flows (up to 12 SCCM) and lower powers. For an increased gas flow of 10 SCCM for example, a maximum thrust of 5.23 $\pm$0.20 mN at 450 W is reachable.

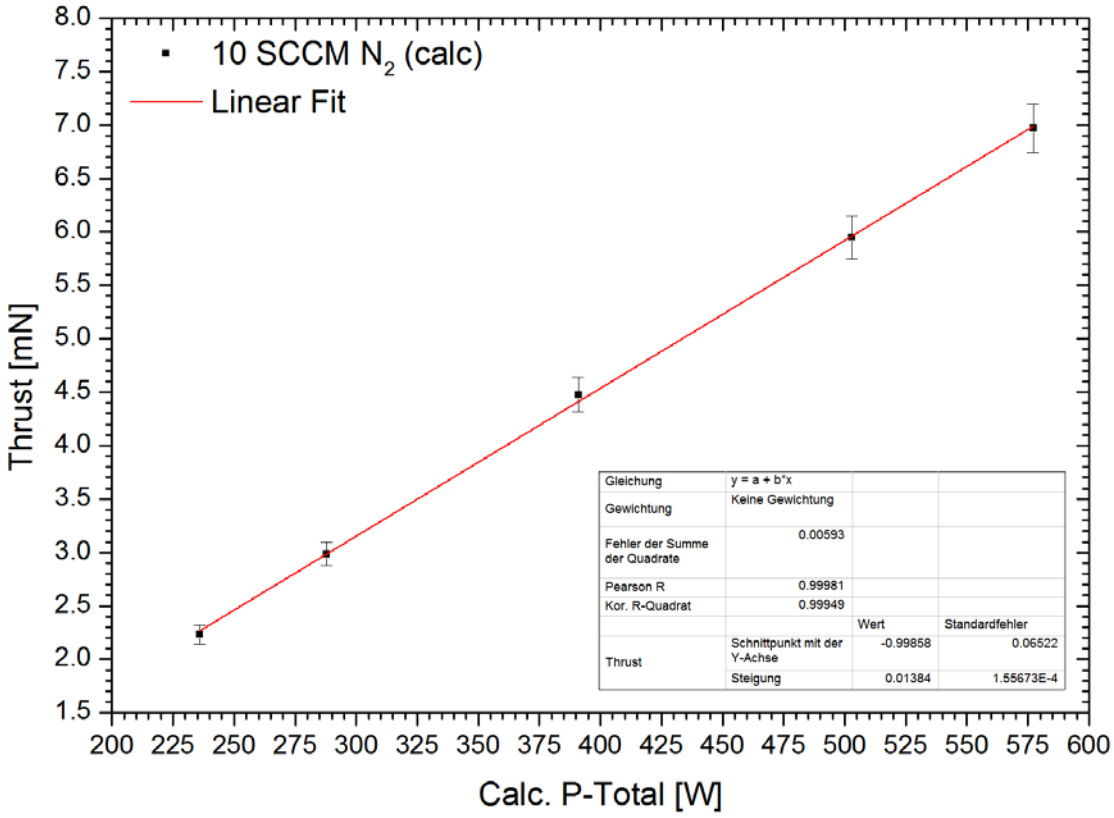

Figure 4-27: Power consumption interpolated for different thrusts at 10 SCCM gas flow

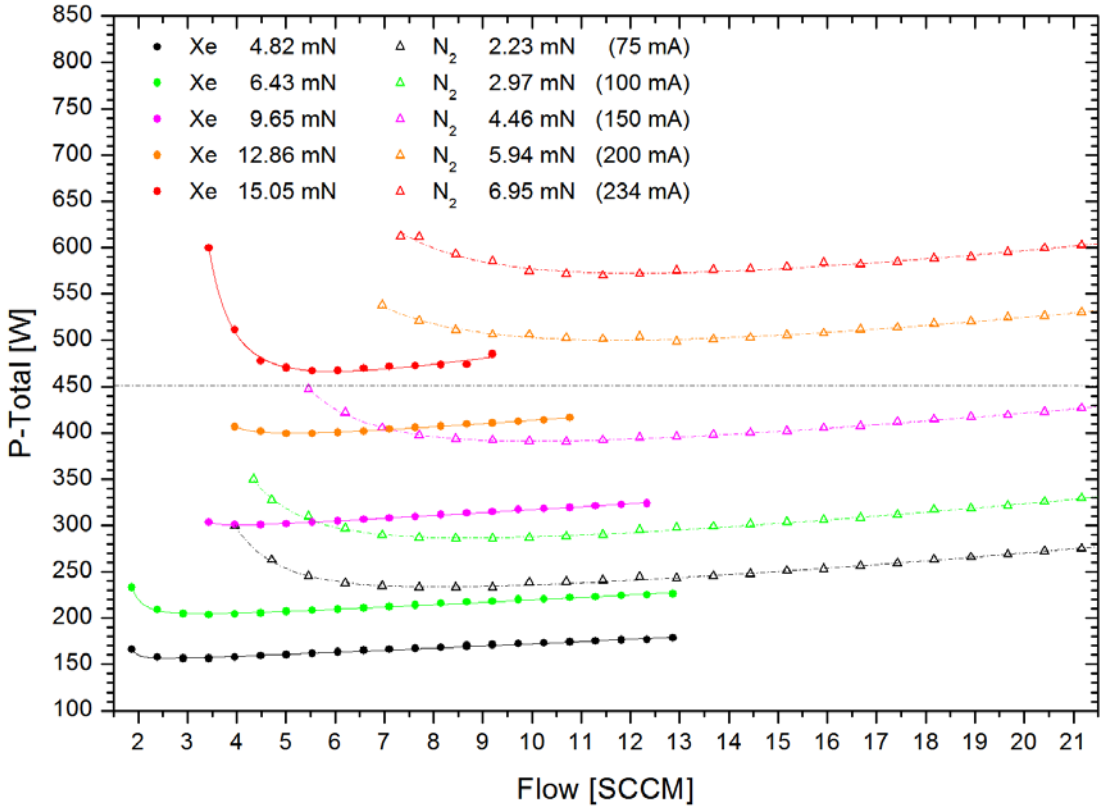

Figure 4-28: Performance comparison between Xe and N_2

4.5.3. Ten hours long run test with Nitrogen

The thruster was operated for 10 hours at a beam level of 150 mA continuously. The test parameters which were used for this test are specified in the following Table 4-18. During this test no beam current controller was used, the thruster was operated in open loop condition. The overall thrust stability of this thruster, even without an active regulating system was very good. Only small thermal drifts have been measured. The beam fluctuations, which can be seen in Figure 4-29, were caused by an automatic "shut off" of the NHV-supply, due to arcing. The therefore reduced extraction voltage explains the drop of the extracted beam current. The thruster continued to run, but the data acquisition stopped due to an error. There was no beam out in this test. This demonstrates that the rf-generator can carry the impedance changes of an arcing thruster, especially in combination with well-defined protection hardware. To stay at the requested beam level, the rf-power of the thruster was manually adjusted on occasion.

I_{Beam} [mA]	Mass flow [SCCM]	U_{PHV} [V]	U_{NHV} [V]
150	10.72	1500	-600

Table 4-18: Thruster parameter for the ten hours long run test with N_2

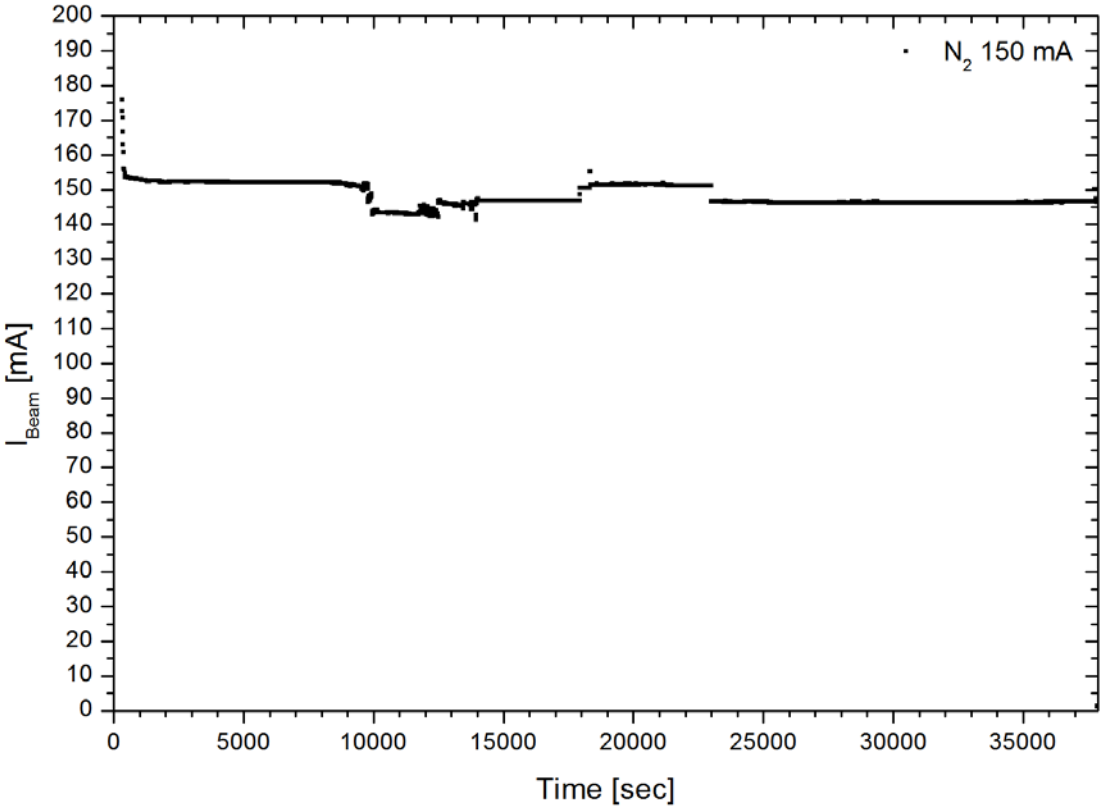

Figure 4-29: 10 hours long run test for N_2

4.5.4. Grid measurements after Nitrogen test

The grid measurements are performed as described in the chapter 3.2.5.2. The accel and the screen grid were investigated. The measured results are shown below in Table 4-19. Based on the measured data it could be determined, that the erosion, occurred during the test campaign, is under the measurement precision. All measured holes have the same diameter as before; the small deviations are under the precision of the measurement and the manufacturing (maximum deviation of 0.02 mm). No erosion could be measured.

Hole No.	Branch	Accel - top			Accel - bottom			Screen - top		
		h-Ø [mm]	v-Ø [mm]	Initial [mm]	h-Ø [mm]	v-Ø [mm]	Initial [mm]	h-Ø [mm]	v-Ø [mm]	Initial [mm]
1	A	2.00	2.00	2.00	2.01	2.03	2.00	3.19	3.19	3.20
2	A	1.99	2.00	2.00	1.99	1.99	2.00	3.19	3.18	3.20
3	A	2.00	2.00	2.00	1.99	1.99	2.00	3.19	3.19	3.20
4	A	2.00	2.00	2.00	1.99	1.99	2.00	3.20	3.19	3.20
5	A	2.00	2.01	2.00	1.99	1.99	2.00	3.19	3.19	3.20
6	A	2.02	2.02	2.00	2.02	2.02	2.00	3.20	3.18	3.20
1	B	2.00	2.00	2.00	2.00	2.00	2.00	3.20	3.19	3.20
2	B	2.01	2.00	2.00	2.03	2.00	2.00	3.20	3.19	3.20
3	B	2.00	2.00	2.00	1.99	1.99	2.00	3.19	3.18	3.20
4	B	2.00	2.00	2.00	2.00	2.00	2.00	3.20	3.19	3.20
5	B	2.00	2.00	2.00	2.00	2.00	2.00	3.19	3.18	3.20
6	B	2.02	2.02	2.00	2.02	2.02	2.00	3.19	3.18	3.20
1	C	1.99	2.00	2.00	2.01	2.00	2.00	3.20	3.20	3.20
2	C	1.99	1.99	2.00	2.01	1.99	2.00	3.20	3.18	3.20
3	C	2.00	1.99	2.00	2.01	2.00	2.00	3.19	3.19	3.20
4	C	2.00	2.00	2.00	2.01	2.00	2.00	3.20	3.19	3.20
5	C	2.00	1.99	2.00	2.01	2.01	2.00	3.19	3.19	3.20
6	C	2.02	2.00	2.00	2.03	2.03	2.00	3.20	3.19	3.20

Table 4-19: Grid Measurements after N_2 test campaign

4.5.5. Summary of the N_2 campaign

The functional and lifetime test is considered as successful, as the performance values for five current levels are measured, the 10 hours long run test is performed and the thruster changes are measured. We couldn't see any changes in thruster before and after the tests. To see the changes, a longer running of the thruster is needed.

4.6. Test campaign with Oxygen

The results of the Oxygen test campaign are reported in this chapter. The impact on the thruster lifetime and on the thruster performance are measured and compared to the previously performed test data of the other propellants (N_2 and Xe).

4.6.1. Performance check with Xe

To crosscheck the thruster performance and to verify the thruster health after the completion of the O_2 test campaign, the thruster performance with Xe before and after the test is compared. The nominal operation point of the RIT-10 operating on ARTEMIS was used as reference. The operated values and gained results are shown in the table

	I_{Beam} [mA]	U_{PHV} [V]	U_{NHV} [V]	Measure RF-Power [W]	Calc. Thrust [mN]	Mass flow [SCCM]
Before O_2	234	1500	-600	115	15	5.00
After O_2	234	1500	-600	116	15	5.00

Table 4-20: Settings for performance check with Xe

4.6.2. Performance mapping with Oxygen

Figure 4-30: RIT-10-EBB thruster running with O_2

The thruster's performance was characterized by variation of the mass flow whilst the beam current is kept constant, as described in chapter 3.2.5.1. The thruster was operated with 15-20 different mass flow rates on each beam current level. For each point of operation the full set of parameters was recorded. Each single operational point was operated until performance equilibrium was reached. Normally the performance equilibrium was reached after few minutes whereas the full thermal equilibrium was reached after 3-4 hours.

The thruster performance was characterized for the 5 levels of beam current:
75 mA, 100 mA, 150 mA, 200 mA and 234 mA.

No	I_{Beam} [mA]	U_{PHV} [V]	U_{NHV} [V]	Max. RF-Power (Artemis) [W]	Thrust (calc.) [mN]	Mass flow [SCCM]	Operation Time [min]
1	75	1500	-600	338	2.36	3.5 - 15	> 15
2	100	1500	-600	299	3.15	4 - 15	> 15
3	150	1500	-600	226	4.73	5 - 15	> 15
4	200	1500	-600	151	6.30	5 - 15	> 15
5	234	1500	-600	100	7.37	6 - 15	> 15

Table 4-21: Parameters for performance mapping with O_2

The measured performances for Oxygen as a propellant after the post-processing are shown in Figure 4-31 and Figure 4-32.

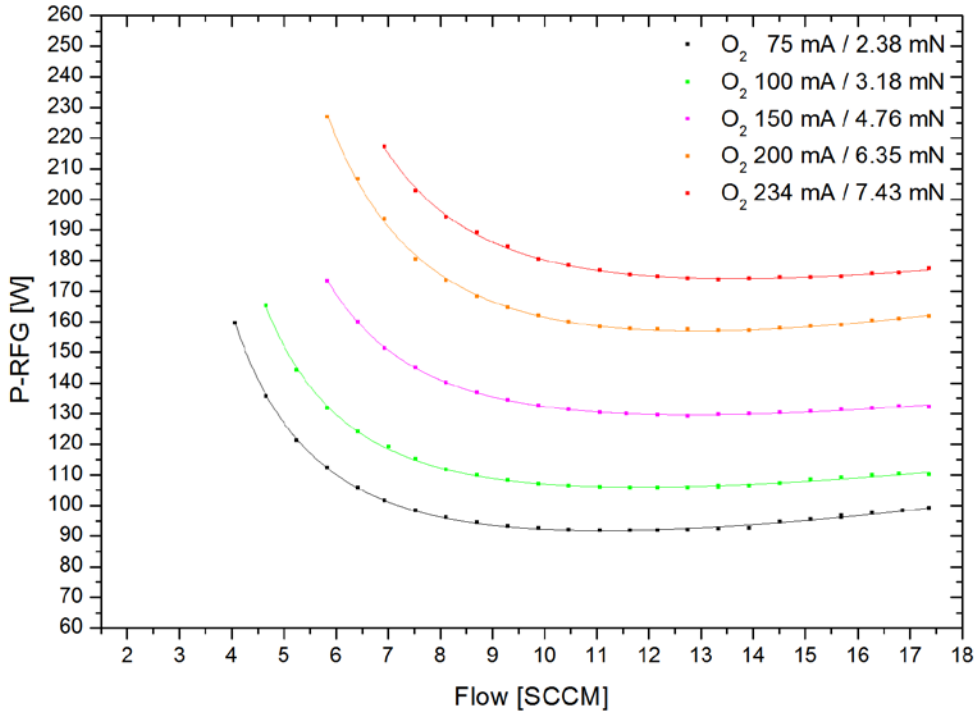

Figure 4-31: Performance overview for O_2

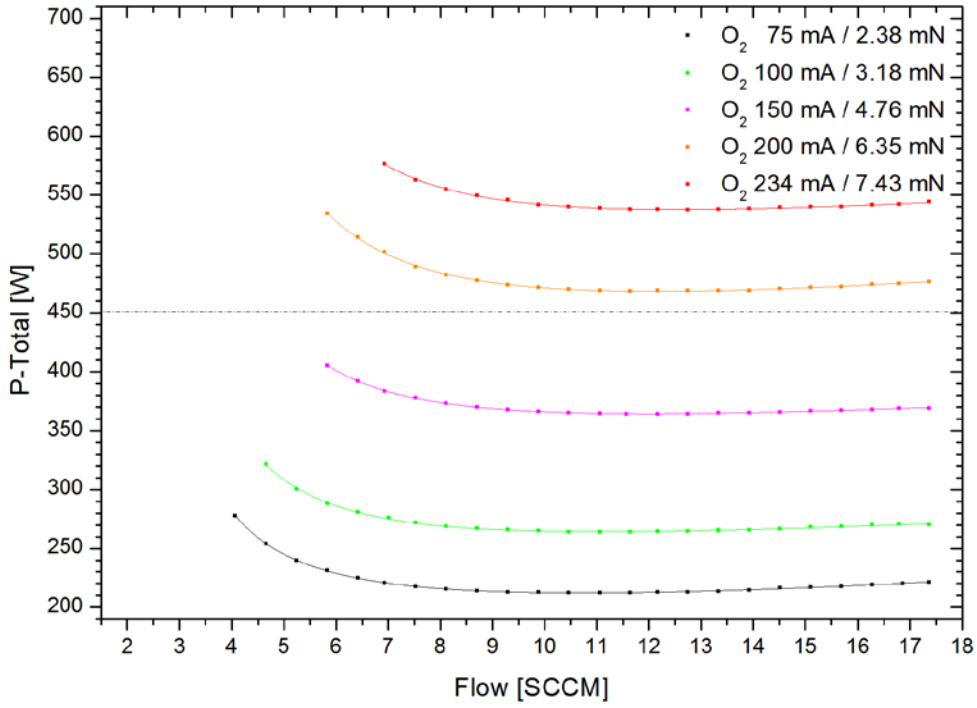

Figure 4-32: Performance overview of P-Total for O_2

Figure 4-34 covers the measurements on Xe and O_2 simultaneously. In these graphs, the total needed power for different values of thrust and different gas flows is shown. The y-axis

shows the maximum available power for the RIT thruster. The RIT-10-EBB thruster needs higher amount of gas and total power, when running with O_2 in comparison to Xe and delivers lower thrusts. The post processing of the curves shows that at optimal O_2 gas flow and 450 W total power, the thruster can achieve about 6.03 $\pm$0.21 mN (see Figure 4-33). The same thrust can be also reached with lower gas flows (down to 6 SCCM) but higher powers or with higher gas flows (up to 12 SCCM) and lower powers.

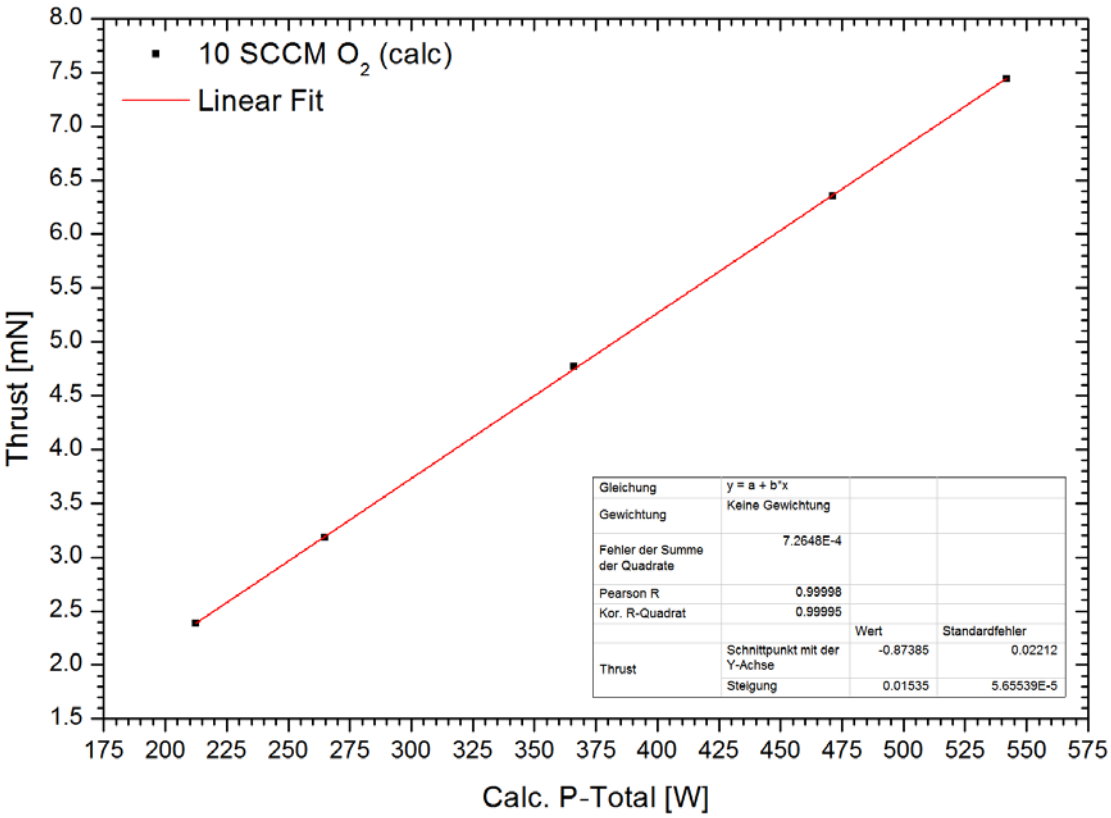

Figure 4-33: Power consumption interpolated for different thrusts at 10 SCCM gas flow

Figure 4-37 shows the comparison between the performance curves of the thruster running with Oxygen and Nitrogen. It shows that as it was expected through the mass ratio of N_2 and O_2, the maximum reachable thrust is higher for Oxygen than for Nitrogen. As the ionization energy of both gases is comparable, there is not a large difference between the power consumptions.

It is to mention: During the tests with O_2, a rising discrepancy between the directly measured thrust by the thrust balance and the calculated value (see Figure 5-10 in the discussion) for Oxygen at 234 mA beam current was seen. This discrepancy is especially higher by higher powers. It can be assumed, that this behavior is due to the dissociation of O_2 into O. With higher dissociation degrees, the thrust to beam energy ratio will be lower, as more ions come out of the thruster with half of the mass (atomic Oxygen = O). This effect could not be seen in the Nitrogen test, but the fact, that the dissociation energy of the Nitrogen molecules is higher than the one of Oxygen molecules (~9.8 eV in N_2 comparison to ~5.2 eV for O_2) can deliver the explanation.

For a quantitative and exact declaration of the phenomena, an intensive beam diagnostics with mass and energy selective systems is necessary.

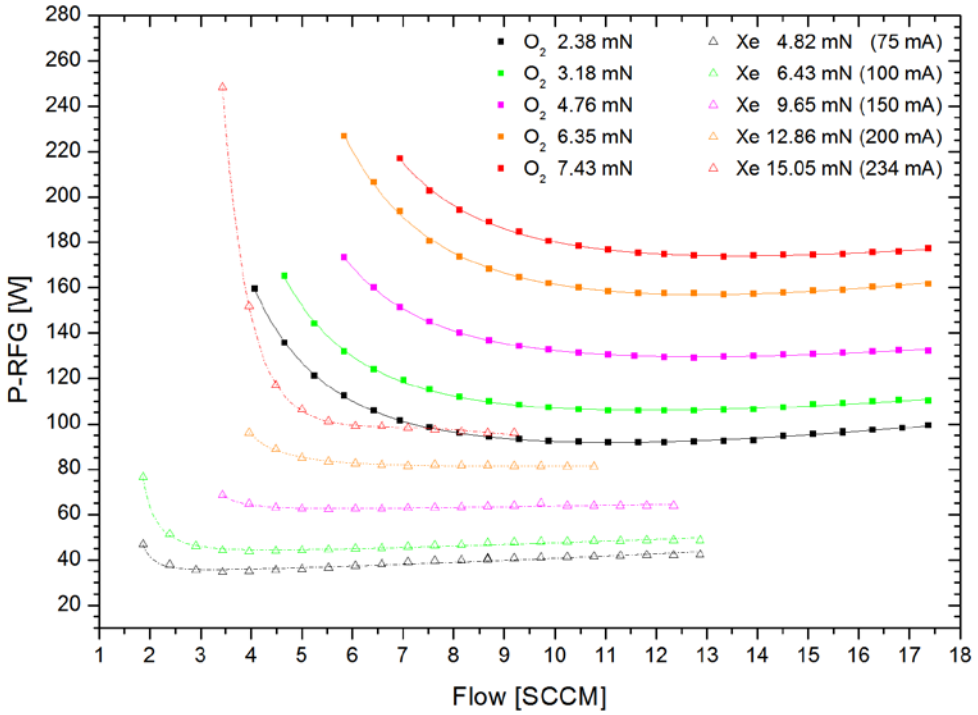

Figure 4-34: RAM-EP-10 thruster performance curves for O_2 and Xe for different beam currents and 1500 V beam voltage

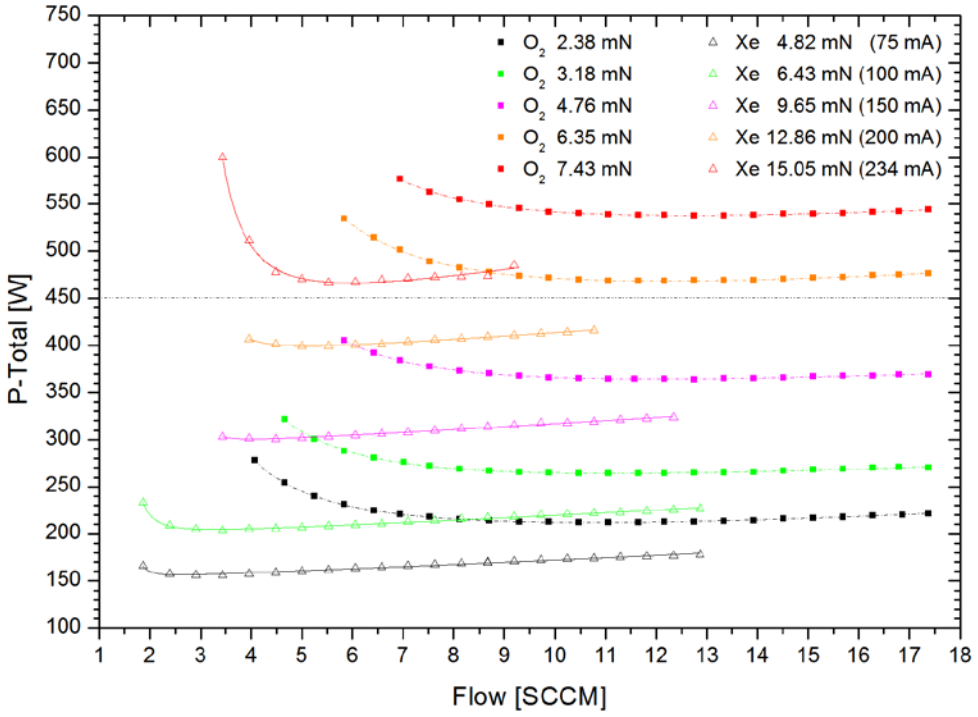

Figure 4-35: RAM-EP-10 thruster performance curves for O_2 and Xe with respect to the total power

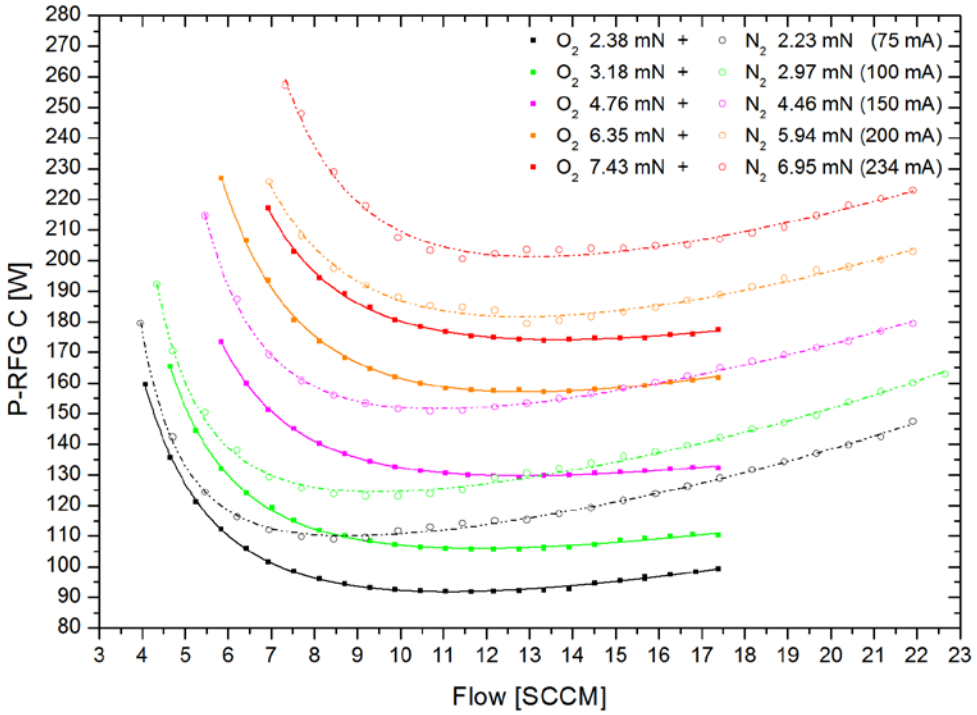

Figure 4-36: RAM-EP-10 thruster performance curves for N_2 and O_2

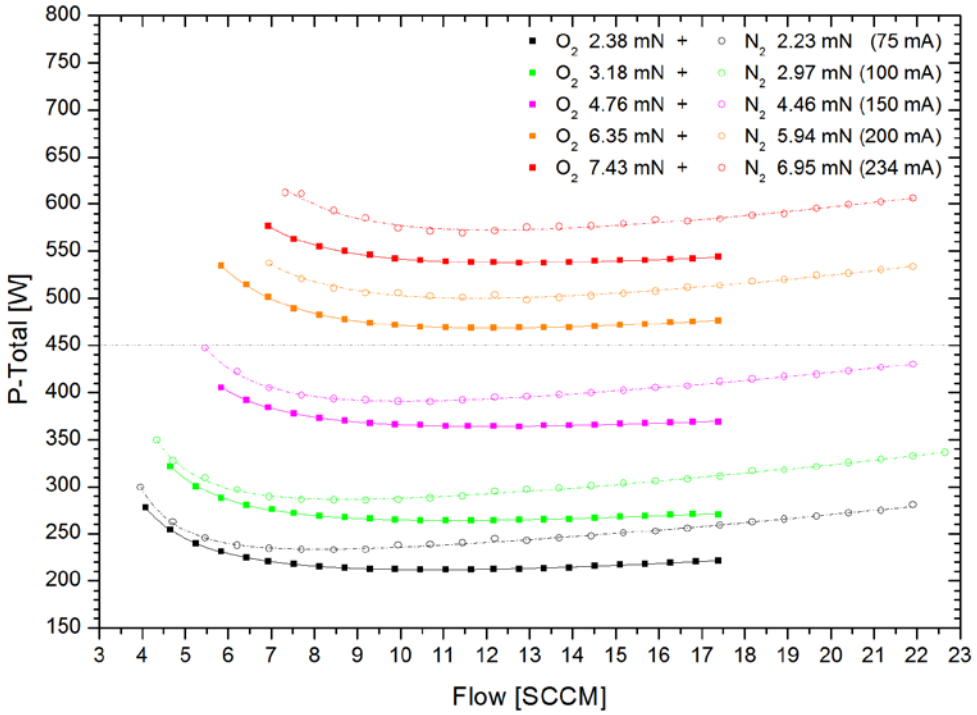

Figure 4-37: RAM-EP-10 thruster performance curves for N_2 and O_2, P-Total

4.6.3. Ten hours long run test with Oxygen

The thruster was operated with a beam level of 150 mA for 10 hours continuously. The thruster parameters were set according to Table 4-22.

I_{Beam} [mA]	Mass flow [SCCM]	U_{PHV} [V]	Cal. Thrust [mN]	U_{NHV} [V]
150	11.57	1500	4.76	- 600

Table 4-22: Operational parameter for 10 hours continuous operation test

During this test, the negative high voltage power supply had two times arcing, which led to automatic "Turn Off" of the NHV. The thruster continued to run, but the data acquisition stopped due to an error. To establish seamless thruster operation the control system was not restarted. There was no beam out in this test, but the thruster data were recorded manually. Photos of the firing thruster are taken in parallel to document the normal operation. The Figure 4-38 shows the developing of the beam current during this test.

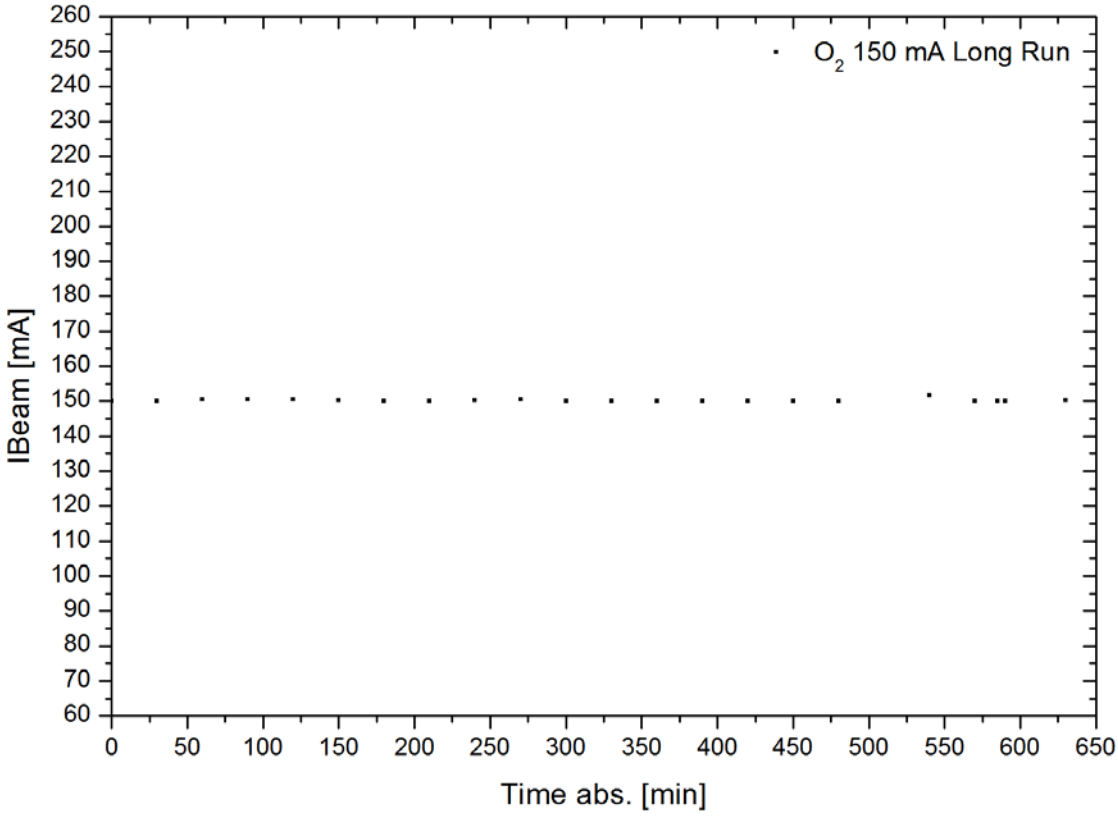

Figure 4-38: The ion beam current during the long firing test O_2

4.6.4. Grid erosion measurements O_2

The grid erosion was measured optically before the functional test and after the long run test according to the procedure described in 3.2.5.2.

The photos were taken with the described Pixellink firewire camera with a fixed focal length. The relevant holes were marked with the paper mask (Figure 3-33). The post processing of the pictures was done with Photoshop 5 Extended. The needed calibration and correlation factor was computed and verified from a series of slit pictures (Figure 3-26 to Figure 3-30).

Hole No.	Branch	Accel - top			Accel - bottom		
		h-Ø [mm]	v-Ø [mm]	Initial [mm]	h-Ø [mm]	v-Ø [mm]	Initial [mm]
1	A	2.20	2.17	2.00	2.10	2.07	2.00
2	A	2.16	2.15	2.00	2.10	2.06	2.00
3	A	2.16	2.13	2.00	2.08	2.06	2.00
4	A	2.13	2.11	2.00	2.06	2.05	2.00
5	A	2.10	2.10	2.00	2.06	2.04	2.00
6	A	2.07	2.06	2.00	2.02	2.05	2.00
1	B	2.12	2.17	2.00	2.06	2.10	2.00
2	B	2.12	2.16	2.00	2.06	2.11	2.00
3	B	2.10	2.13	2.00	2.04	2.10	2.00
4	B	2.08	2.13	2.00	2.03	2.11	2.00
5	B	2.07	2.11	2.00	2.01	2.07	2.00
6	B	2.04	2.07	2.00	2.01	2.11	2.00
1	C	2.15	2.13	2.00	2.10	2.08	2.00
2	C	2.16	2.14	2.00	2.10	2.07	2.00
3	C	2.15	2.13	2.00	2.12	2.07	2.00
4	C	2.13	2.11	2.00	2.07	2.04	2.00
5	C	2.11	2.09	2.00	2.06	2.04	2.00
6	C	2.08	2.05	2.00	2.09	2.06	2.00

Table 4-23: Grid erosion measurements after O_2 tests

4.6.5. Conclusion O_2 test campaign

The performance characterization test and the long firing test were successfully performed.

Performance values for the selected five beam current levels have been measured.

During the 10 hours of long firing test the changes in the thruster performance have been measured.

The grid erosion is noticeable higher than with Nitrogen. As the sputtering rate of Graphite under ion beams of Oxygen and Nitrogen is merely the same, the difference can be expected in chemical processes between Graphite and the Oxygen.

4.7. Test campaign with gas mixtures and modified thruster

The results from the performance characterization of the modified RIT-10-EBB (RAM-RIT-10) are reported in this chapter. According to the description a new Titanium accel grid and an impedance transformation was installed, to increase the grid lifetime and to improve the rf-coupling.

4.7.1. Performance check Xe, N_2 and O_2

The performance mapping of the RIT-10-EBB, after the reconstruction of the grid system for this activity had to be cross checked with the performance values of the same thruster before the reconstruction measured in the previous tests in this activity. The thruster performances had to be characterized and compared with each other at a beam current of 150 mA.

From the other side the performance of the thrusters had been measured before, during and after the lifetime test. Figure 4-40 shows the performance check curve of the Xe at three different time points; the beginning of the tests, before starting the lifetime test and after the lifetime test.

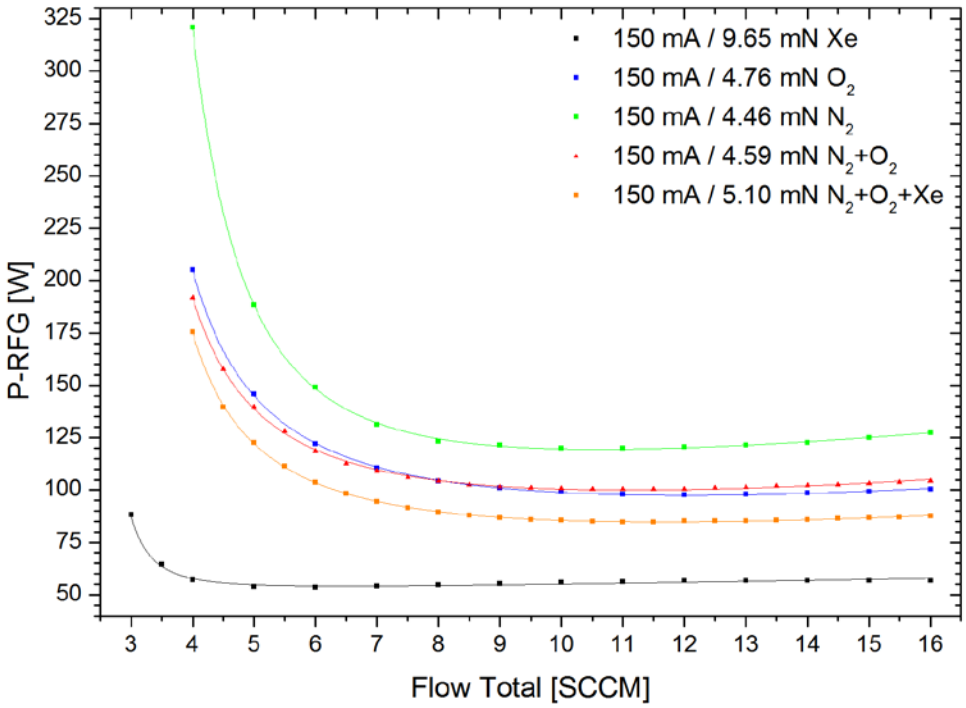

Figure 4-39: Performance overview of the different propellants at 150 mA I_{Beam}

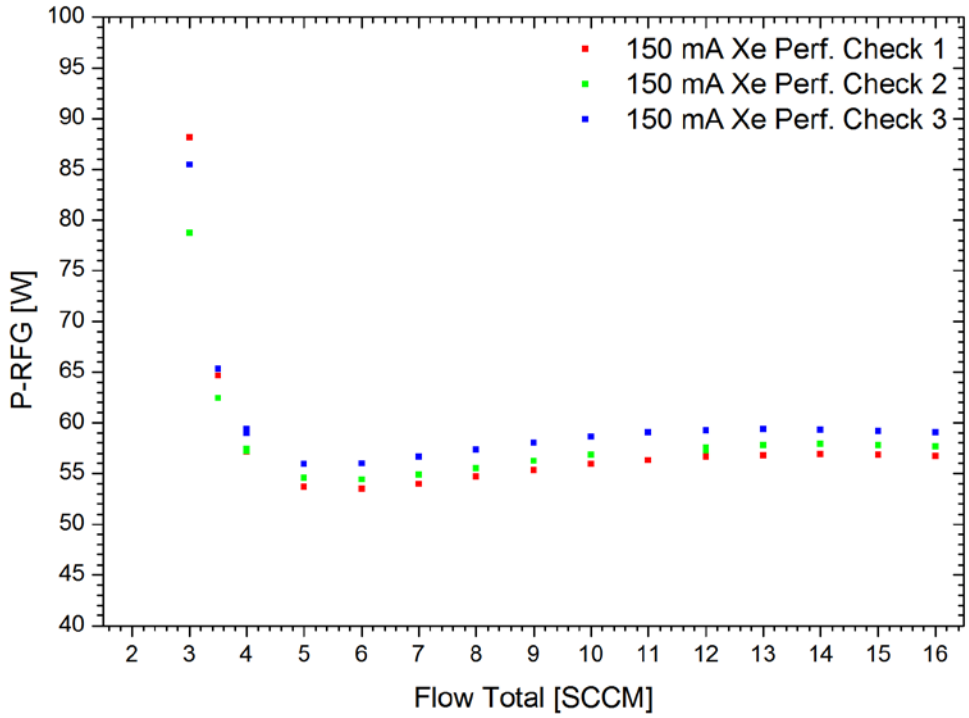

Figure 4-40: Performance check with Xenon at the beginning of the tests, before the starting the lifetime test and after the lifetime test

The small discrepancy between the curves is assumed to be due to the covering of the quartz discharge chamber by the sputter material coming back from the facility. The amount of the discrepancy is however with few watts in the frame of the experiment precision.

A larger discrepancy is observed in comparing the power consumption of the thruster before and after the thruster reconstruction. These discrepancies are shown in Figure 4-41. The power consumption is as expected considerably lower. It is due to the fact that with a impedance transformation of 1 to 3, the input impedance of the thruster is 3 times higher, so the current in the rf-coil of the thruster will be lower and so the ohmic loss in the thruster. The most benefit is gained for the gases, which had the highest currents in this case the Nitrogen, followed by Oxygen and Xenon.

Figure 4-41 shows the thruster impedance after and before the reconstruction and depending on the gas.

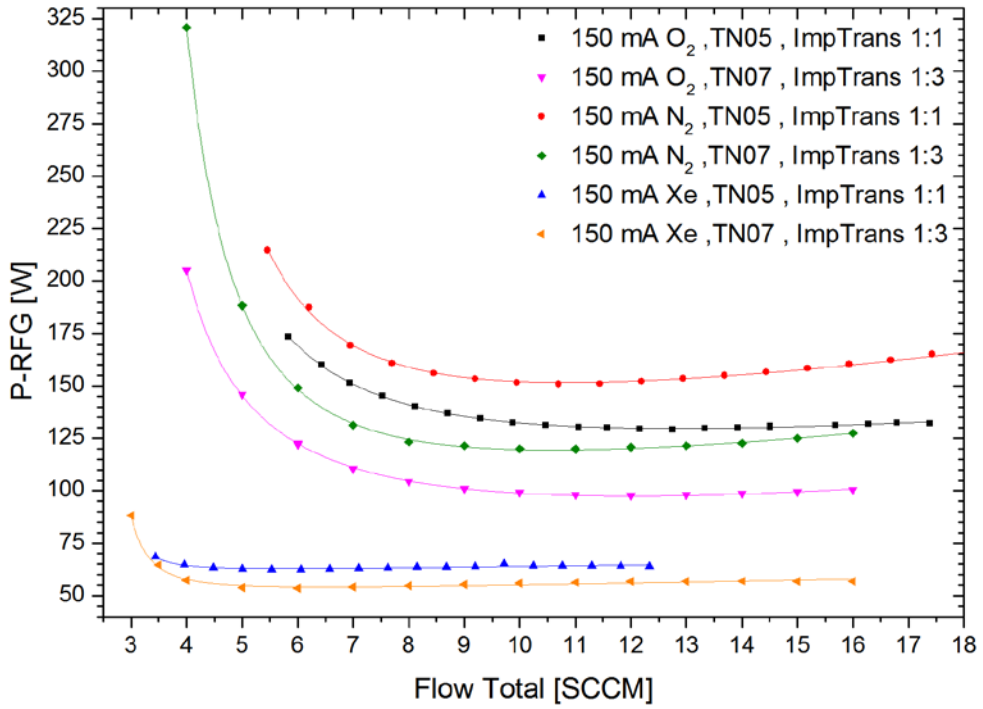

Figure 4-41: The comparison between the power consumption of the RIT-10-EBB thruster before (Imp-Trans 1:1) and after (Imp-Trans 1:3) the reconstruction (RAM-RIT-10)

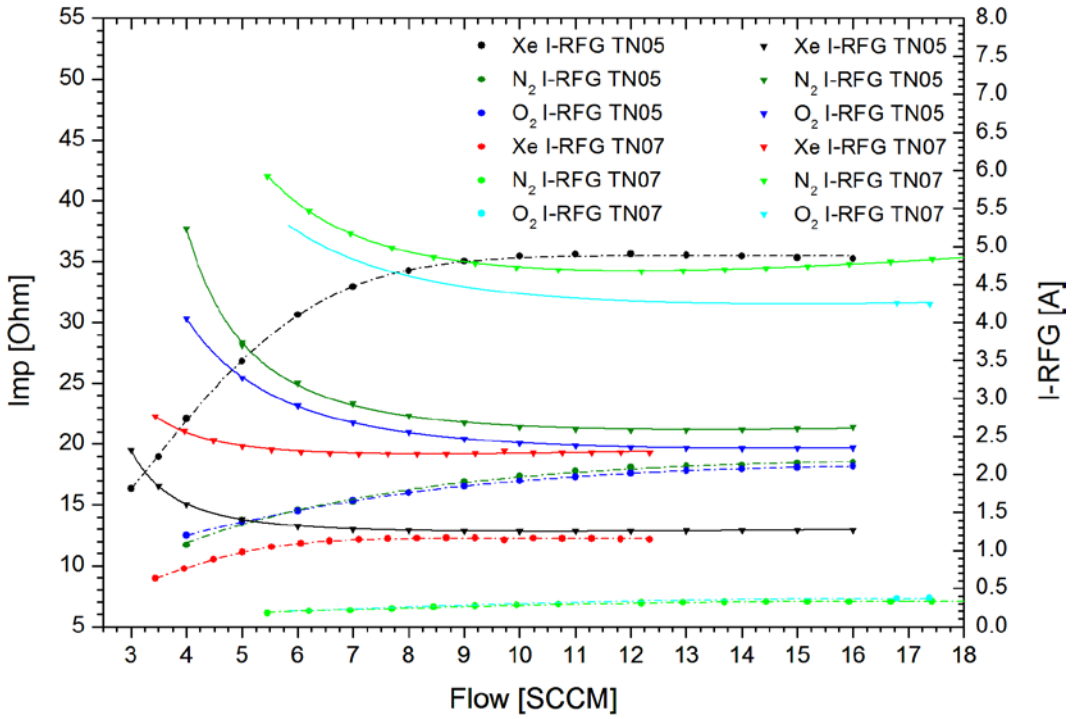

Figure 4-42: The comparison between the impedance and the correlated RFG-current of the RIT-10-EBB thruster before (Imp-Trans 1:1) and after (Imp-Trans 1:3) the reconstruction (RAM-RIT-10)

4.7.2. Performance mapping with N_2 + O_2 mixture

Figure 4-43: RAM-RIT-10 thruster running with N_2+O_2 at 75 mA beam-current

The thruster's performance was characterized by following the described procedure in chapter 3.2.5.1 variation of the mass flow whilst the beam current was kept constant. The thruster was operated with 20-25 different mass flow rates on each beam current level. For each point of operation the full set of parameters were recorded. Each single operational point was operated until the performance equilibrium was reached. Normally the performance equilibrium was reached after a few minutes (~5 minutes), whereas the full thermal equilibrium would have been reached after 3-4 hours.

The thruster performance was characterized for 5 levels of beam current: 75 mA, 100 mA, 150 mA, 200 mA and 234 mA.

No	I_{Beam} [mA]	U_{PHV} [V]	U_{NHV} [V]	Thrust (calc.) [mN]	mT set [SCCM]
1	075	1500	-600	2.30	3.5 - 16
2	100	1500	-600	3.06	4 - 16
3	150	1500	-600	4.59	4 - 16
4	200	1500	-600	6.12	5 - 16
5	234	1500	-600	7.16	5 - 16

Table 4-24: Settings for performance characterization with N_2+O_2 mixture

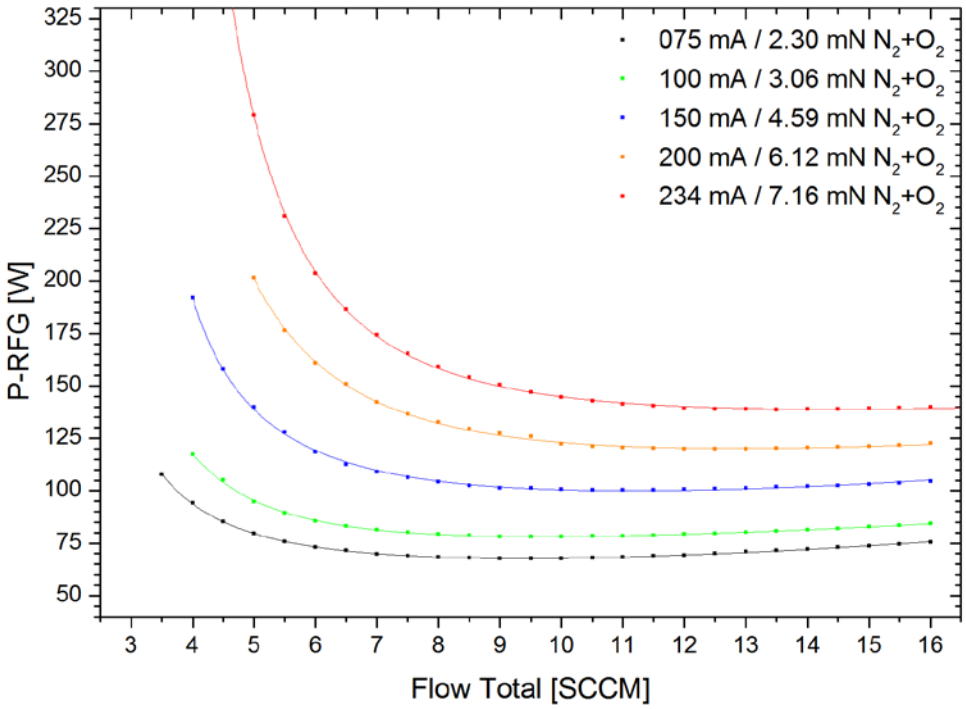

Figure 4-44: N_2+O_2 Overview for different ion beams for 1500 V beam voltage

Figure 4-44 shows all the measurements for N_2+O_2 after the processing. Figure 4-46 covers the measurements of the total power consumption (PHV-Power + NHV-Power + RFG-Power + RFG-Aux-Power) for different thrust values and flow rates. The horizontal black line shows the maximum available power for the RIT thruster. The post processing of the curves shows that at optimal N_2+O_2 gas flow and 450 W total power, the thruster can achieve about 6.33 $\pm$0.23 mN (see Figure 4-45) with 10 SCCM N_2+O_2. Compared to the power to thrust ration for only Oxygen (6 mN at 450 W) the reachable thrust level could be increased by 0.30 mN. These thrust can be also reached with lower gas flows (down to 6 SCCM) but higher powers or with higher gas flows (up to 14 SCCM) and lower powers. For higher flow rates the losses on the second grid would be too high because of the higher charge exchange rates. This affects the lifetime of the grid.

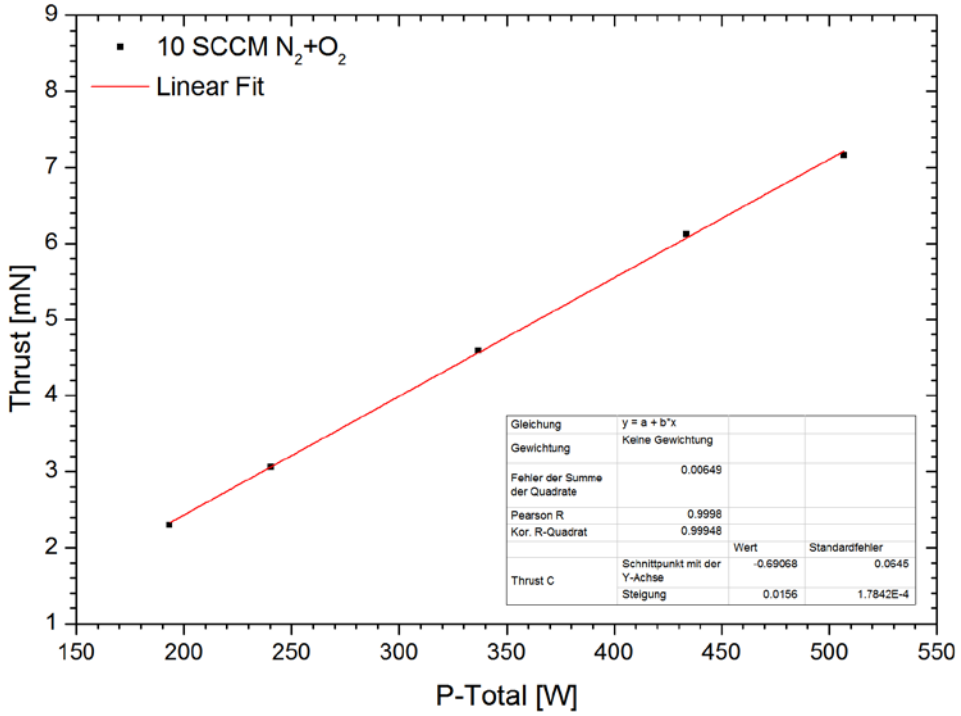

Figure 4-45: N_2+O_2 power consumption interpolated for different thrusts at 10 SCCM gas flow

The Figure 4-46 illustrates total power consumption related to the given mass flows. The comparison between the power consumption of N_2+O_2 mixture with the single propellants N_2 and O_2 at 150 mA I_{Beam} shows that the gas mixture is less sensitive to dissociation losses and that the needed power of N_2+O_2 is at the power level of the O_2. This comparison is shown in Figure 4-47.

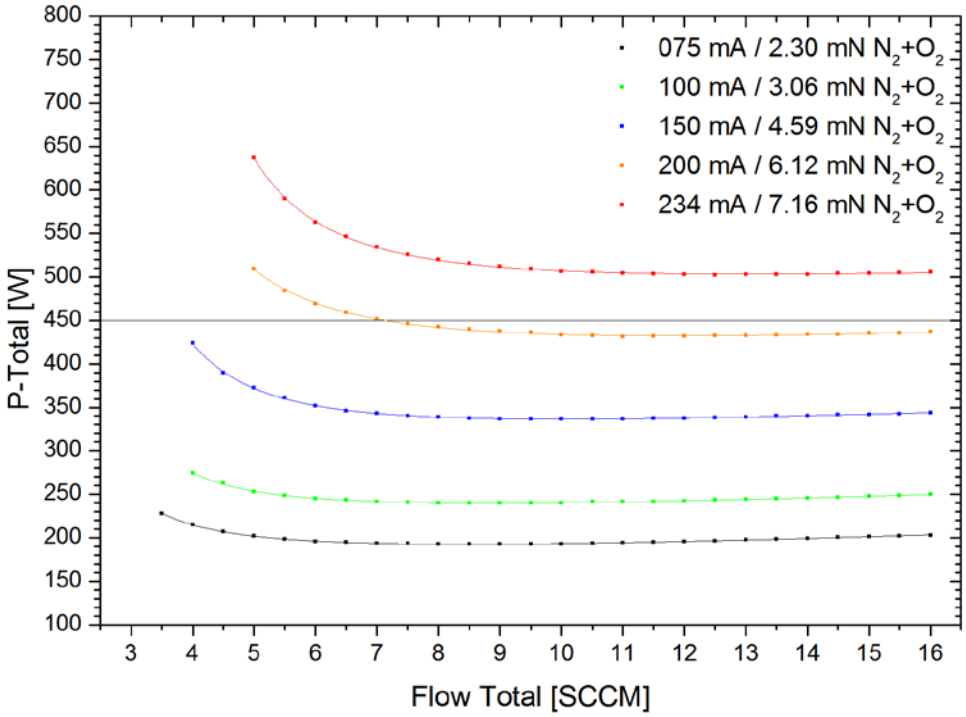

Figure 4-46: RAM-EP-10 thruster performance curves for N_2+O_2 (total power)

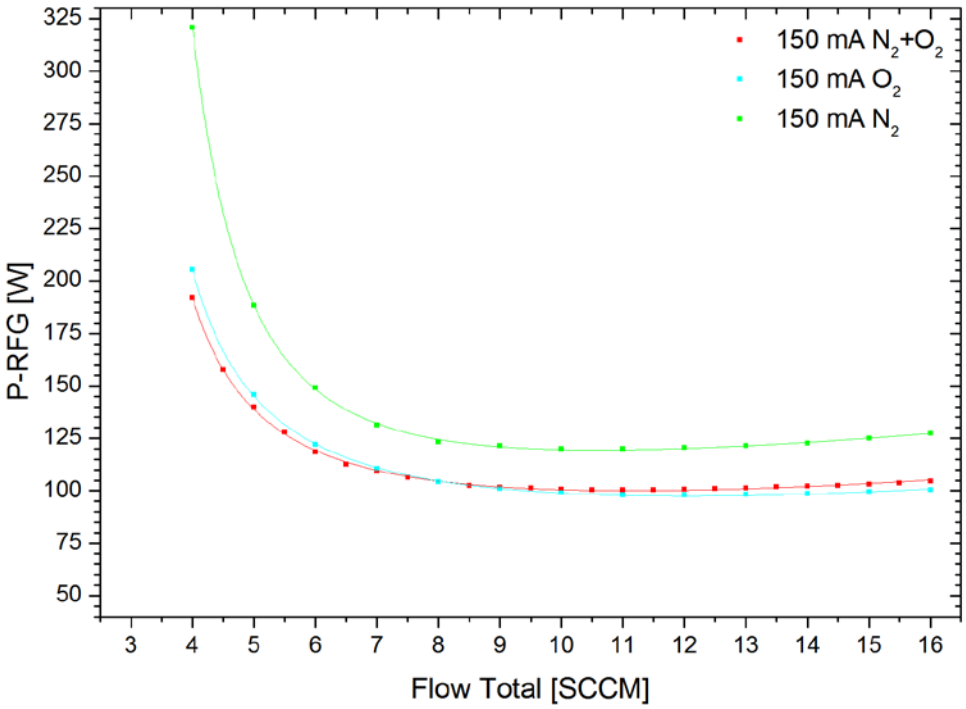

Figure 4-47: Performance comparison between O_2, N_2 and N_2+O_2 mixture @150 mA I_{Beam}

4.7.3. Performance mapping with N_2 + O_2 + Xe mixture

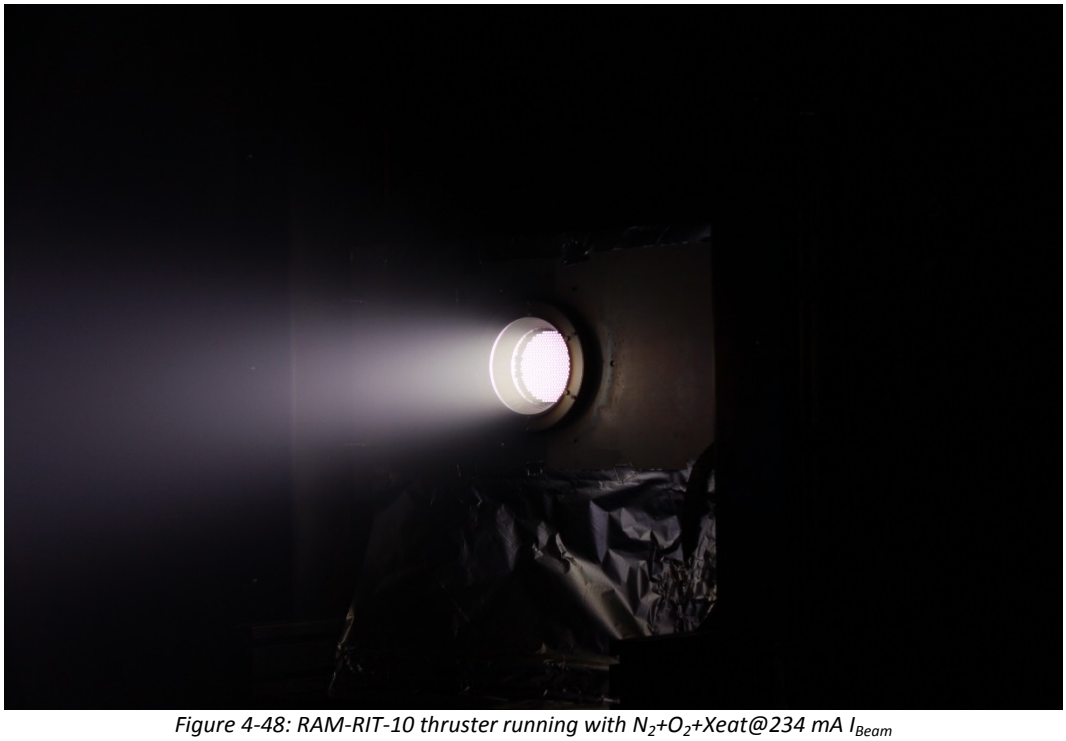

Figure 4-48: RAM-RIT-10 thruster running with N_2+O_2+Xeat@234 mA I_{Beam}

As described in chapter 3.2.5.1 the thruster's performance was characterized by variation of the mass flow whilst the beam current was kept constant. The thruster was operated with 20-25 different mass flow rates on each beam current level. For each point of operation the full set of parameters was recorded. Each single operational point had been operated for

~5 minutes until the performance equilibrium was reached. Normally the performance equilibrium was reached after a few minutes, whereas the full thermal equilibrium would have been reached after 3-4 hours.

The thruster performance was characterized for the same 5 levels of beam current: 75 mA, 100 mA, 150 mA, 200 mA and 234 mA. But this time 10 % of Xenon was mixed to the gas-composition as a support gas. The ratio between Nitrogen and Oxygen was still 1.27:1.

Again the effects of beam divergence and plasma potential are under the precision of the thrust measurement (about 3%).

No	I_{Beam} [mA]	U_{PHV} [V]	U_{NHV} [V]	Thrust [mN]	mT set [sccm]
1	075	1500	-600	2.55	4 - 16
2	100	1500	-600	3.40	4 - 16
3	150	1500	-600	5.10	4 - 16
4	200	1500	-600	6.80	5 - 16
5	234	1500	-600	7.95	5 - 16

Table 4-25: Settings for performance characterization with N_2+O_2+10 % Xe mixture

Figure 4-49 shows the measurement performance data of the RAM-RIT-10, running with N_2+O_2+Xe, after the post processing. The correlated thrust levels were also given to simplify the comparison.

The total power consumption of the RAM-RIT-10 thruster operated with N_2+O_2+Xe is given in Figure 4-50. Figure 4-51 and Figure 4-52 show the measurements on N_2+O_2 and N_2+O_2+Xe simultaneously. In these graphs, the RF-Power and the total needed power for different values of thrust and different gas flows are shown. The black horizontal line indicates the maximum available power for the RIT thruster. The RAM-RIT-10 thruster needs a higher amount of gas and total power, when running with N_2+O_2 in comparison to N_2+O_2+Xe and delivers lower thrusts. The positive impact of only 10 % Xenon is given but did not legitimate the need of having Xenon available. The post processing and interpolation of the curves show that at optimal N_2+O_2+Xe gas flow and 450 W total power, the thruster can achieve up to 7.28 $\pm$0.26 mN thrust at 10 SCCM (see Figure 4-53). This is slightly higher than without 10 % Xenon. The thrust gain is about 0.95 mN compared to N_2+O_2.This thrust level of 7.28 $\pm$0.26 mN can also be reached with lower gas flows (down to 6 SCCM) but higher powers or with higher gas flows (up to 14 SCCM) and lower powers. The negative impact on the grid lifetime of a too high gas flow has to be considered. The RAM-RIT-10 thruster can be operated with both gas mixtures but for the thruster there is clearly no need in using Xenon in addition to N_2+O_2. Also the focusing of the beam would not be optimal due to the huge mass difference between Xenon and the atmospheric gases, which would lead to ion impingement on the second grid. Therefore using Xenon would reduce the grid lifetime.

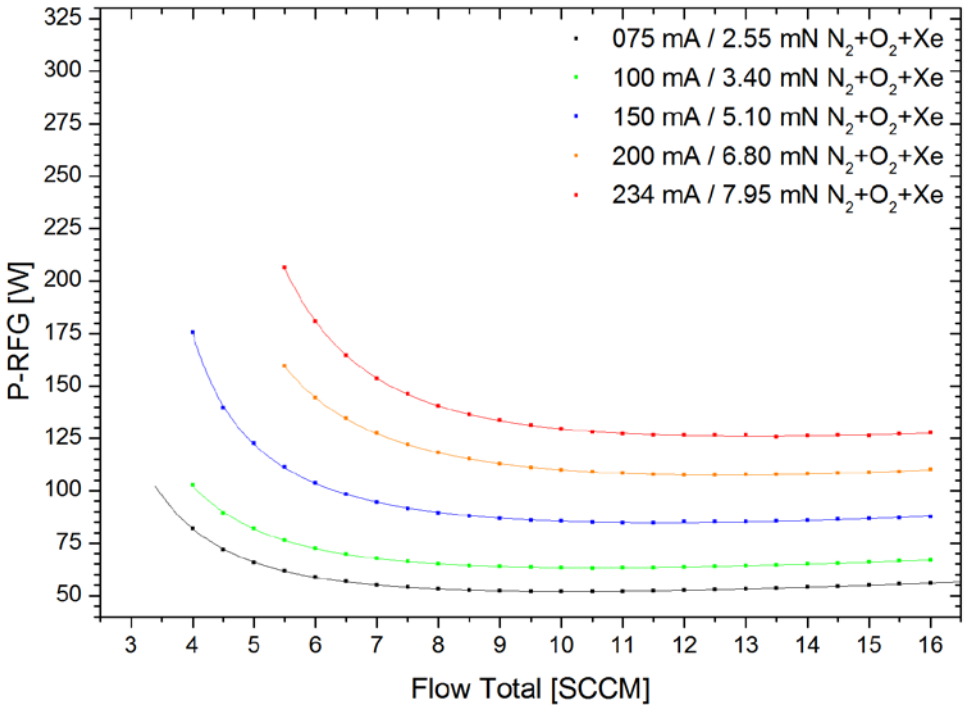

Figure 4-49: N_2+O_2+Xe overview for different ion beams for 1500 V beam voltage

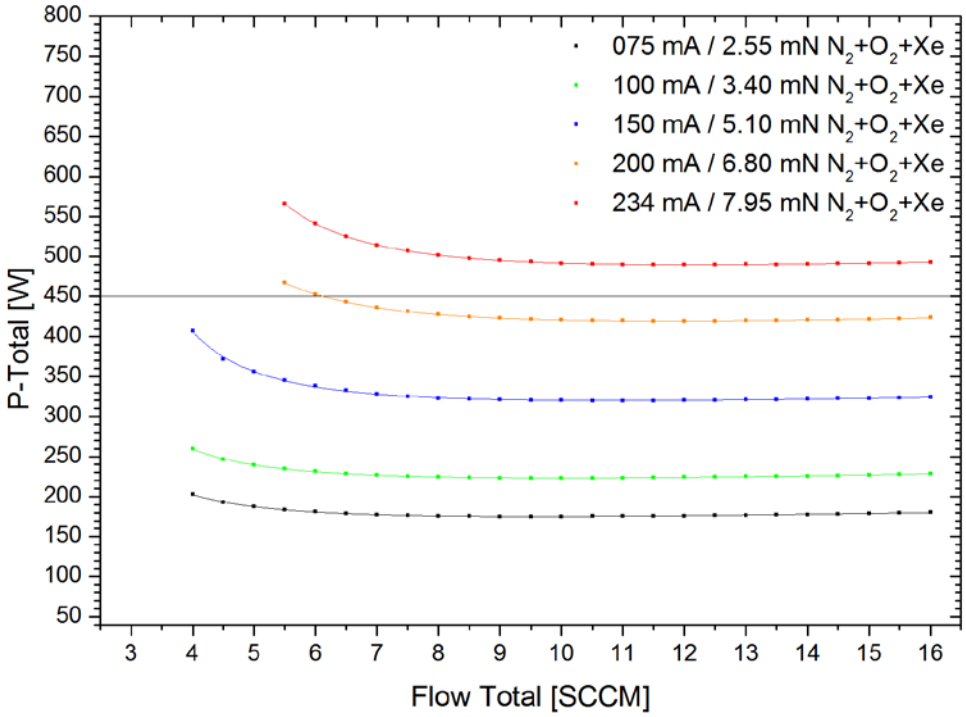

Figure 4-50: RAM-EP-10 thruster performance curves for N_2+O_2+Xe (total power)

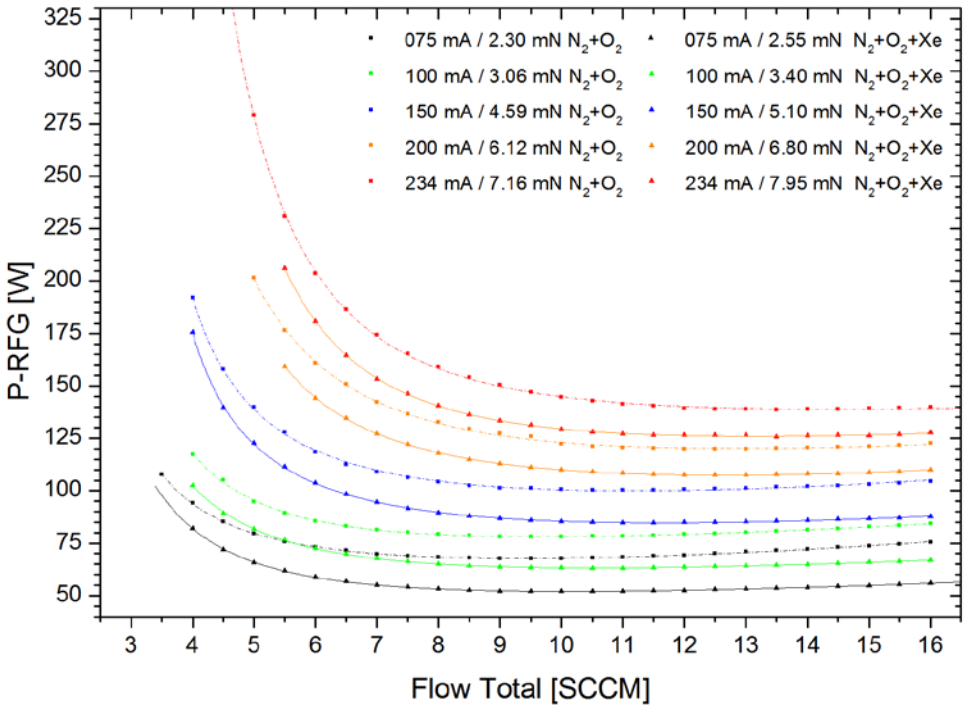

Figure 4-51: Performance overview for N_2+O_2 and N_2+O_2+Xe mixtures

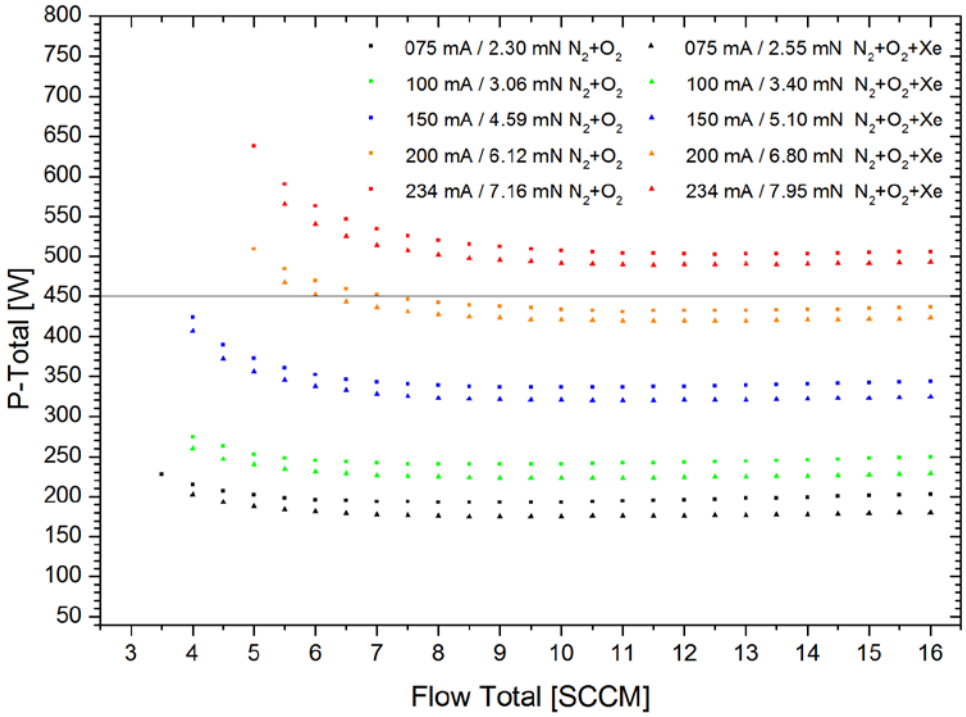

Figure 4-52: Performance overview for N_2+O_2 and N_2+O_2+Xe mixtures (total power)

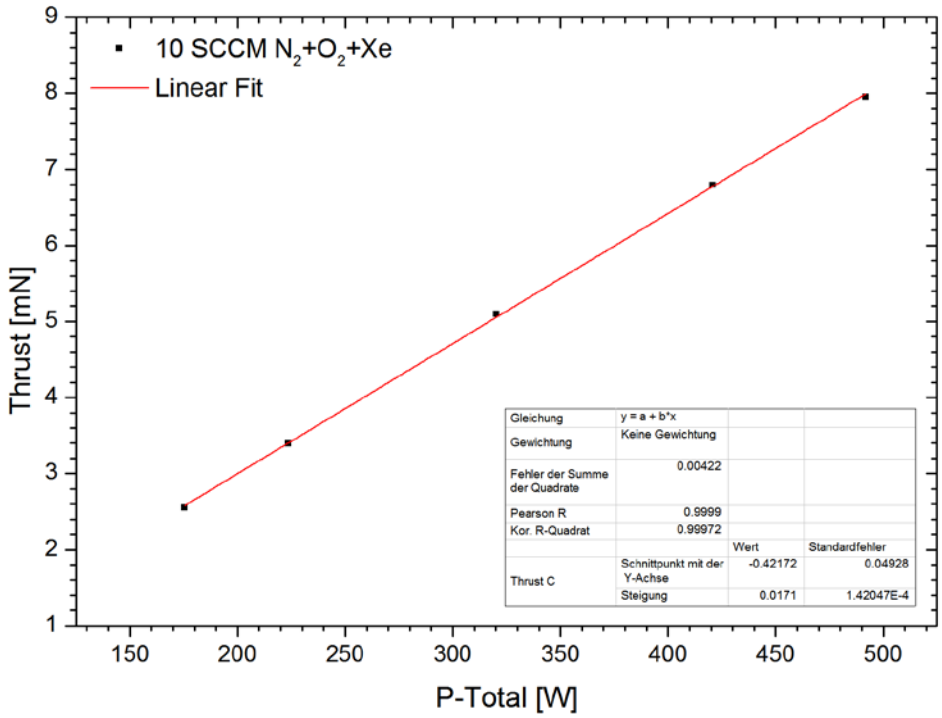

Figure 4-53: N_2+O_2+Xe power consumption interpolated for different thrusts at 10 SCCM gas flow

4.7.4. Continuous thruster operation with N_2 + O_2 (500 hours endurance test)

The thruster shall be operated with a beam level of 150mA for 500 hours continuously with the mixture (1.27 N_2 + O_2).

The used parameter setting for the 500 hours lifetime test are defined in Table 4-26.

I_{Beam} [mA]	mT set [SCCM]	U_{PHV} [V]	U_{NHV} [V]
150	6.5	1500	- 600

Table 4-26: Operational parameters for the endurance test

The Figure 4-54 shows the accumulated thrusting hours versus date.
The following Figure 4-55 gives an overview of the behavior of the thrust and the grid voltages during the 500 hour test. The vertical artifacts in the graph are caused by the ignition.

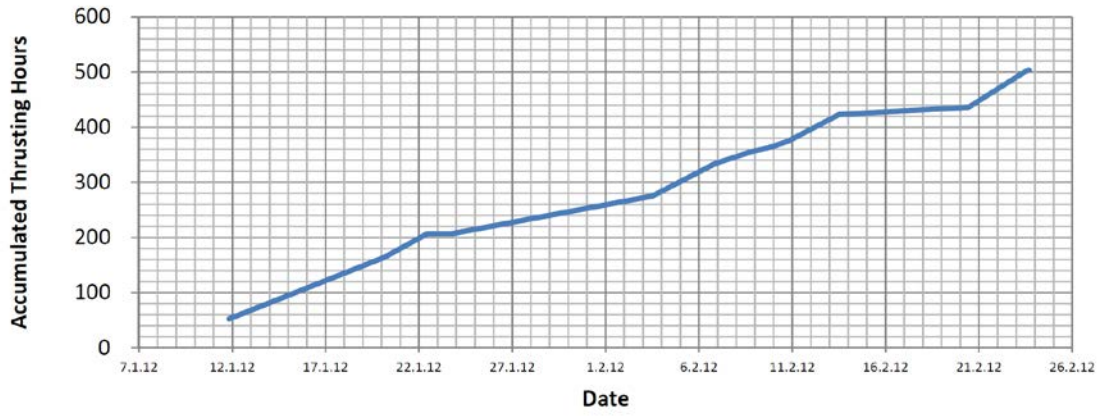

Figure 4-54: Accumulated thrusting hours versus date (no regeneration, off and standby periods are not counted)

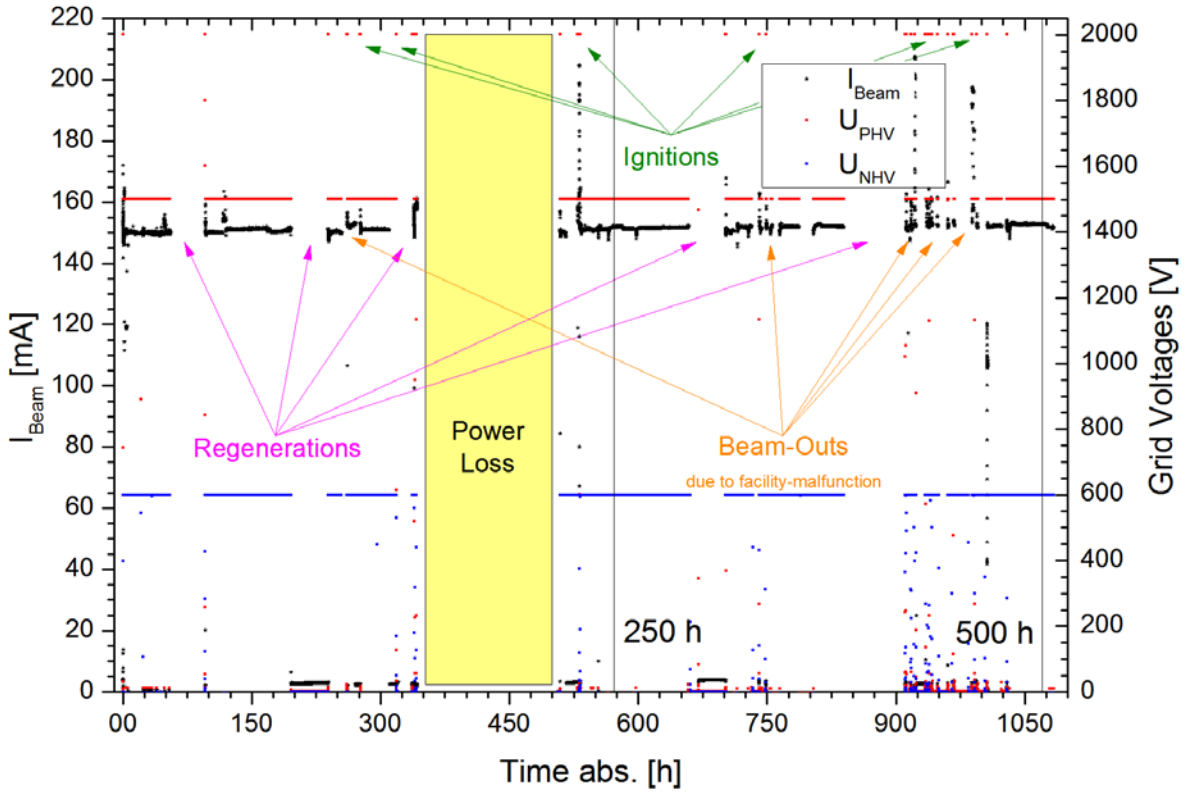

Figure 4-55: Overview of the 500 hours test

During this test, severe problems of the test facility for this test were observed. After around 160 hours, a part of the beam target was damaged, so that the target cryo panels were partially in the direct beam at the edge. “Droplets” were built up from the frozen propellant on the cryo panels. Dropping down of the cryo panels, they caused pressure increase in the chamber (see Figure 4-56). These pressure peaks resulted in the changes of the thruster parameters and partially in beam outs. As the real reason of this effect has not been clear before the end of the test and opening the chamber, the most appropriate way to avoid the problem was to regenerate the cryo system more frequently. Furthermore there was also an electricity power outage due to a failure/fire in the “Power Switching Network” of the University.

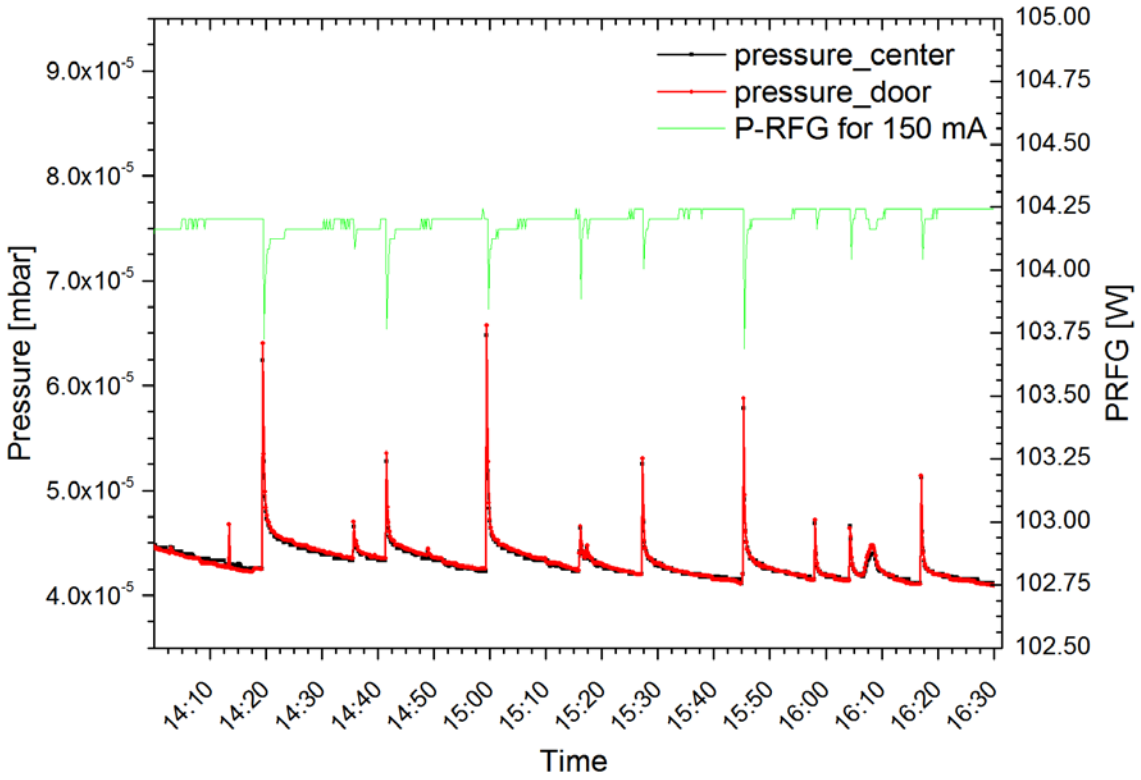

Figure 4-56: An example of the droplets problem during the lifetime test (22.02.2012)

4.7.5. Grid erosion measurement

As described in 3.2.5.2 the photos for the erosion measurement were taken with the described setup. The relevant holes were again marked with a paper mask shown in Figure 3-33. The post processing of the pictures was done with Photoshop 5 Extended. The needed calibration and correlation factor was computed from a series of slit pictures (Figure 3-26 to Figure 3-30). The inner diameters of the holes were compared. The first of the three grid measurements (M1) was performed at the beginning of the test campaign, the second measurements (M2) was done after the performance characterization part directly before the 500 h test and the last measurements (M3) after the lifetime test.

Table 4-27 and Table 4-28 show the results of the measurements on the accel grid for the three described measurements. Only the inner diameter was taken into account, edge erosion was also visible but not measureable. It is due to the non-optimized ion optic of the RAM-RIT-10 for atmospheric gases. The effect is however marginal and in this stage not visible on the thruster performance. It is not possible to give appropriate and somehow precise lifetime estimation after this test. For a reliable estimation a longer lifetime test (over 2000 hours) would be necessary. However, if the experiences with the lifetime test and lifetime model of the RIT-10 operated with Xenon is taken under account (26; 27), the lifetime should not be under 25000 hours.

Hole No.	Branch	Grid	Side	Initial [mm]	H-Ø M1 [mm]	V-Ø M1 [mm]	H- Ø M2 [mm]	V- Ø M2 [mm]	H- Ø M3 [mm]	V- Ø M3 [mm]
1	A	Accel	Top	2.00	2.00	2.00	2.02	2.01	1.98	2.01
2	A	Accel	Top	2.00	2.00	1.99	2.00	1.99	1.99	2.03
3	A	Accel	Top	2.00	1.98	1.98	2.00	1.99	2.03	2.03
4	A	Accel	Top	2.00	1.99	1.98	2.00	1.99	2.00	2.01
5	A	Accel	Top	2.00	2.00	2.01	2.01	2.01	2.02	2.02
6	A	Accel	Top	2.00	2.01	2.00	2.03	2.01	2.00	2.04
1	B	Accel	Top	2.00	2.01	2.00	2.02	2.02	1.99	2.01
2	B	Accel	Top	2.00	1.99	1.98	2.00	2.00	2.01	2.01
3	B	Accel	Top	2.00	1.99	1.99	2.01	2.00	2.00	2.01
4	B	Accel	Top	2.00	2.00	2.00	2.02	2.02	2.01	2.00
5	B	Accel	Top	2.00	2.00	2.00	2.02	2.02	2.00	2.00
6	B	Accel	Top	2.00	1.99	1.99	2.01	1.99	1.98	2.01
1	C	Accel	Top	2.00	2.02	2.01	2.03	2.03	2.03	2.00
2	C	Accel	Top	2.00	1.99	1.98	2.00	2.00	2.00	2.00
3	C	Accel	Top	2.00	1.99	1.98	2.00	2.00	2.02	2.00
4	C	Accel	Top	2.00	2.01	2.02	2.01	2.03	2.01	2.01
5	C	Accel	Top	2.00	2.02	2.02	2.02	2.02	2.01	2.01
6	C	Accel	Top	2.00	2.00	1.99	2.01	2.00	1.99	2.00

Table 4-27: The accel grid hole diameter (screen side) at the beginning of the test campaign (M1), before (M2) and after the 500 hours test (M3)

Hole No.	Branch	Grid	Side	Initial [mm]	H- Ø M1 [mm]	V- Ø M1 [mm]	H- Ø M2 [mm]	V- Ø M2 [mm]	H- Ø M3 [mm]	V- Ø M3 [mm]
1	A	Accel	Bottom	2.00	1.98	1.98	1.99	1.98	1.99	2.03
2	A	Accel	Bottom	2.00	1.98	1.98	1.98	1.99	2.02	2.01
3	A	Accel	Bottom	2.00	1.98	1.98	2.00	1.98	1.98	1.98
4	A	Accel	Bottom	2.00	1.98	1.98	2.00	1.98	1.98	1.98
5	A	Accel	Bottom	2.00	1.99	1.99	2.00	1.99	2.01	2.01
6	A	Accel	Bottom	2.00	1.99	1.99	2.00	1.99	2.00	2.00
1	B	Accel	Bottom	2.00	1.98	1.98	2.00	1.98	2.00	2.00
2	B	Accel	Bottom	2.00	1.98	1.98	1.99	1.98	1.98	1.98
3	B	Accel	Bottom	2.00	1.98	1.98	2.00	1.99	2.01	2.01
4	B	Accel	Bottom	2.00	1.98	1.99	2.01	2.00	2.02	2.02
5	B	Accel	Bottom	2.00	2.00	2.00	2.02	2.00	1.99	1.99
6	B	Accel	Bottom	2.00	1.98	1.98	2.00	1.97	1.99	1.98
1	C	Accel	Bottom	2.00	2.00	2.00	2.00	2.01	1.99	1.99
2	C	Accel	Bottom	2.00	1.98	1.97	1.98	1.99	1.99	1.99
3	C	Accel	Bottom	2.00	1.98	1.98	1.99	1.99	1.99	1.99
4	C	Accel	Bottom	2.00	2.00	1.99	2.01	2.00	2.00	2.00
5	C	Accel	Bottom	2.00	1.99	1.99	2.02	2.00	2.01	2.01
6	C	Accel	Bottom	2.00	1.98	1.99	2.00	2.01	1.98	2.01

Table 4-28: The accel grid hole diameter (decel side) at the beginning of the test campaign (M1), before (M2) and after the 500 hours test (M3)

4.7.6. Summary of the test campaign with gas mixtures

After changing the accel grid material from Graphite to Titanium and using an impedance transformation circuit at the input of the thruster coil to match the new thruster impedance to the old rf-generator, the performance characterization test and the preliminary lifetime test were successfully performed using the mixture of atmospheric propellants. The effect of using a small amount of Xe in the propellant mixture was also investigated successfully. The small increase of the thruster performance did not justify the need of Xenon for the thruster. The amount of Xenon can be reduced and eventually completely cut off, if the neutralizer would not need Xenon.

Performance values for the selected beam current levels i.e. thrust levels have been measured.

During the 500 hours of the long firing test the changes in the thruster performance have been observed, which was in the order of the measurement precision.

The behavior of the thruster performance is to a very large amount predictable. There were some minimal discrepancies at the lower gas flow and high RF-power regime. It is due to the dissociation processes and can only be understood by using the appropriate plasma/ion beam diagnostics systems specifically a plasma monitor.

The Titanium grid erosion is significantly lower than that of the Graphite grid, as its degradation rate under Oxygen environment is considerably lower than Graphite.

4.8. High performance test with $N_2 + O_2$

At the beginning of the high performance test the grid voltages have been investigated as described in the schedule, to test the behavior of the grid system apart from the predefined voltages. The thruster was operated with an ion beam current of 300 mA, while the negative high voltage applied to the accel grid was varied. Two flow rates had been used for this test (8 and 10 SCCM N_2+O_2). The positive high voltage was fixed at 2000 V. The NHV voltage was commanded from -650 V up to 0 V and the performance values were measured. While the NHV voltage is drawn against the rf-power and the total-power in Figure 4-57 and Figure 4-58, Figure 4-59 delivers the dependency of the drain current in respect to the NHV voltage. It can be seen that the drain current increases with higher voltages. Though, the negative accel grid voltage should not be selected too “low” to prevent electron back-streaming (especially when a NTR is used) and to improve beam forming and extraction. Therefore a NHV-voltage of -350 V was selected as a compromise.

After the grid voltages had been defined the main test was performed. The thruster was operated with N_2+O_2 at three different beam currents 300, 350 and 400 mA and with five different PHV voltages (applied to the screen) from 1500 V to 2400 V. The performance curves were measured and shown in Figure 4-60 to Figure 4-65. Even on this higher thrust levels, the engine performed very well without any problems. The maximum demonstrated

thrust is 15.46 mN with 400 mA beam current and $U_+ = 2400\ \mathrm{V}$. The given thrust is also calculated with the described equation 2-16 and dissociation is neglected. Based on the demonstrated mass efficiencies of up to 74 % (for 400 mA and 8 SCCM) the thruster has still some performance margins. The maximum theoretical extractable beam current is around 600 mA if nearly 100 % mass efficiency is assumed. But the thermal and rf-power limitations would probably prevent such optimal extraction currents, especially if the thruster should not be damaged. Figure 4-66 and Figure 4-67 demonstrate the correlation between the power to thrust ratio for different mass flows (with $U_+ = 2400\ \mathrm{V}$). It can be seen, that the ratios of the higher beam currents improve from higher flow rates compared to the low flow rate regime. All measured curves have a kind of crossing point at ~ 9.5 SCCM. At this point all three thrust levels have the same power to thrust ratio. The performance overview of the mass flow against P_{RFG} is shown in Figure 4-68 and for P_{Total} in Figure 4-69. These graphs are quite overloaded but summarizing the total results. To make a comparison easier, Figure 4-70 concentrates only on the 2400 V sequences. The increase in the total power consumption can clearly be seen. To generate 50 mA more thrust, this curve predicts an increase of ~200 W for the total power, at least in this thrust regime.

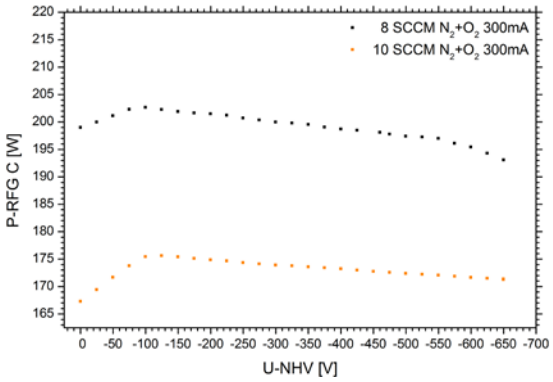

Figure 4-57: Voltage test for NHV with 2000 V PHV and 300 mA with N_2+O_2 (P-RFG)

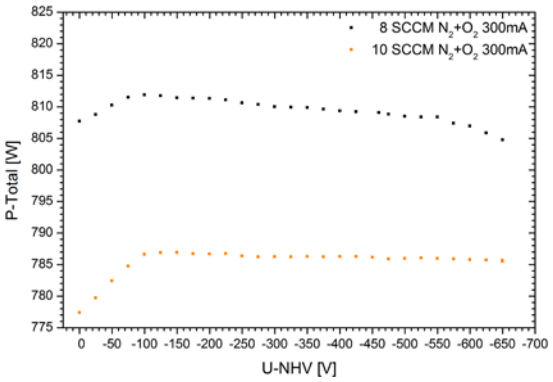

Figure 4-58: Voltage test for NHV with 2000 V PHV and 300 mA with N_2+O_2 (P-Total)

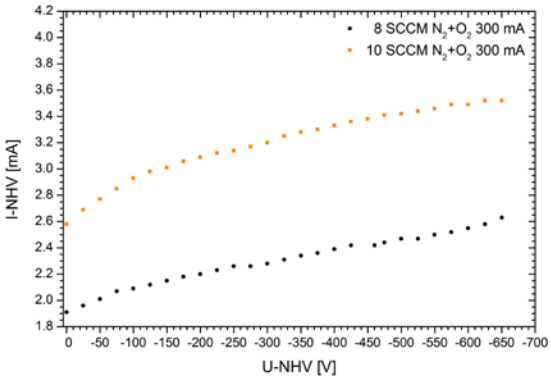

Figure 4-59: U_{NHV} to I_{NHV} at 300 mA with N_2+O_2

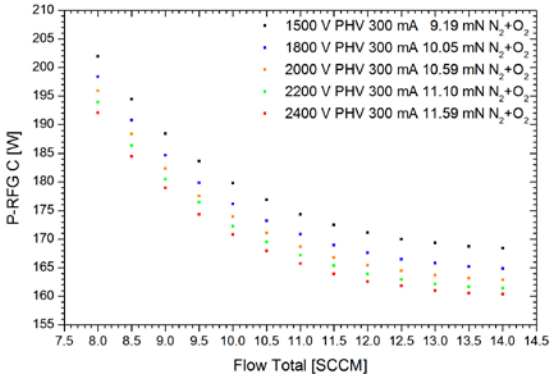

Figure 4-60: HPT with 300 mA N_2+O_2, NHV -350 V, P-RFG

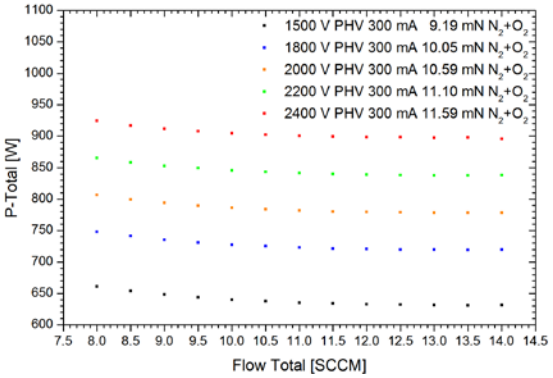

Figure 4-61: HPT with 300 mA N_2+O_2, NHV -350 V, P-Total

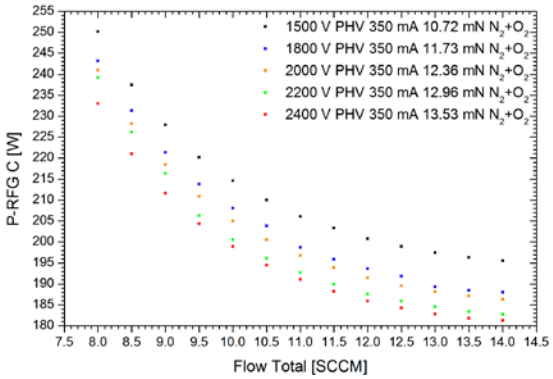

Figure 4-62: HPT with 350 mA N_2+O_2, NHV -350 V, P-RFG

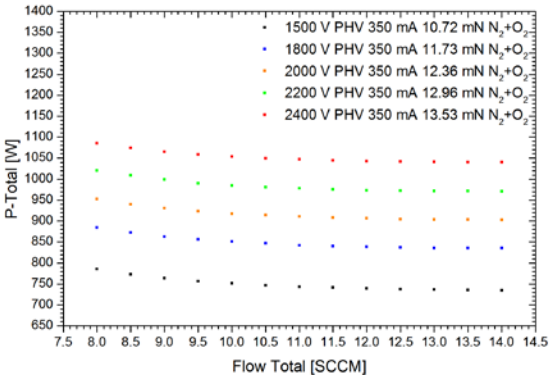

Figure 4-63: HPT with 350 mA N_2+O_2, NHV -350 V, P-Total

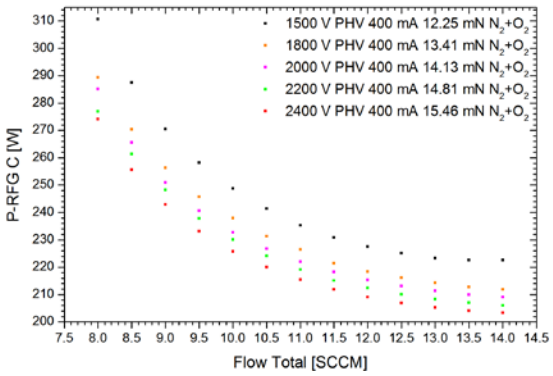

Figure 4-64: HPT with 400 mA N_2+O_2, NHV -350 V, P-RFG

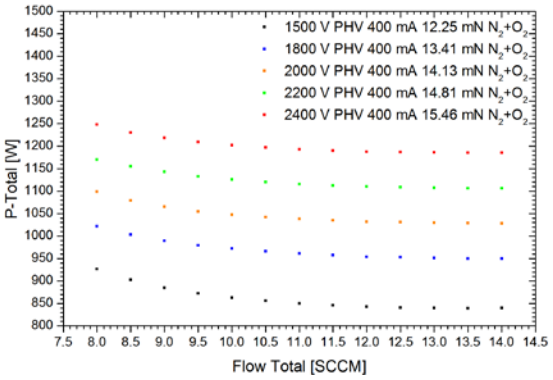

Figure 4-65: HPT with 400 mA N_2+O_2, NHV -350 V, P-Total

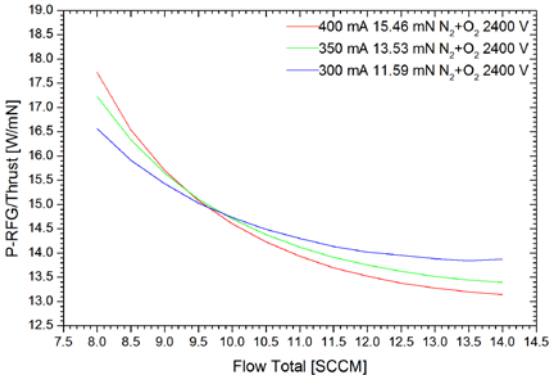

Figure 4-66: HPT P-RFG/Thrust to mass flow, N_2+O_2, 2400 V

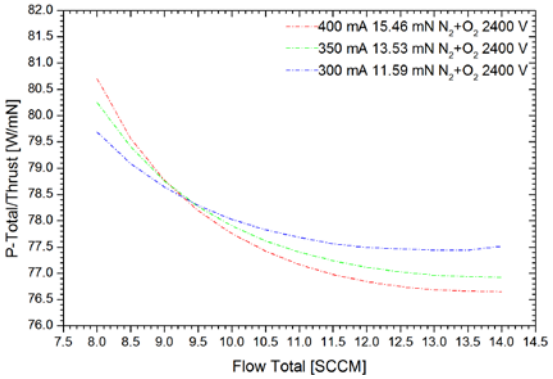

Figure 4-67: HPT P-Total/Thrust to mass flow, N_2+O_2, 2400 V

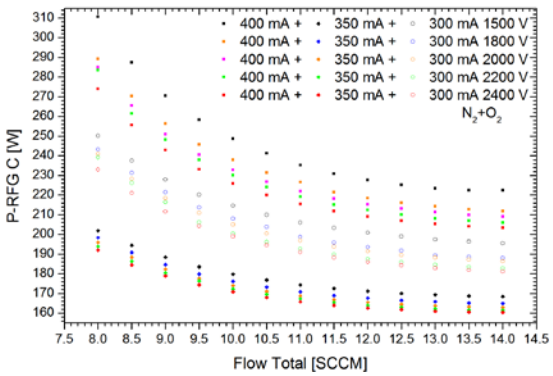

Figure 4-68: HPT P-RFG overview N_2+O_2

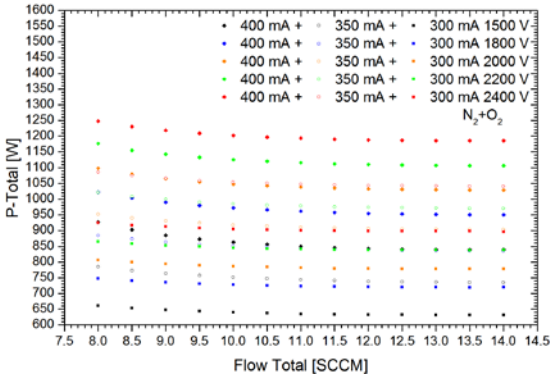

Figure 4-69: HPT P-Total overview N_2+O_2

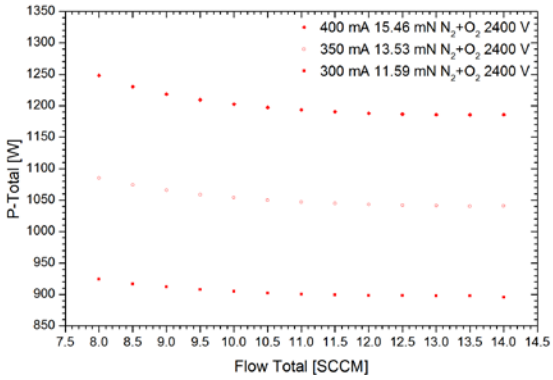

Figure 4-70: HPT P-Total overview for 2400 V PHV, N_2+O_2

5. Discussion

This chapter analyzes and describes the post-processing and the modeling results of the measured values and presents the thruster determined parameter ranges. The chapter is grouped into six sub-chapters. The first chapter describes the physical model, which is based on the measured results of this thesis. The second chapter discusses the problems and facts which have to be considered. The dissociation, probably observed during the Oxygen test campaign, is processed in the third chapter. The predicted dissociation and the computation of the corrected thrust are described in part four. The thruster operation range is discussed in chapter five and finally the modeling results are compared with the measured results in the last chapter.

5.1. Physical model based on the measured values

Based on the huge amount of data, acquired and measured during this thesis, a physical model to describe the thruster parameters was investigated. The results are presented in this chapter.

Figure 5-1 and Figure 5-2 show the measured performance curves of the RAM-RIT-10 operated with Nitrogen and Oxygen respectively. To describe these curves a theoretical calculation of the discharge was performed based on the theory described in chapter 2.

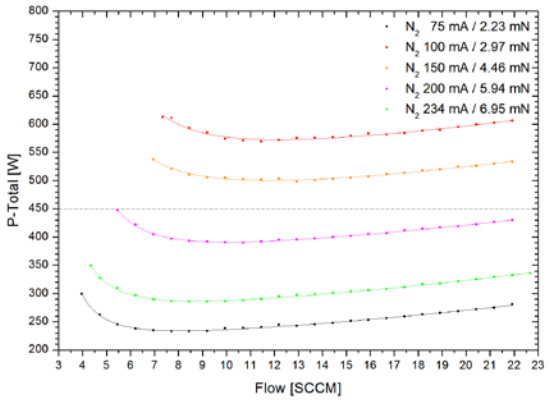

Figure 5-1: Performance overview N_2, P-Total

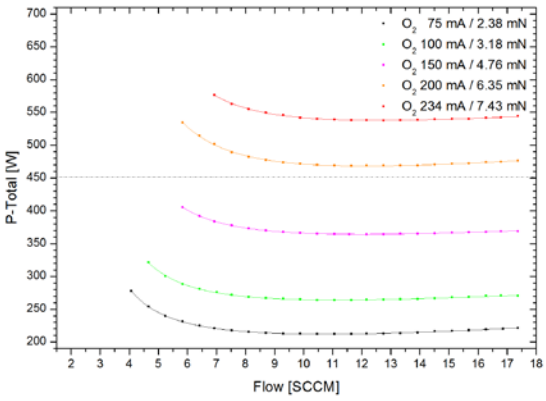

Figure 5-2: Performance overview O_2, P-Total

In these curves the total power consumption is given as a function of the mass flow for different thrust levels:

$$P, \dot{V}(F) \qquad 5\text{-}1$$

The total power is a summation of discharge rf power for ionization of the gas, the beam power and electric power due to the efficiency of the rf generator

$$P = I_i \cdot U_+ + I_{acc} \cdot U_- + P_{rf} + P_{Aux} \qquad 5\text{-}2$$

Model inputs:

$$U_- = 40\ \%\ U_+\ ,\ \beta = \frac{I_{acc}}{I_i} = 2\ \%,\ w_i = \frac{P_{rf}}{I_i} = 1.04\,\frac{W}{mA} = 1040V,\ \gamma = p_I/I_i$$

$$\dot{V} = \dot{V}_i + \dot{V}_0 = 13.935\frac{SCCM}{A} \cdot I_i + p_I \cdot L = I_i \cdot \left(13.935\frac{SCCM}{A} + \gamma L\right) \qquad 5\text{-}3$$

Model inputs (28): O_2: discharge pressure $p_I = 3.78 \cdot 10^{-4}\ Torr$,
grid gas conductivity $L = 1.179 \cdot 10^5\ cm^3/s$
N_2: discharge pressure $p_I = 4.11 \cdot 10^{-4}\ Torr$,
grid gas conductivity $L = 1.260 \cdot 10^5\ cm^3/s$

Grid data: hole diameters: $\emptyset_s = 3.2\ mm$, $\emptyset_a = 2.0\ mm$
grid thicknesses: $d_s = 0.5\ mm$, $d_a = 1.8\ mm$
interspace: $d_{sa} = 1.2\ mm$
number of holes: $N = 499$

Propellant efficiency: $\eta_m = \dot{V}_i/\dot{V}$

Model inputs (28): O_2: $\gamma = 1.512 \cdot 10^{-3}\ Torr/A$, $\eta_m = 49.76\ \%$
N_2: $\gamma = 1.644 \cdot 10^{-3}\ Torr/A$, $\eta_m = 46.01\ \%$

$$F = a \cdot I_i \cdot \sqrt{U_+ + V_P} \qquad 5\text{-}4$$

Model inputs: O_2: $a = 25.11\ mA/A \cdot kV^{1/2}$
N_2: $a = 23.49\ mA/A \cdot kV^{1/2}$
electron temperature $T_e = 10\ eV$, plasma potential $V_P = 45V$

$$I_{sp} = b \cdot \eta_m \cdot \sqrt{U_+ + V_P} \qquad 5\text{-}5$$

Model inputs: O_2: $b = 7798\ s/kV^{1/2}$
N_2: $b = 8335\ s/kV^{1/2}$

5.1.1. RAM-EP modeling using the experimental data

In the following, we will use the results of the test campaigns with N_2 and O_2 to model the used test engine running at +1.5 kV/-0.6 kV with 234 mA of beam current or with 450 W of power consumption, respectively. Figure 5-3 and Figure 5-4 show the measured mass efficiency of the investigated thruster. Further performance parameters like power consumption and gas flow are given in chapter 4.

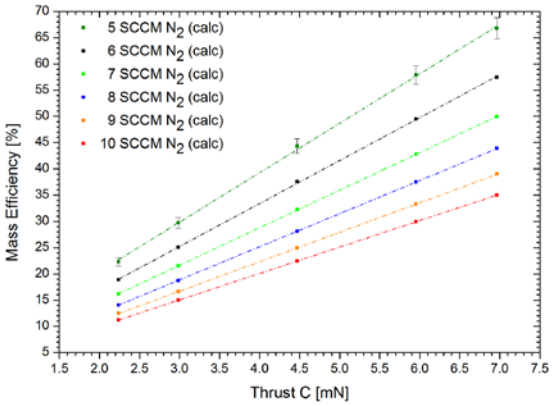

Figure 5-3: Mass efficiency of the RAM-RIT-10 running with N_2

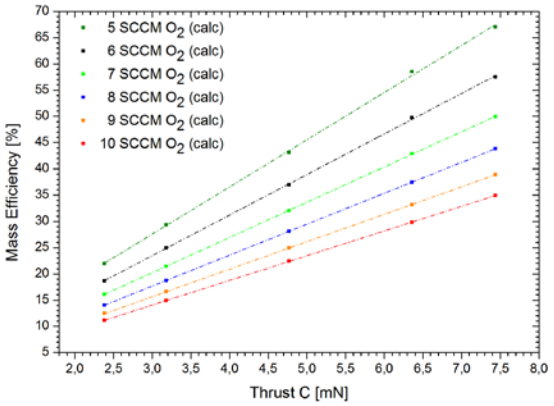

Figure 5-4: Mass efficiency of the RAM-RIT-10 running with O_2

Hereby, the theory explained in the preceding chapters (chapter 2), suggests that the used engine would not be able to yield optimum data for all three propellant species, Xe, N_2, and O_2. For the grid geometry, the Artemis design has been used (see Table 5-1). However, equation 2-12 suggests for Xe, O_2 and N_2 somewhat other data when comparing them with the actual RIT-engines. Here, we should take not only the ion mass into account, but also the extraction voltage U_{ex} and the ion current density j_i at the screen grid.

	RIT-22	**Artemis RIT-10 & test engine**	**Optimum grid data**		
	Xe, 175 mN	**Xe, 15 mN**	**Xe**	**N_2**	**O_2**
ion mass m_i [AMU]	131.3	131.3	131.1	28	32
current density j_i $[mA/cm^2]$	11.7	5.95	5.95	5.95	5.95
extraction voltage U_{ex} [kV]	2.315	1.95	2.10	2.10	2.10
scaling factor	1	-	1.301	1.915	1.851
number of apertures N	7148	499	853	409	433
open area ratio [%]	53.3	51.1	53.3	53.0	53.0
screen grid hole-diameter $\emptyset_s$ [mm]	1.9	3.2	2.5	3.6	3.5
accel grid hole-diameter $\emptyset_a$ [mm]	1.25	2.0	1.6	2.4	2.3
decel grid hole-diameter $\emptyset_d$ [mm]	open	~3.2	~2.5	~3.6	~3.5
screen grid thickness d_s [mm]	0.25	0.5	0.325	0.48	0.46
accel grid thickness d_a [mm]	1.2	1.8	1.55	2.3	2.2
decel grid thickness d_d [mm]	-	1.0	~1.0	~1.5	~1.4
screen/accel grid interspace d_{sa} [mm]	0.7	1.1	0.9	1.35	1.3
accel/decel grid interspace	-	0.7	~0.6	~0.85	~0.8

Table 5-1: Optimum grid geometry of a RAM-RIT-10 compared with that of a nominal-power RIT-22 (new standard Xe-geometry) and with the 10 cm Artemis-like test thruster

Looking at the Table 5-1, we see that the grid geometry of the Artemis-type test engine is more or less between the optimum design-data for an operation with Xenon and with atmospheric gases.

Concerning the rf-discharge, the actual measured performance data of N_2 and O_2 correspond completely with the theory (see above).

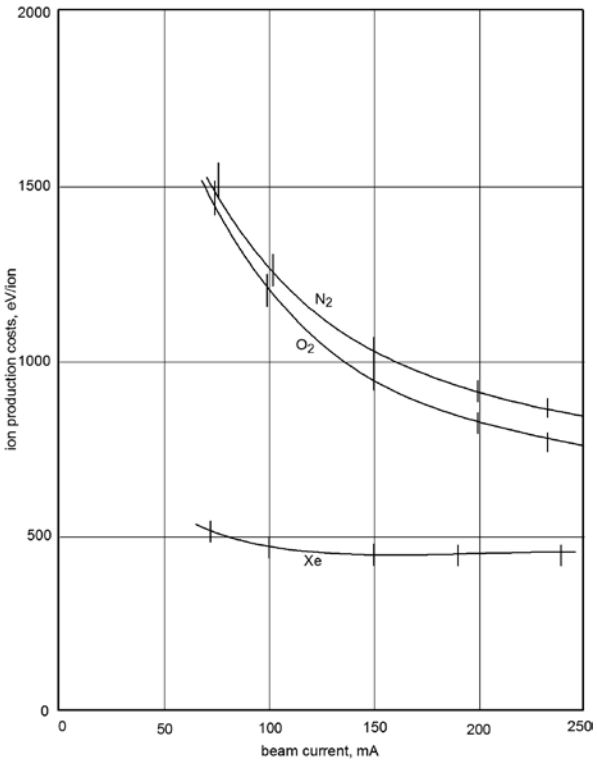

Figure 5-5: Ion production costs w_i of Xe, N_2 and O_2 as functions of I_{Beam} (11)

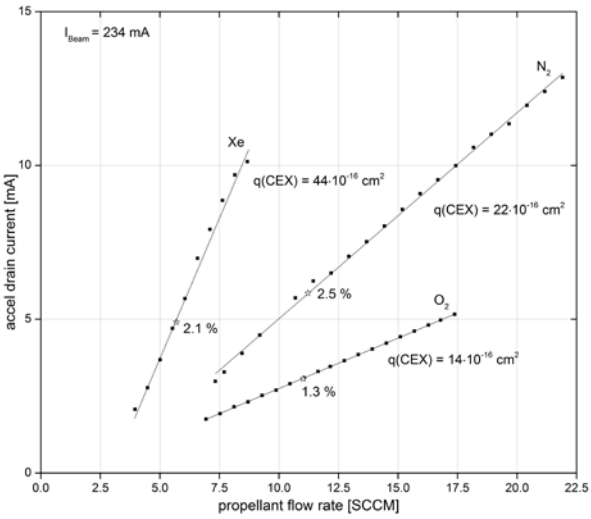

Figure 5-6: Accelerator drain current I_{acc} of Xe, N_2 and O_2 as a function of the propellant flow rate $\dot{V}$ (and thus of the rf-power, too); the CEX cross sections of the gases are given, too; the stars mark the operational $\dot{V}$- P_{rf} data. The beam current is kept constant ($I_{Beam} = 234\ mA$) (11)

Figure 5-5 shows that the ion production costs w_i (see equation 2-8) for N_2^+ and O_2^+ increased significantly when the engine had been throttled.

Figure 5-6 shows that the accel drain currents I_{acc} of all tested propellants increased linearly with the propellant flow-rate $\dot{V}$ (the extracted ion current I_i had been kept constant, and the rf-power P_{rf} had to be decreased for increasing gas flow rates following the discharge characteristics). As with increasing $\dot{V}$, also the gas pressure between the grids increases, the linearity proves that the drain current is originated by charge exchange collisions. The fact that the gradients depend on the charge exchange cross section q(CEX) (see Figure 5-6) corroborate the theory. The stars in the graphs mark the bending points of the discharge characteristic hyperbola, i.e. the working point of the engine. At this point the drain current ratios $\beta = \frac{I_{acc}}{I_i}$ amounted to 2.1 %, 2.5 %, and 1.3 % for Xe^+, N_2^+, and O_2^+, respectively.

At first sight, there has been observed a discrepancy between the measured thrust (by the thrust balance) and the calculated thrust (by equation 2-16) of the engine operated with Oxygen (see Figure 5-7): The measured thrust decreased at constant beam and voltage data at low propellant flow-rates, i.e. at increased rf-power. Obviously, this fact has been caused by an increasing portion of atomic Oxygen ions O^+. For all beam currents, the portion of O^+ at the bending point (see stars in Figure 5-7) is about 25 %. Due to its high dissociation energy, Nitrogen did not show this effect.

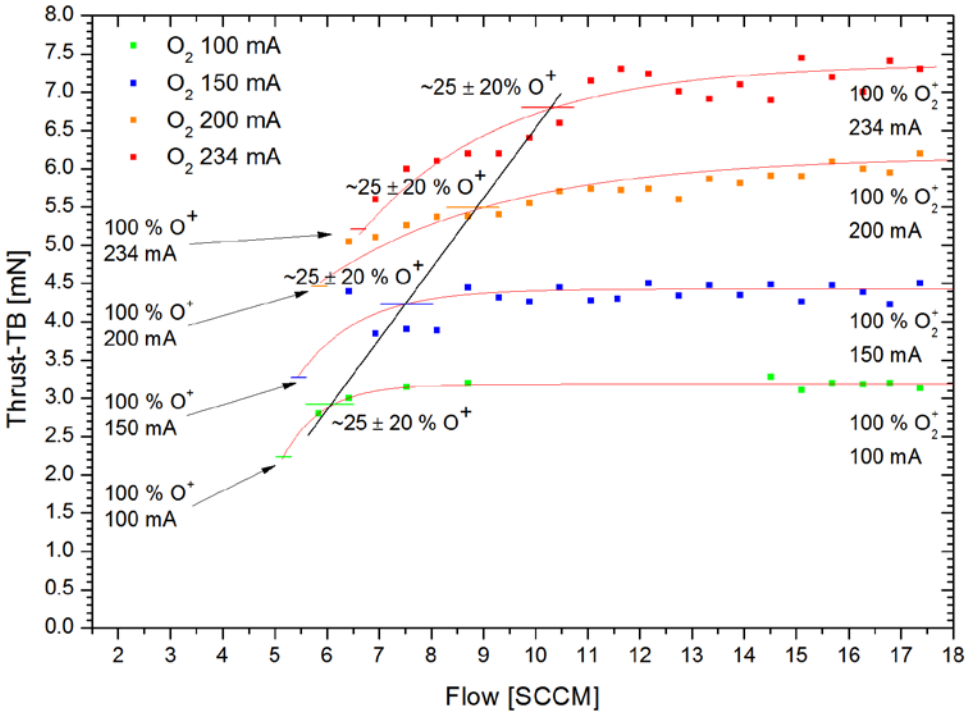

Figure 5-7: Measured thrust data F of Oxygen for 4 beam currents vs. the propellant flow rate $\dot{V}$; the crosspoints mark the optimum operation point of the engine, indicating a portion of about 25 % of atomic ions in the beam.

In general it can be said:

To generate the same beam current at the same high voltages, atmospheric gases require the double rf-power and the double gas flow rate than with Xenon, but their thrust is half of it due to their lower atomic masses.

5.1.2. RAM-EP performance with a mixture of Nitrogen and Oxygen

Following the standard atmospheric model (mentioned in chapter 2.4), the air composition in 200 km altitude and the mean solar activity delivers the following values:

O: $4.4 \cdot 10^{15}/m^3$
N_2: $3.0 \cdot 10^{15}/m^3$
O_2: $1.9 \cdot 10^{14}/m^3$

Other constitutes like He, Ar, H and N may be disregarded. The Figure 5-8 shows the optimal parameter regime of the thruster running with N_2+O_2. However, no dissociation processes were taken under account. The defined parameter field delivers the optimized dependency of the requested thrust and the correlated mass flow and rf-power pairs. This is again only valid if you assume that dissociation does not appear.

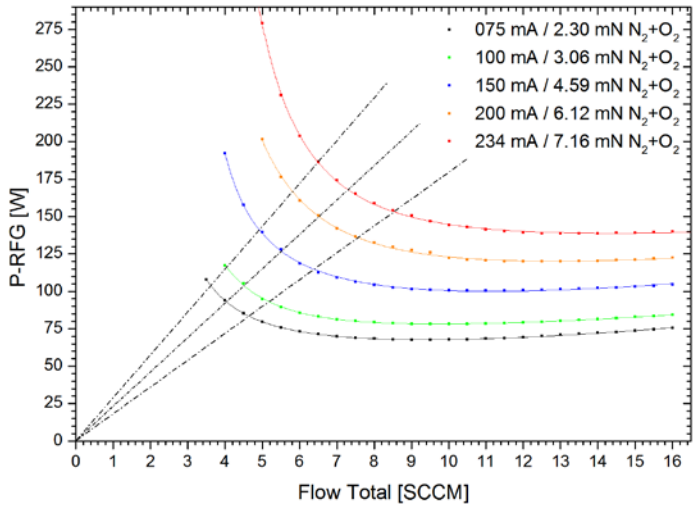

Figure 5-8: Defined optimal working regime of the RAM-RIT-10 for N_2+O_2 mixture, no respect to dissociation

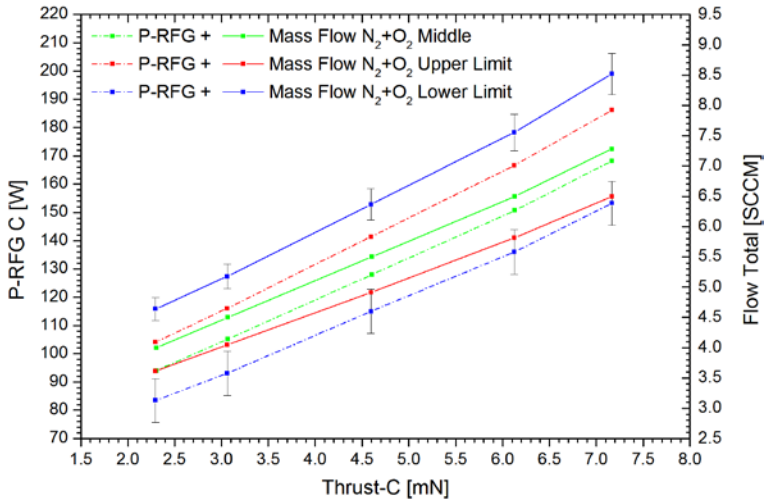

Figure 5-9: Optimal working regime of the RAM-RIT-10 thruster; P_{rf} and $\dot{V}$ against thrust for N_2+O_2

5.2. Gas mixtures

If gas mixtures are used to operate a thruster, different things have to be considered. This chapter will describe the two main points, which were important for this thesis: the changes in the thrust calculation and the ion optics.

5.2.1. Thrust calculations

The thrust calculation is performed by the use of equation 2-16, as described before. In this equation the ion-beam current, the positive high voltage and the plasma potential are the main input values. The divergence correction factor and the energy distribution can be neglected. As long as single masses are involved the thrust calculation is quite simple. But for gas mixtures and eventually partially dissociated propellants the equation becomes more complex. A superposition principle is used to calculate the individual thrust contingents for each particle type and summates them. The defined gas composition delivers the approximated particle ratios of the not dissociated propellant. In the case of dissociation,

the affected propellant component is spread up into a dissociated and not dissociated part. Each of these parts is also considered individually. The degree of dissociation has to be known or calculated before. Vice versa the degree of dissociation can be calculated by inverting the thrust formula and inserting the different masses. The precision of this method is around 20 %, but delivers a good first approximation of the degree of dissociation. It was used later in the post processing to evaluate a possible Oxygen dissociation.

5.2.2. Ion optic

The ion optic and beam extraction mentioned in 2.2.4 is sensitive on the ion masses being extracted and accelerated. As described, the focus-point of the electrical lens formed by the grid system should be in the plane of the accel grid to achieve the best results. All electrical charged particles were accelerated and attracted in the same way (as long as single charged state is supposed) but this is not valid for their impulse and the focus characteristics. The mixture of Nitrogen and Oxygen is somewhat a kind of exception; the two molecules have nearly the same mass and related ionization energies. The mis-focusing should be minimal for these mixtures. If a light weight or much heavier atom and or molecule is injected in addition, the beam divergence, the beam forming and the charge exchange will be affected. Whereas Xenon is a very good candidate for a single propellant mission and even reduces the power consumption and lower the plasma potential and electron energies of the discharge, it has a negative effect on the beam extraction and the grid lifetime. The grid system has to be optimized to a certain propellant mass to achieve the required lifetime of up to 70000 hours. Thus, Xenon should not be used in combination with Oxygen and Nitrogen due to the three times greater mass, if high mission lifetime is required.

5.3. Dissociation effects

Dissociation of gas molecules can have a great impact on a thruster, especially when theses gas molecules are used as a propellant. The main disadvantages of a dissociated propellant can be summarized easily. The dissociation process reduces the mass of the former molecule by dividing it into two or more atoms and or molecules (depends on the gas type). That means that the original impulse ($p = m \cdot v$) carried by the molecule is now less if the beam current is kept constant and single charged particles are expected. Also the required dissociation energy is then lost for the ionization processes, this results in additional higher power demand to maintain the plasma. And last but not least did the dissociated atoms and molecules disturb the extraction process and lead to a mis-focusing because of their differing masses. In general each molecule can be dissociated if the provided energy is high enough. In the case of the rf-plasma discharge the electron temperature T_e has to be high enough to enable these processes. The next chapters describe the dissociation observed during the test campaign and the resulting consequences.

5.3.1. Dissociation of O_2

During the test campaign with Oxygen a not insignificant deviation to the expected thrust was measured. Even the repetition of the measurement and re-commanding of different thruster parameters did not eliminate this discrepancy. The thrust deviation measured for 234 mA beam current operated with Oxygen is shown in Figure 5-10. The expected thrust levels were calculated prior to the test to have the ability to crosscheck the measurement. The red points represent the individual calculated thrust values for each 234 mA point. The black values were measured with the thrust balance. Apart from the measurement uncertainty of the thrust balance and the difficulties to stabilize the balance, these measured values were too far away to be only faulty value. The calculated thrust error ΔF is < 0.4 mN (equation 8-1) and also the systematic error of the measuring device is not big enough. The maximum deviation was around 1.8 mN and the drift is quite linear. As can be seen in Figure 5-10, the thruster performs in a normal way as long as higher mass flows are commanded. The fluctuations on the right side of the figure can be explained by the oscillations of the balance system. Also the beam divergence was not taken under account. Therefore the thrust should not be as high as the given reference values. Reducing the mass flow to values smaller than ~10 SCCM, lead to an increase of the thrust deviation. Assuming that the dissociation energy is quite low for Oxygen as described in chapter 2.1, already small changes in the discharge parameters can enable this process. It is predicted that this deviation is caused by dissociation.

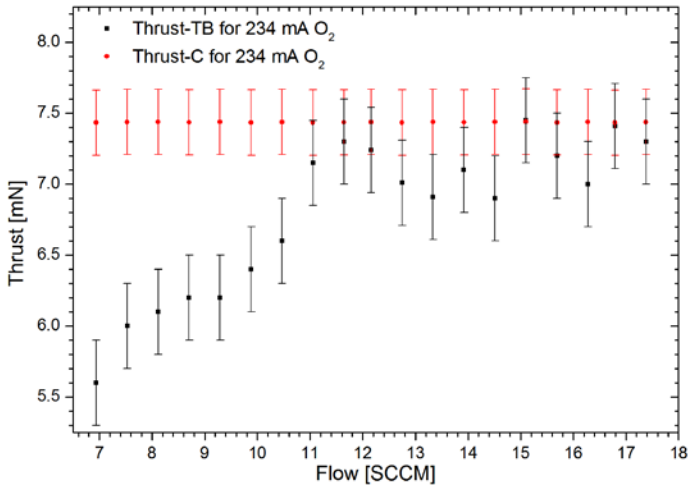

Figure 5-10: Thrust deviation for 234 mA running with O_2, the calculated and expected thrust is drawn in red and the measured thrust in black

The calculation method described in chapter 5.2.1 was used to approximate the degree of dissociation. The measured thrust was compared and calculated backwards by the use of the superposition principle to solve the particle ratios of the beam. The mentioned thrust deviation yields a degree of dissociation of up to 80 % $\pm$20 % for Oxygen (see Figure 5-11). It has to be mentioned that the divergence angle has a significant influence on these calculations, therefore it is recommended to measure the divergence angles for the different operational points of the thruster in addition to increase the precision of these calculations.

This was not part of this project and of the thesis. Ongoing tests already confirm partially the theory, that the electron temperature T_e is not dependent on the rf-power but on the discharge pressure p_I. The dissociation might be suppressed by increasing the mass flow to higher rates.

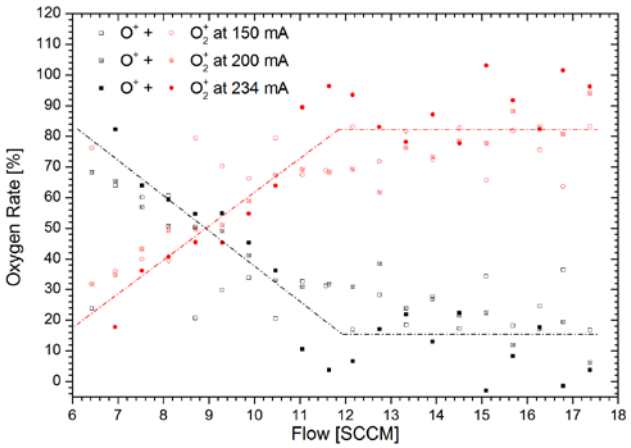

Figure 5-11: Calculated dissociation rate of Oxygen depending of mass flow

5.3.2. Dissociation of N_2

Apart from the observed dissociation artifacts during the Oxygen test campaign no dissociation effect could be observed or measured with Nitrogen in the operated limits. This corresponds in a good way with the discharge theory, because of the higher dissociation energies which would have been needed to dissociate Nitrogen too. The expected maximum electron temperature derived from the theory is around 10 eV, what is clearly under the dissociation energy. The dissociation process is expected to play only a minor role in the Nitrogen plasma discharge of an rf-thruster.

5.3.3. Dissociation of N_2 + O_2

The gas composition used for the gas mixture test campaign was defined to 1.27 N_2 +O_2 according to the atmospheric model. As already mentioned the Oxygen could be possibly dissociated, while Nitrogen did not show up this behavior. Under the adoption, which these two gases behave in the same way as a mixture than as in their single state, the expected dissociation for N_2+O_2 can be approximated. The gas distribution consists of 55.95 % Nitrogen and 44.05 % Oxygen. For this reason the impact of a possible dissociation of the Oxygen is expected to be comparably lower than before. The consequences for the resulting thrust should not exceed ~25 %, even if the complete amount of Oxygen would be dissociated. To prove this assumption, further investigations on the thrust, the beam constitution and the plasma discharge of an rf-thruster operated with atmospheric propellants have to be performed. This was not part of this thesis.

5.4. Predicted dissociation for N_2 + O_2 and the corrected thrust

Based on the described assumptions the anticipated dissociation for the gas mixture can be calculated and the generated thrust can be corrected. It has to be mentioned that a higher

propellant flow and therefore a higher discharge pressure p_I should minimize the diss. effect or even suppress it in total.

	Unit	Set 1	Set 2	Set 3	Set 4	Set 5
I_{Beam}	**[mA]**	234	234	234	234	234
U_{PHV}	**[V]**	1500	1500	1500	1500	1500
V_P	**[V]**	20	20	20	20	20
Div. angle θ	**[°]**	10	10	10	10	10
Rate of O^+	**[%]**	80	60	40	20	0
Rate of O_2^+	**[%]**	20	40	60	80	100
Thrust (Xe)	**[mN]**	14.94	14.94	14.94	14.94	14.94
Thrust ($Oxygen$)	**[mN]**	5.65	6.08	6.51	6.94	7.37
Thrust ($Nitrogen$)	**[mN]**	6.90	6.90	6.90	6.90	6.90
Thrust ($N_2 + O_2$)	**[mN]**	6.35	6.54	6.73	6.92	7.11
Thrust ($N_2 + O_2 + Xe$)	**[mN]**	7.21	7.38	7.55	7.72	7.89

Table 5-2: Thrust behavior of O_2 with variable dissociation rates

5.5. Operation range

During the complete test campaign a huge number of performance values have been measured and recorded. The gathered details of the thruster operation and the achieved performances allow extensive possibilities of data post processing and data analysis. The parameter ranges for the thruster, being operated with different propellants, have been approximated as shown in Figure 5-12 and Figure 5-13. The red line defines the upper power limit caused by the rf-power and also thruster temperature. The thruster should not be operated too long beyond this limit, even if it is possible. The black line defines the lower limit of the so called optimum range, the enclosed flow parameters can be considered as a good compromise between too much rf-power and too high flow rates, which would lead into low lifetime.

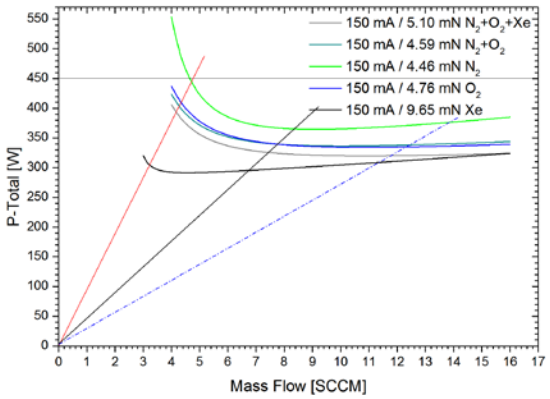

Figure 5-12: Thruster performance overview P-Total at 150 mA with indicated operation range

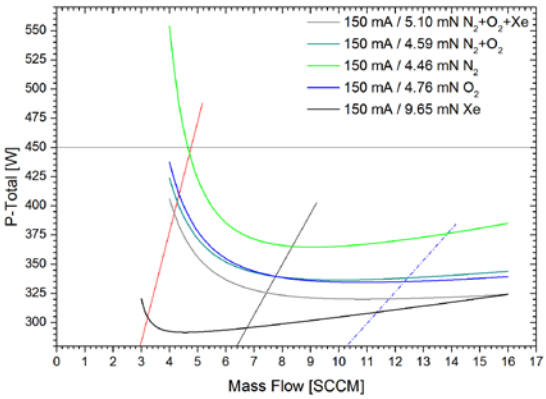

Figure 5-13: Thruster performance overview P-Total at 150 mA with indicated operation range, close-up

Beside this parameter field the range should be extended to the blue dashed line. Especially for dissociation susceptible propellant higher flow rates might be considered to reduce the dissociation. A thruster being operated in this regime would need lower power consumption, would have less heat dissipation and gas dissociation, but the mass efficiency and the I_{sp} would be lower than in the optimal point. The other main drawback of the high gas flow namely the higher I_{acc} and the lower lifetime of the thruster is still acceptable in this range. This has to be taken under account and a decision based on the defined mission parameters has to be made, which parameter regime has to be used.

However, the presented results may lead to operational points with low mass flow rates and therefore possible dissociation for Oxygen and the gas mixture. The calculated values of the table did not take care of the dissociation and the listed performance values like the thrust or mass efficiency might be lower than expected. To minimize or even avoid these effects, the mass flow rate should be > 10 SCCM for these propellants; this is according to the blue dashed regime. The thruster parameters at different ion currents are shown in Table 5-3. To have comparable values 10 SCCM was selected as mass flow.

		Xe		N_2		O_2		N_2+O_2	N_2+O_2+Xe
75 mA	**RF-Power P_{rf} $[W]$**	40.8		110.8		92.4		67.8	52.1
	Total-Power P_{Total} $[W]$	172.2		236.1		212.4		193.2	175.1
	Mass flow $\dot{V}$ $[SCCM]$	10.25		10		10		10	10
	Thrust F $[mN]$	4.83		2.24		2.38		2.30	2.55
	$ME\ \eta_m$ [%]	11.0		11.2		11.1		11.2	11.2
	Specific impulse I_{sp} $[s]$	534		1171		1092		1178	939
100 mA	**RF-Power P_{rf} $[W]$**	47.8		124.7		107.1		78.2	63.3
	Total-Power P_{Total} $[W]$	219.8		287.9		264.8		240.5	223.5
	Mass flow $\dot{V}$ $[SCCM]$	10		10		10		10	10
	Thrust F $[mN]$	6.44		2.98		3.18		3.07	3.41
	$ME\ \eta_m$ [%]	14.7		14.9		14.9		15.0	15
	Specific impulse I_{sp} $[s]$	712		1562		1455		1517	1254
150 mA	**RF-Power P_{rf} $[W]$**	63.9	55.9	152.1	120.0	132.4	99.2	100.9	85.5
	Total-Power P_{Total} $[W]$	317.2	305.8	391.1	365.8	366.1	334.8	336.9	320.2
	Mass flow $\dot{V}$ $[SCCM]$	10	10	10	10	10	10	10	10
	Thrust F $[mN]$	9.65	9.66	4.46	4.46	4.77	4.77	4.60	5.11
	$ME\ \eta_m$ [%]	22.2	22.3	22.4	22.5	22.4	22.5	22.5	22.4
	Specific impulse I_{sp} $[s]$	1073	1060	2339	2346	2188	2193	2277	1880
200 mA	**RF-Power P_{rf} $[W]$**	81.5		187.0		161.6		122.3	109.9
	Total-Power P_{Total} $[W]$	413.6		503.0		471.3		433.6	420.6
	Mass flow $\dot{V}$ $[SCCM]$	10		10		10		10	10
	Thrust F $[mN]$	12.89		5.95		6.35		6.13	6.81
	$ME\ \eta_m$ [%]	29.6		29.9		29.7		30.0	29.9
	Specific impulse I_{sp} $[s]$	1433		3122		2910		3033	2505
234 mA	**RF-Power P_{rf} $[W]$**	95.5		209.6		180.2		144.5	129.4
	Total-Power P_{Total} $[W]$	488.0		577.2		541.9		506.8	491.7
	Mass flow $\dot{V}$ $[SCCM]$	8.57		10		10		10	10
	Thrust F $[mN]$	15.06		6.96		7.43		7.17	7.96
	$ME\ \eta_m$ [%]	34.6		35.0		34.9		35.0	34.9
	Specific impulse I_{sp} $[s]$	1671		3656		3414		3546	2928

Table 5-3: Performance values for 10 SCCM and different beam currents

The red marked values were not measured at 10 SCCM but with only 9.20 SCCM. These values have been calculated for 10 SCCM. This was the highest operated mass flow because of the strongly increasing drain current I_{acc} for Xenon. To avoid damage to the grid system the performance mapping for 234 mA with Xe as propellant was ended with respect to the drain current. The here mentioned Xenon values for 10 SCCM do not represent the optimal working regime of the thruster, thus the losses on the accel grid were comparably high. This can be recognized by the high total-power, where the beam power, including the losses, is implied. Nevertheless they are given as a reference data set for comparison reasons. The 234 mA series has not been measured up to 10 SCCM, therefore the red marked values are extrapolated. The black values were also interpolated, because the original measured flow

rates were not exactly at the compared flow rate of 10 SCCM, but a little less or above. The green values have been measured after the RF-Impedance transformation. This transformation has a clearly positive impact on the discharge process. For Nitrogen and Oxygen for example the power consumption has decreased around 30 W. The following tables (Table 5-4 to Table 5-8) provide the calculated errors for the individual parameter sets of Xe, N_2, O_2, N_2+O_2 and N_2+O_2+Xe. They are calculated based on the given equations in appendix A.2. It is to mention, that the mass flow error is depending on the operation range. The uncertainty increases if the MFCs are operated near their lower limits.

Xe	75 mA	100 mA	150 mA	200 mA	234 mA
ΔP-RFG [W]	0.4	0.4	0.5	0.6	0.6
ΔP-Total [W]	2.3	2.6	3.2	3.8	4.2
ΔMass flow [%]	4 - 10	4 - 10	4 - 10	4 - 10	4 - 10
ΔThrust [mN]	0.2	0.2	0.3	0.4	0.5
ΔISP [s]	98	107	126	145	158
ΔME [%]	0.8	1.0	1.4	1.8	2.0
ΔThrust/P-RFG [mN/W]	1.0	0.7	0.4	0.3	0.3
ΔThrust/P-Total [mN/W]	4.7	3.4	2.2	1.6	1.4

Table 5-4: Calculated error values for Xe

N_2	75 mA	100 mA	150 mA	200 mA	234 mA
ΔP-RFG [W]	0.7	0.7	0.8	0.9	0.9
ΔP-Total [W]	2.5	2.8	3.4	4.0	4.4
ΔMass flow [%]	4 - 10	4 - 10	4 - 10	4 - 10	4 - 10
ΔThrust [mN]	0.1	0.1	0.2	0.2	0.2
ΔISP [s]	259	279	320	362	390
ΔME [%]	0.8	1.0	1.4	1.8	2.0
ΔThrust/P-RFG [mN/W]	7.4	4.6	2.5	1.7	1.4
ΔThrust/P-Total [mN/W]	16.7	11.5	7.0	5.1	4.2

Table 5-5: Calculated error values for N_2

O_2	75 mA	100 mA	150 mA	200 mA	234 mA
ΔP-RFG [W]	0.6	0.7	0.7	0.8	0.8
ΔP-Total [W]	2.4	2.7	3.3	3.9	4.3
ΔMass flow [%]	4 - 10	4 - 10	4 - 10	4 - 10	4 - 10
ΔThrust [mN]	0.1	0.1	0.2	0.2	0.2
ΔISP [s]	230	249	288	326	352
ΔME [%]	0.8	1.0	1.4	1.8	2.0
ΔThrust/P-RFG [mN/W]	5.3	3.5	1.9	1.3	1.1
ΔThrust/P-Total [mN/W]	13.2	9.3	5.8	4.2	3.5

Table 5-6: Calculated error values for O_2

N_2+O_2	75 mA	100 mA	150 mA	200 mA	234 mA
ΔP-RFG [W]	0.5	0.6	0.7	0.7	0.8
ΔP-Total [W]	2.4	2.7	3.2	3.8	4.2
ΔMass flow [%]	4 - 10	4 - 10	4 - 10	4 - 10	4 - 10
ΔThrust [mN]	0.1	0.1	0.2	0.2	0.2
ΔISP [s]	245	265	305	345	372
ΔME [%]	0.8	1.0	1.4	1.8	2.0
ΔThrust/P-RFG [mN/W]	4.3	2.8	1.6	1.1	1.0
ΔThrust/P-Total [mN/W]	13.0	9.2	5.8	4.2	3.6

Table 5-7: Calculated error values for N_2+O_2

N_2+O_2+Xe	75 mA	100 mA	150 mA	200 mA	234 mA
ΔP-RFG [W]	0.5	0.5	0.6	0.7	0.8
ΔP-Total [W]	2.3	2.6	3.2	3.8	4.2
ΔMass flow [%]	4 - 10	4 - 10	4 - 10	4 - 10	4 - 10
ΔThrust [mN]	0.1	0.1	0.2	0.2	0.3
ΔISP [s]	187	204	237	270	292
ΔME [%]	0.8	1.0	1.4	1.8	2.0
ΔThrust/P-RFG [mN/W]	2.8	1.9	1.2	0.8	0.7
ΔThrust/P-Total [mN/W]	9.9	7.1	4.6	3.4	2.9

Table 5-8: Calculated error values for N_2+O_2+Xe

5.6. Comparison between the predicted and measured performance values

By using the basic equations of chapter 2.3, the mathematical model yields the RAM-RIT-10 performance data with Xe, N_2, and O_2 while operating the engine with a beam current of 234 mA (Artemis-application; see Table 5-9).

$I_b = 234\ mA$	Xe	N_2	75 % O_2 + 25 % O
Rf-power P_{rf} $[W]$	102.5 (101.3)	208.5 (207.5)	177.2 (178.2)
Ion production costs w_i $[eV/ion]$	429.6	890	755
Gas flow rate $\dot{V}$ $[SCCM]$	5.0 (5.5)	9.3 (9.9)	8.2 (10.5)
Mass flow rate $\dot{m}$ $[mg/s]$	0.489	0.194	0.170
Discharge pressure p_I $[10^{-4}\ Torr]$	5.86	8.63	6.52
Drain current percentage β [%]	2.1	2.5	1.9
Accel grid drain current I_{acc} $[mA]$	4.9	5.9	4.4
Thrust F $[mN]$	14.71	6.83	6.79
Specific impulse I_{sp} $[s]$	3100	3636	4328
Thruster power input P_{Total} $[W]$	467	574	540
Propellant efficiency η_m [%]	65.2	35.1	39.1
Power efficiency η_e [%]	76.5	63.0	70.3

Table 5-9: RIT-10-EBB performance data of Xe, N_2 and O_2 for an ion current of I_i = 234 mA and voltages of U_+ = 1500 V and U_- = -600 V; ~25 % Oxygen will be dissociated

The comparison between the measured values (in red) and the theoretical values (in black) show a very good agreement for Xenon and Nitrogen, but for Oxygen a deviation in the gas

flow of around 20 % can be seen between the measured value and the predicted value. The reason can be identified in the approximation of the degree of the dissociation. A deviation of $\sim$20 % for the degree of dissociation would results in such a deviation between the calculated gas flow and the measured one (5.3.1).

Therefore it is strongly recommended that tests with gas mixtures should include also a mass spectrometer and a plasma monitor to take care about these facts and to gain further details on the extracted beam while operating the thruster with gas mixtures, especially with different gas types. N_2 and O_2 are quite comparable in this point, except the dissociation aspect.

Beside of the uncertainty in the degree of dissociation, there could be another source of failure due to the uncertainty in the calculation of the flow conductance for atomic Oxygen.

6. Conclusion

Based on the Artemis flight hardware, an elegant bread board model of a RIT-10 was constructed and some modifications have been performed to work with atmospheric gases of Oxygen and Nitrogen. These modifications were applied after the first tests with Oxygen and Nitrogen. At first the discharge was optimized by the adaptation of the thruster impedance to the rf-generator. The second modification was undertaken in the extraction system, to overcome the lifetime problem of the Graphite grid by using Oxygen due to the chemical degradation. This was done by replacing the Graphite grid by a Titanium version. After these modifications the thruster could be successfully operated with the defined gas mixtures required for an earth observation mission in 200 - 250 km orbit, utilizing RAM-EP technology. To characterize physically the thruster by using atmospheric gases as propellants, the discharge and extraction behavior of Nitrogen and Oxygen in the thruster was studied. Nitrogen and Oxygen perform quite similar concerning the power demand, what was already expected due to their comparable masses and ionization integrals. Only the dissociation aspect is different for these two gases. A discrepancy was observed between the directly measured thrust of the Oxygen propelled thruster and the calculated thrust, based on the measured beam current. This effect was more distinguished at lower gas flows, which led to higher electron temperatures inside the discharge plasma. This discrepancy is due to the lower dissociation energy of the Oxygen molecules. No discrepancy was observed for Nitrogen.

In combination these two gases worked very well with the RAM-RIT-10 thruster. Lower dissociation impact was also observed here.

The dissociation losses have not shown a negative influence on lifetime so far, but having only half the mass of the molecule should also affect the extraction process and the beam focusing. The biggest problem with the dissociation is the resulting thrust deviation, so higher rf-powers would have to be used to generate the desired thrust.

The effect of mixing the Nitrogen and Oxygen composition with a small amount of Xenon was also studied. The small performance improvement of the additional Xenon did not compensate the lifetime drawback due to the larger mass difference between Xenon and atmospheric gases.

The theoretical modeled performance values of the thruster could be validated and show a good agreement with the experimental data. The maximum thrust levels for the RAM-RIT-10 thruster, achievable with 450 W total-power, are summarized in the following table. The table shows the improvement of the thruster performance after the modifications. The orange marked values are based on the measured values before the modifications were implemented.

P_{Total} = 450 W	Xe Thrust [mN]	N_2 Thrust [mN]	O_2 Thrust [mN]	$N_2 + O_2$ Thrust [mN]	$N_2 + O_2 + Xe$ Thrust [mN]
8.5 SCCM	13.94	5.14	5.93	6.23	7.19
10 SCCM	14.21	5.23	6.03	6.33	7.28

Table 6-1: Achievable thrust levels for 450 watt p-total for different propellants

7. Outlook

The idea of using atmospheric gases as propellant for a propulsion system to compensate the atmospheric drag in lower earth orbits is very interesting for earth observation missions. However this idea should be developed toward a technology in two parallel sections:

1) The thruster should be further developed to optimize the power consumption and the gas flow for a specific thrust (depending on the orbit, sun activity and the satellite's geometry). The optimization of the size (diameter) of the thruster has been already started (see master thesis of Michael Becker (1)).Also the length of the thruster, the rf-coil and the frequency should be optimized. More investigations are needed on the ion optics, especially when the dissociation aspect is taken into account. In any case a complete diagnostics of the beam and the plasma are necessary. The beam diagnostics should cover the measurement of the beam divergence with the help of faraday arrays and the measurement of the ion energy distribution. Therefore a retarding potential analyzer should be used to get access to the electron energy distribution function in the discharge plasma. Also measurements with an energy selective mass spectrometer would be necessary to investigate the dissociation aspect in more detail. The measurement of the plasma parameters like electron energy and plasma density is required for the optimization of the ion optics and can be done using Langmuire probes or spectroscopic methods.

2) The gathering of the gas at the low earth orbit and the compression is another important part of this technology. The DSMC (Direct Simulation Monte Carlo) methods are necessary to optimize the pressure of the gathered gas for the function of a thruster. The experimental approach would be much more complicated and would require a source for atomic Oxygen and Nitrogen with velocities of up to 8000 m/s (1).

8. Reference list

1. **Becker, Michael.** *Simulation of Free Molecular and Transitional Flows for the Collector System of an Air-breathing Ion Thruster (Master Thesis).* 2013.

2. **Freisinger, J. et al.** *"Non-Propulsion Application of the RF-Ion Thruster for Material Processing with Reactive Gases".* Garmisch-Partenkirchen : IEPC-99-118, Oct. 1988.

3. **Walther, R., Schäfer, M. and Freisinger, J.** *"Plasma Diagnostics of the RF-Ion Thruster RIT-10".* 9th Electric Prop. Conf. Bethesda : AIAA 72-472, 1972.

4. **Löb, H. W.** *unpublished.*

5. **E. Brook, M.F.A. Harrison, and A.C.H. Smith, J. Phys.** *"Measurements of the electron impact ionisation cross sections of He, C, O and N atoms ".* s.l. : NIST.gov, 1978. B 11, 3115.

6. **Jackson, J. D.** *Klassische Elektrodynamik 4.Auflage.* s.l. : Walter de Gruyter, 2006. ISBN-13: 978-3-11-018970-4.

7. **Lorrain, P., Corson, D. R. and Lorrain, F.** *Elektromagnetische Felder und Wellen.* s.l. : Walter de Gruyter, 1995. ISBN: 3-11-012232-4.

8. **Peters, A.** *"Erzeugung negativer Wasserstoffionen in Hochfrequenz-Ionenquellen vom Typ RIG und PRIS" (diploma thesis).* Giessen : JLU Giessen, 1992.

9. **Löb, H. W. and Feili, D.** *"Development of RIT-Microthrusters".* 55th IAF-Congress, Vancouver : s.n., 2004. IAC-04S.4.04.

10. **Walther, R.** *"Diagnostik mit Doppelsonden an Hg-Proben" (diploma thesis).* Giessen : JLU Giessen, 1971.

11. **Löb, H. W. and Feili, D.** *unpublished.*

12. **Löb, H. W. et. al.** *"State-of-the-Art of the RIT-Ion Thrusters and their Spin-Offs".* 39th IAF-Congress, Bangalore : IAF-88-258, 1988.

13. **Velten, Hans-Werner.** "Komponenten-Optimierung der RIT10 Ionenquelle für dem Edelgasbetrieb zur Erweiterung der Leistungsgrenzen und zum Einsatz reaktiven Plasmen". Giessen : Justus-Liebig Universität Giessen, 1986.

14. **Hoffknecht, A.** *"Untersuchungen zur Erzeugung von negativen Wasserstoffionen mit einer PRIS-10 Quelle" (diploma thesis).* Giessen : JLU Giessen, 1996.

15. **Scholze, Frank, et al.** *"Ion Analytical Characterisation of the RIT 22 Ion Thruster".* Cincinnati, OH : 43rd AIAA/ASME/SAE/ASEE Joint Propulsion Conferenz and Exhibit, 2007. AIAA-2007-5216.

16. **Darwent, B. deW.** *Bond dissociation energies in simple molecules.* Washington DC : NIST/NSRDS, 1970. NSRDS-NBS 31.

17. **Löb, H. W.** *"RIT-Operation and Mission Potentialities".* 1992. RGC-EP 92-12.

18. **Goebel, D. M. and Katz, I.** *"Fundamentals of Electric Propulsion: Ion and Hall Thrusters (Jpl Space Science and Technology)".* s.l. : John Wiley & Sons; Auflage: 1. Auflage (25. November 2008), 2008. ISBN-13: 978-0470429273.

19. **Feili, D., Meyer, B. K. and Lotz, B.** *"Entwicklung, Optimierung und Charakterisierung".* s.l. : DLR, 2010. FKZ 50JR0541.

20. **Leiter, H. J., Löb, H. W. and Schartner, K. H.** *"The RIT15 Ion engines - A survey of the present state of radio frequency ion thruster technology and ist future potentiality" - Proceedings 3rd International Conference on Spacecraft Propulsion.* s.l. : Noordwijk : ESA Publ. Div. c/o ESTEC, 2000. ISBN: 92-9092-701-1 , ESA SP-465.

21. **Tartz, M., et al.** *"Study of extraction grid erosion in a long-time ion thruster operational test".* Toulouse : 28th Int. Electric Propulsion Conference, 2003. Paper IEPC-03-176.

22. **Löb, H. W., et al.** *"CONSEP II-Tandem Reference Mission".* s.l. : DLR-study 50 RS 0705, Nov. 2008.

23. **Wutz, M., et al.** *"Handbuch Vakuumtechnik - Theorie und Praxis" 7. Auflage.* s.l. : Friedr. Vieweg und Sohn, 2000. ISBN: 3-528-54884-3.

24. **Killinger, Rainer, et al.** *Electric Propulsion System For ARTEMIS;Rainer Killinger, Helmut Basner, Günther Kienlein, Johanes Müller;. DaimlerCrysler Aerospace AG, IEPC 99-054,.* IEPC 99-054 : DaimlerCrysler Aerospace AG, 1999.

25. **EADS Astrium GmbH.** Schematic drawings of the test power supply.

26. **Killinger, R., et al.** *"RITA Ion Propulsion for ARTEMIS Lifetime Test Results".* s.l. : AIAA 2000-3273.

27. **Tartz, M.; Hartmann, E.; Neumann, H.; Leibniz Institute of Surface Modification, Permoserstrasse 15, D-04318 Leipzig, Germany.** *"Validated simulation of the ion extraction grid lifetime".* s.l. : American Institute of Physics, 2008. DOI: 10.1063/1.2801376.

28. **Feili, Davar.** unpublished.

29. *Physical constants.* s.l. : www.NIST.gov.

30. **Lotz, B. and Feili, D.** *Preliminary characterization test campaign of electric propulsion technology with non conventional Propellants; TN-03; Test Report N2.* Giessen : ESA/ESTEC, 2010.

31. **Lotz, B. and Feili, D.** *Preliminary characterization test campaign of electric propulsion technology with non conventional propellants; Test Report for test campaign on RIT10EBBM TN-08; Test Report Gas Mixture.* Giessen : ESA/ESTEC, 29.05.2012.

32. **Lotz, B. and Feili, D.** *Preliminary characterization test campaign of electric propulsion technology with non conventional Propellants; TN-05; Test Report O2.* Giessen : ESA/ESTEC, 08.12.2010.

A.1 Physical constants

Constant	Description	Value
u	Atomic unit	$1.660538782 \cdot 10^{-27}\ [kg]$
m_{Xenon}	Mass of Xenon atom	$2.180171183 \cdot 10^{-25}\ [kg]$ / $131.293\ [u]$
m_{Oxygen}	Mass of Oxygen molecule O_2	$5.313391994 \cdot 10^{-26}\ [kg]$ / $32.9988\ [u]$
$m_{Nitrogen}$	Mass of Nitrogen molecule N_2	$4.651733711 \cdot 10^{-26}\ [kg]$ / $28.0134\ [u]$
m_e	Mass of electron	$9.10938291(40) \cdot 10^{-31}\ [kg]$
e	Electrical charge	$1.602176487 \cdot 10^{-19}\ [As]$
g	Earth gravity acceleration	$9.80665\ [m/s^2]$
k	Boltzmann constant	$1.3807 \cdot 10^{-23}\ [(VAs)\ /K]$

Table 8-1: Most important physical constants used in this thesis (29)

A.2 Error calculations

The here mentioned equations were used to calculate the error or uncertainty of the computed values. All known errors of the involved devices were considered or estimated if no real values were available. The equations are given in two notations. The first notation was used to calculate the relative error of the value of interest in percent. The other version allows the approximation of the absolute error in the particular unit.

Thrust calculation (F) :

$$\Delta Thrust = \sqrt{\frac{2\times m_{Ion}}{q_{Ion}}} \cdot \left(\frac{(1+\cos\theta)}{2} \cdot \sqrt{(U_{PHV}+V_P)} \cdot \Delta I_{Beam} + I_{Beam} \cdot \frac{\sin\theta}{2} \cdot \sqrt{(U_{PHV}+V_P)} \cdot \Delta\theta + I_{Beam} \cdot \frac{(1+\cos\theta)}{2} \cdot \frac{1}{2\cdot\sqrt{(U_{PHV}+V_P)}} \cdot (\Delta U_{PHV} + \Delta V_P) \right) \quad 8\text{-}1$$

$$\frac{\Delta Thrust}{Thrust} = \frac{\Delta I_{Beam}}{I_{Beam}} + \frac{\sin\theta}{1+\cos\theta} \cdot \Delta\theta + \frac{1}{U_{PHV}+V_P} \cdot (\Delta U_{PHV} + \Delta V_P) \quad 8\text{-}2$$

P_{RFG} and P_{Total} :

$$\Delta P_{RFG} = \Delta U_{RFG} \cdot I_{RFG} + U_{RFG} \cdot \Delta I_{RFG} \quad 8\text{-}3$$

$$\Delta P_{Total} = \Delta U_{RFG} \cdot I_{RFG} + U_{RFG} \cdot \Delta I_{RFG} + \Delta U_{RFG-Aux} \cdot I_{RFG-Aux} + U_{RFG-Aux} \cdot \Delta I_{RFG-Aux} + \Delta U_{PHV} \cdot I_{PHV} + U_{PHV} \cdot \Delta I_{PHV} + \Delta U_{NHV} \cdot I_{NHV} + U_{NHV} \cdot \Delta I_{NHV} \quad 8\text{-}4$$

Specific impuls (I_{sp}) :

$$\Delta I_{sp} = \frac{1}{(\dot{V}\cdot g)} \cdot \Delta Thrust + \frac{Thrust}{g\cdot\dot{V}^2} \cdot \Delta\dot{V} \quad 8\text{-}5$$

$$\frac{\Delta I_{sp}}{I_{sp}} = \frac{\Delta Thrust}{Thrust} + \frac{\Delta massflow}{massflow} \quad 8\text{-}6$$

Mass efficiency ($\eta_m = ME$) :

$$\Delta ME = \frac{\left(\frac{1\cdot mass}{1{,}602176487E{-}19\cdot 6{,}02214179E23}\right)}{\dot{V}} \cdot \Delta I_{Beam} + \frac{\left(\frac{I_{Beam}\cdot mass}{1{,}602176487E{-}19\cdot 6{,}02214179E23}\right)}{\dot{V}^2} \cdot \Delta\dot{V} \quad 8\text{-}7$$

$$\frac{\Delta ME}{ME} = \frac{\Delta I_{Beam}}{I_{Beam}} + \frac{\Delta \dot{V}}{\dot{V}}$$ *8-8*

RFG-Power per mN :

$$\Delta P_{RFG}/Thrust = \frac{\Delta P_{RFG}}{Thrust} + \frac{P_{RFG}}{Thrust^2} \cdot \Delta Thrust$$ *8-9*

$$\frac{\Delta(P_{RFG}/Thrust)}{(P_{RFG}/Thrust)} = \frac{\Delta P_{RFG}}{P_{RFG}} + \frac{\Delta Thrust}{Thrust}$$ *8-10*

Total-Power per mN :

$$\Delta P_{Total}/Thrust = \frac{\Delta P_{Total}}{Thrust} + \frac{P_{Total}}{Thrust^2} \cdot \Delta Thrust$$ *8-11*

$$\frac{\Delta(P_{Total}/Thrust)}{(P_{Total}/Thrust)} = \frac{\Delta P_{Total}}{P_{Total}} + \frac{\Delta Thrust}{Thrust}$$ *8-12*

c

Danksagung

Zu allererst möchte ich mich bei der Justus-Liebig-Universität, insbesondere bei meinem Doktorvater Prof Dr. B. K. Meyer und meinem Arbeitsgruppenleiter Dr. D. Feili bedanken, das meine Dissertation angenommen wurde und für die Unterstützung und Betreuung die ich während meiner Arbeit von ihnen erhalten habe.

Ich danke der Europäischen Weltraum Agentur (ESA), dem Haupt-Projektnehmer ALTA und Löwe Schwerpunkt RITSAT für die Finanzierung des Projektes " CHARACTERIZATION TEST CAMPAIGN OF ELECTRIC PROPULSION TECHNOLOGY WITH NON CONVENTIONAL PROPELLANTS".

Ich bedanke mich bei meinen Gutachtern, für die Annahme und zeitnahe Beurteilung meiner Dissertation.

Großer Dank gebührt auch Professor Dr. H.W. Löb für seine kompetente Beratung und Unterstützung. Obwohl er schon seit längerem im Ruhestand ist, wird er nicht müde mit Rat und Tat zu Seite zu stehen. Danke dafür.

Spezieller Dank gebührt der EADS-Astrium GmbH, insbesondere Dr.Hans Leiter und Ralf Kukies, für die freundliche Genehmigung, dass ich einen Großteil ihres Test –Equipments benutzen durfte und für ihre versierte Hilfestellung bei auftretenden Problemen.

Ich bedanke mich bei Johanes Müller für den hilfreichen Support, die zahlreichen Telefonate und Gespräche in denen er mir mit seiner großen Erfahrung oft Rat gegeben hat.

Ich bedanke mich bei der feinmechanischen Werkstatt, im speziellen bei Reiner Weis, Peter Schneider und Gerhard Boller für die Herstellung und Montage der verschiedenster Triebwerks- und Testaufbauteile. Ohne Ihre Unterstützung hätte ich die Arbeit in dieser Form nicht ohne weiteres abschließen können.

Für die tatkräftige Hilfe bei der Inbetriebnahme, den Umbaumaßnahmen, und eine umfassende technischen Betreuung bedanke ich mich bei meinem guten Kollegen Udo Bachmann. Insbesondere für die hervorragende Zusammenarbeit bei der Konzeptionierung und Umsetzung des neuen Flow-Boards.

Unserem Konstrukteur Thomas Wasem möchte ich mich ferner bedanken für die Hilfestellung bei der Konstruktion und dem Reverse-Engineering bezüglich der nötigen Teile. So manche Stunden haben wir vor dem Catia-Rechner verbracht um verschiedenste Unstimmigkeiten und Probleme zu lösen.

Der Elektronikwerkstatt im besonderen Thomas Nimmerfroh und Björn Bellof möchte ich für die Konfektionierung der Kabel und die messtechnische Unterstützung danken.

Ich danke meinen Kollegen Stephanie Bonnet, Maria Smirnova, Markus Piechotka, Jörn Mankiewicz, Alexander Börngen, Julian Kaupe, Benjamin Steinmüller, Michael Becker,

Waldemar Gärtner, Peter Köhler, Oliver Weller, Gregor Birmuske und allen die ich jetzt doch zu erwähnen vergessen habe, die mich bei dem Bau, Montage und Konstruktion, den gemachten Messungen und Simulationen sowie bei der Auswertung und Korrektur unterstützt haben.

Besonderen Dank gilt meinen Korrekturlesern Rudolf und Ilse Möse, meinem Schwager Philipp Nimtsch und meiner Schwester Christin Nimtsch, meiner Kollegin Stephanie Bonnet, meinem Chef und meiner Freundin, die mich maßgeblich bei der Fehlerfindung und der Fehlerbeseitigung unterstützt haben.

Mein ganz spezieller Dank gilt meinen Eltern und meiner Freundin Sandra Hennig, die mich im Verlauf meines Studiums und dieser Doktorarbeit stets unterstützt und diese mit großer Anteilnahme verfolgt haben.

Eidesstattliche Erklärung

„Ich habe die vorgelegte Dissertation selbständig und ohne unerlaubte fremde Hilfe und nur mit den Hilfen angefertigt, die ich in der Dissertation angegeben habe. Alle Textstellen, die wörtlich oder sinngemäß aus veröffentlichten Schriften entnommen sind, und alle Angaben, die auf mündlichen Auskünften beruhen, sind als solche kenntlich gemacht. Bei den von mir durchgeführten und in der Dissertation erwähnten Untersuchungen habe ich die Grundsätze guter wissenschaftlicher Praxis, wie sie in der „Satzung der Justus-Liebig-Universität Gießen zur Sicherung guter wissenschaftlicher Praxis“ niedergelegt sind, eingehalten.“

Gießen, den 17.05.2013